

IMPACT OF MECHANICAL STRESS ON ALGAN/GAN HEMT PERFORMANCE:
CHANNEL RESISTANCE AND GATE CURRENT

By

ANDREW DANIEL KOEHLER

A DISSERTATION PRESENTED TO THE GRADUATE SCHOOL
OF THE UNIVERSITY OF FLORIDA IN PARTIAL FULFILLMENT
OF THE REQUIREMENTS FOR THE DEGREE OF
DOCTOR OF PHILOSOPHY

UNIVERSITY OF FLORIDA

2011

© 2011 Andrew Daniel Koehler

To my family

ACKNOWLEDGMENTS

I would like to thank my advisor Dr. Scott E. Thompson. I have benefited from his advice and guidance during my studies. Also, I thank my co-chair Dr. Toshikazu Nishida for his encouragement and guidance. I would also like to thank Dr. Ant Ural and Dr. Brent Gila for their assistance and serving on my committee.

I also thank all of my current and past colleagues for their assistance and support: Amit, Eric, Guangyu, Hyunwoo, Jingjing, Ji-Song, Kehuey, Lu, Min, Nidhi, Onur, Sagar, Sri, Tony, Toshi, Ukjin, Uma, Xiaodong, Yongke, Younsung.

TABLE OF CONTENTS

	<u>page</u>
ACKNOWLEDGMENTS.....	4
LIST OF TABLES.....	7
LIST OF FIGURES.....	8
LIST OF ABBREVIATIONS.....	12
ABSTRACT.....	13
CHAPTER	
1 INTRODUCTION AND OVERVIEW	15
Overview of AlGaIn/GaN HEMTs	15
Stress in AlGaIn/GaN HEMTs	17
Stress in Semiconductor Technology	18
Motivation	19
Organization	21
2 ALGAN/GAN HEMT AND WAFER BENDING BACKGROUND	25
GaN Fundamentals.....	25
Spontaneous Polarization.....	25
Piezoelectric Polarization	26
Formation of 2DEG	28
Device Description.....	29
Mechanical Wafer Bending Experiment Setup.....	30
Four-Point Bending	31
Bending Measurements of Small Samples.....	31
Summary	33
3 EXTRACTION OF ALGAN/GAN HEMT GAUGE FACTOR IN THE PRESENCE OF TRAPS.....	42
Introduction	42
Effects of Trapped Charge.....	42
Experimental Setup	44
Elimination of Charge Trapping Effects	44
External Resistance Consideration	45
Results and Discussion.....	46
Gauge Factor Measurement.....	46
Resistance Change with Stress.....	47

	2DEG Change with Stress.....	47
	Electron Mobility Change with Stress	48
	Simulated Gauge Factor.....	49
	Summary	49
4	VERTICAL ELECTRIC FIELD IN THE ALGAN BARRIER.....	62
	Introduction	62
	Ideal 1D Calculation of E_{AlGaN}	63
	1D Experimentally Measured E_{AlGaN}	65
	2D Simulation of E_{AlGaN}	67
	Simulation Details.....	67
	Simulation Results.....	68
	Summary	69
5	FIELD DEPENDENT MECHANICAL STRESS SENSITIVITY OF ALGAN/GAN HEMT GATE LEAKAGE CURRENT.....	84
	Introduction	84
	Experiment.....	85
	Results and Discussion.....	86
	Wafer Bending Results.....	86
	Discussion	87
	Maximum compensation ($r = 1$)	90
	Reduced compensation ($1 < r < 2$).....	92
	Reduced compensation ($1 < r < 2$) with reverse current	94
	Summary	96
6	CONCLUSION.....	112
	Overall Summary	112
	Future Work	114
	LIST OF REFERENCES	116
	BIOGRAPHICAL SKETCH.....	126

LIST OF TABLES

<u>Table</u>		<u>page</u>
1-1	Key material parameters for high power high performance transistors.....	23
4-1	List of parameters used in 1D E_{AlGaN} calculation	71
5-1	Key parameters extracted to match experimental data	97

LIST OF FIGURES

<u>Figure</u>	<u>page</u>
1-1 Cross-section schematic of AlGa _x GaN/GaN HEMT on Si(111) substrate.	24
2-1 GaN-faced GaN crystal lattice, oriented along the <0001> direction.	34
2-2 Polarizations in strained Al _x Ga _{1-x} N (x = 0.26), relaxed GaN heterostructure. The strained AlGa _x N layer has larger spontaneous polarization than the GaN layer, as well as additional polarization from the piezoelectric effect.	35
2-3 Conduction band schematic diagram of an AlGa _x N/GaN HEMT showing charge balance.	36
2-4 Cross-section SEM of commercial devices characterized in this dissertation. Image from Nitronex [47].	37
2-5 Typical I_D - V_G curve of a depletion mode AlGa _x N/GaN HEMT measured at $V_{DS} = 0.1$ V.	38
2-6 Mechanical wafer bending setup: showing (a) a photograph of Si wafer under ~1 GPa of stress, and (b) a schematic of wafer under four-point bending.	39
2-7 GaN wafer sample attached to heat treated high carbon stainless steel inserted in a four-point bending setup.	40
2-8 Increasing and decreasing stress applied to a wafer mounted on a stainless steel strip. A strain gauge is used to determine the amount of applied stress. ...	41
3-1 Results of consecutive $V_{GS} = -2$ to 0 $V_{DS} = 0.1$ V measurement sweeps resulting in charge trapping and detrapping.	51
3-2 V_T measured in consecutive $I_D - V_G$ sweeps. In dark, $ V_T $ can increase (decrease) from detrapping (trapping) of electrons, depending the device initialization. Under unfiltered UV illumination, V_T does not fluctuate.	52
3-3 A decrease in channel resistance of 15% observed during 1200 seconds of measuring after turning on the incandescent microscope light.	53
3-4 Unfiltered UV measurement (a) I_D - V_G measurements in dark and under unfiltered UV light with a large increase in off-state current and a decrease in subthreshold slope. (b) The spectral output of the unfiltered UV light.	54
3-5 Filtered UV measurement (a) I_D - V_G measurements in dark and UV light filtered by a 380 nm bandpass filter. (b) The spectral output of UV light with 380 nm bandpass filter.	55

3-6	Experimental setup for photoionizing trapped charge to measure the gauge factor.	56
3-7	Illuminating the device under test with UV light stabilized R_{CH} to less than 0.02% variation for 1200 seconds of measurement.....	57
3-8	Normalized change in channel resistance with incrementally increasing and decreasing uniaxial stress.	58
3-9	R_{CH} measurements at each time interval stress was held constant. Error bars represent a three standard deviation confidence interval for the measurement.....	59
3-10	Schematic showing polarizations in AlGaIn/GaN HEMTs as fabricated (left), and 1 GPa mechanically applied stress (right) generating additional $P_{PE, mech}$ similar in magnitude for both AlGaIn and GaN layers.	60
3-11	Simulated change in n_s , μ_e and R_{CH} with uniaxial stress shown in bands of uncertainty. The bands signify variations in numerical results due to uncertainty in elastic and piezoelectric coefficients.	61
4-1	Energy band diagram schematic showing Ni/AlGaIn/GaN interface	72
4-2	Dependence of the 2DEG density (n_s) with gate bias for the 1D case, with no interface trapped charge. Threshold is defined when n_s is entirely depleted ($n_s = 0$).....	73
4-3	Idealistic 1D calculation of E_{AlGaIn} , assuming no interface trapped charge. E_{AlGaIn} increases linearly until the threshold voltage, then saturates.	74
4-4	Bar diagram of the AlGaIn/GaN interface charge for an ideal device with no trapped charge and an actual device. Trapped charge reduces the positive fixed sheet charge density at the AlGaIn/GaN interface.	75
4-5	Capacitance-Voltage measurement, which is integrated in order to determine $n_s(V)$	76
4-6	1D ideal (no interface trapped charge) calculation and the experimental result from experimental parameters obtained by adjusting σ_{int} and obtaining n_s from C-V	77
4-7	Optimized grid for Sentaurus simulation of the AlGaIn/GaN HEMT device.....	78
4-8	Experimental calculation of E_{AlGaIn} versus V_G compared to 2D simulation results.....	79
4-9	Vertical cross-section of electric field of the AlGaIn/GaN HEMT at the (a) center of the gate and (b) drain edge of the gate.....	80

4-10	Horizontal cross-section of E_{AlGaN} taken near the top surface of the AlGaN barrier 1 nm below the gate contact.	81
4-11	Horizontal cross-section of the electrostatic potential taken near the top surface of the GaN 0.5 nm below the AlGaN/GaN interface.....	82
4-12	Horizontal component of E_{AlGaN} at the (a) center and (b) edge of the gate.....	83
5-1	Electrical step stress measurement showing the breakdown of J_G at the critical voltage.....	98
5-2	Normalized change in J_G for incrementally increasing and decreasing uniaxial stress for (a) $V_G = -0.25$ V and (b) $V_G = -4$ V.	99
5-3	$\Delta J_G(\sigma)/J_G(0)$ averaged for all levels of compressive and tensile stress at $V_G = -0.25$ V and -4 V. Uncertainty comes from three standard deviation from the measurement of $\Delta J_G(\sigma)/J_G(0)$ over the duration stress was held constant.	100
5-4	Experimentally measured stress sensitivity of J_G per 100 MPa of stress, as a function of reverse gate bias.....	101
5-5	Measured gate leakage current density versus gate voltage from $T = 300$ K to 400 K for unstressed AlGaN/GaN HEMT.....	102
5-6	PF plot showing linear fit to the measured data for $T = 300$ K to 400 K.....	103
5-7	The slope of the PF plot (m) plotted versus $1/T$. The slope of this plot (m') is used to calculate ϵ_{AlGaN}	104
5-8	The y -intercept of the PF plot versus $1/T$. The slope of this plot (m'') is used to calculate the trap energy level.	105
5-9	Schematic of change in E_A with compressive and tensile stress. Compressive stress increases E_A , decreasing r , increasing compensation, and reducing PF emission. The opposite is true for tensile stress.....	106
5-10	Simulated stress sensitivity of J_G per 100 MPa of stress, including E_A and r changing with stress, as a function of reverse gate bias.	107
5-11	Schematic of J_G , J_{PF} , and J_R assuming J_R is a bulk-assisted mechanism driven by the PF emission current for $V_G = -2$ V and other parameters from Table 4-1.	108
5-12	Measured J_G , ideal J_{PF} obtained by linear extrapolation of the linear PF fit, and J_R calculated by the difference between J_{PF} and J_G	109

- 5-13 Simulated stress sensitivity of J_G at 100 MPa of stress, including J_R , as a function of reverse gate bias. J_R not changing with stress overestimates the stress sensitivity. However, $\Delta J_R(\sigma)/J_G(0) = 1.5\%$ matches experiment..... 110
- 5-14 Energy band diagrams showing the reduction in the AlGaN barrier thickness at the gate edges for V_G well below V_T 111

LIST OF ABBREVIATIONS

DC	Direct current
FN	Fowler-Nordheim
GF	Gauge factor
HEMT	High electron mobility transistor
MEMS	Microelectromechanical systems
MOCVD	Metal organic chemical vapor deposition
MOSFET	Metal oxide semiconductor field effect transistor
PF	Poole-Frenkel
SEM	Scanning electron microscope
UV	Ultraviolet

Abstract of Dissertation Presented to the Graduate School
of the University of Florida in Partial Fulfillment of the
Requirements for the Degree of Doctor of Philosophy

IMPACT OF MECHANICAL STRESS ON ALGAN/GAN HEMT PERFORMANCE:
CHANNEL RESISTANCE AND GATE CURRENT

By

Andrew Daniel Koehler

December 2011

Chair: Scott E. Thompson

Cochair: Toshikazu Nishida

Major: Electrical and Computer Engineering

AlGaIn/GaN high electron mobility transistors (HEMTs) stand out with superb advantages for high-power, high-temperature, high-frequency applications. Internal stress is inherent to state-of-the-art AlGaIn/GaN HEMTs and has the potential to impact performance and reliability. Strain is an integral part of modern semiconductor technology and has been used to extend scaling of Si for nearly a decade, and the performance and reliability implications are well understood. Understanding the impact of mechanical stress on AlGaIn/GaN HEMT channel resistance and gate current is crucial for continued improvements in device performance and reliability.

Repeatable gauge factors of an AlGaIn/GaN HEMT device were obtained after eliminating parasitic charge trapping effects. Over four orders of magnitude of variation in gauge factors are reported in literature. Charge traps are likely responsible for the huge discrepancy. By employing continuous sub-bandgap optical excitation, the effect of non-repeatable charge trapping transients was effectively minimized, allowing the gauge factor to be accurately measured. The measured gauge factor is compared to a

simulated gauge factor, calculated from stress-induced changes in the 2DEG sheet carrier density and mobility.

Stress-altered gate leakage currents in AlGaIn/GaN HEMTs are measured as a function of constant applied reverse gate bias. Increasing reverse gate bias decreases the stress sensitivity of the gate leakage current. Poole-Frenkel emission dominates the gate leakage current for gate biases above threshold. Stress changes Poole-Frenkel emission by altering the trap activation energy, which also changes the compensation parameter. Reverse tunneling current which balances the forward Poole-Frenkel current at equilibrium is modeled to explain the experimental results. Tensile (compressive) stress decreases (increases) the trap activation energy, increasing (decreasing) the gate leakage current. Although below threshold, the electric field in the AlGaIn barrier saturates in the middle of the gate, the electric field increases at the gate edges because of two-dimensional effects. For larger reverse gate bias much below threshold, the thickness of the AlGaIn tunneling barrier decreases which causes Fowler-Nordheim tunneling at the gate edges to dominate the current transport.

CHAPTER 1 INTRODUCTION AND OVERVIEW

Overview of AlGaN/GaN HEMTs

III-V semiconductor devices show promise over Si metal-oxide-semiconductor field-effect transistors (MOSFETs) for high speed circuits. The focus of early III-V semiconductor research was toward GaAs MOSFET technology, however poor quality native oxide and high surface state density prevented channel electron accumulation. In 1980, Takashi Mimura from Fujitsu Laboratories developed a depletion-mode high electron mobility transistor (HEMT) with selectively doped n-type AlGaAs barrier, eliminating issues associated with native oxides on GaAs [1][2]. Although $\text{Al}_x\text{Ga}_{1-x}\text{N}$ was historically used in optoelectronic devices because of its direct and tunable band gap, AlGaN/GaN HEMTs were developed in 1993 by M. Asif Khan of APA Optics for high temperature, high performance devices [3].

Unique advantages associated with GaN make AlGaN/GaN HEMTs desirable for high-speed, high-performance applications. Table 1-1 summarizes key material parameters for high power high performance devices, displaying benefits of GaN compared to other relevant semiconductors. Although the effective mass (m^*) of GaN is larger than GaAs and InP, resulting in lower bulk effective low-field electron mobility (μ_e), the high conduction band density of states (DOS) and large saturation velocity (v_{sat}) still permits large current densities. The low dielectric constant (ϵ) reduces capacitive loading and allows for large area devices, increasing RF current and power [4]. The large band gap (E_G) improves radiation resistance, results in high intrinsic temperature, and provides a very large breakdown field (E_{br}) necessary for handling high RF power.

Heat dissipation benefits from the high thermal conductivity (κ), allowing for more efficient dissipation of heat away from the device.

Mechanical strain resulting from lattice mismatch between the AlGa_N and GaN layers induces piezoelectric polarization. This polarization increases the two-dimensional electron gas (2DEG) sheet carrier density (n_s). Benefitting from mechanical strain, AlGa_N/GaN HEMTs are capable of achieving n_s greater than 10^{13} cm⁻², without intentional doping. This is significantly higher than other III-V systems due to strong piezoelectric polarization in the Wurtzite GaN and AlN. Biaxial tensile stress in the AlGa_N barrier results from the lattice mismatch between AlGa_N and GaN, increase polarization at the AlGa_N/GaN interface and induces the mobile 2DEG. A cross-section schematic of an AlGa_N/GaN HEMT is shown in Figure 1-1.

The combination of material and structural benefits allows AlGa_N/GaN HEMTs to be suitable for various high power, high performance circuits. AlGa_N/GaN HEMTs are attractive for expanding markets in communications, radar, sensors, and automotive for both military and commercial applications. Integration of GaN on Si(111) substrates improves device performance and reliability while reducing cost [5], making AlGa_N/GaN HEMT technology extremely attractive for commercial and military markets. Currently, several commercial vendors have AlGa_N/GaN HEMT devices available, such as Cree, Fujitsu, Nitronex, RFMD, Toshiba, and Triquint.

An example AlGa_N/GaN HEMT power transistors of current commercially available operate at 2.7 to 3.5 GHz range (S-band) ,outputting 240 W of power with a power-added efficiency (PAE) of 60% [6][7]. In academia, an example of the current devices under investigation include Al₂O₃ dielectric layers forming metal-oxide-

semiconductor HEMTs, providing transistors with a PAE of 73% at 4 GHz at a 45 V drain bias [8].

Stress in AlGaN/GaN HEMTs

Stress is an integral part of AlGaN/GaN HEMT devices. Large mechanical stress profiles are created during processing and are generated during operation. These stresses can impact device performance and reliability.

In order for AlGaN/GaN HEMTs to be commercially competitive with Si alternatives, low-cost, large-scale production must be achieved. Si(111) substrates offer advantages of low-cost, large size, and high quality over sapphire and SiC alternatives. However, large differences in lattice constants (~17%) and thermal expansion coefficients (TEC) (~56%) between GaN and the Si(111) produce large strains, resulting in the formation of crystallographic defects [5]. High quality GaN layers on Si, free of cracks and dislocations, have been fabricated through implementation of stress mitigation using transition layers [5]. It is hypothesized that the lattice mismatch stress is primarily absorbed by the Al/Si interface, while the (Al, Ga) N transition layer absorbs the TEC mismatch stress, which occurs during processing [5].

Another type of stress induced during processing is biaxial tensile stress in the AlGaN barrier layer. The AlGaN barrier is pseudomorphically grown on the relaxed GaN channel/buffer. Lattice mismatch between AlGaN and GaN induces a biaxial tensile stress in the AlGaN barrier. For an Al concentration of 26%, the AlGaN barrier has ~3 GPa of biaxial tensile stress induced. This stress is advantageous since Wurtzite GaN and AlN grown in the (0001) orientation are both strongly piezoelectric [9]. The piezoelectric effect results in a polarization fixed charge at the AlGaN/GaN interface, inducing a mobile sheet charge layer which is termed a two-dimensional

electron gas (2DEG). SiO_2 or Si_3N_4 passivation possess residual stress which also has been shown to induce stress, adding to the lattice mismatch stress and increasing the 2DEG [10].

During operation, the vertical electric field under the gate contact through the inverse piezoelectric effect induces additional stress in the AlGaN barrier. This vertical field is the largest at the gate edges, where significant amounts of stress (500 MPa) can be generated in the AlGaN barrier during normal operation ($V_{GS} = 30$ V). It has been proposed that stress generated from the inverse piezoelectric effect can initiate defect formation leading to irreversible degradation [11]. Stress is of particular importance to performance and reliability of AlGaN/GaN HEMTs and has been investigated extensively in Si MOSFET technology for improving performance.

Stress in Semiconductor Technology

Piezoresistance, or change in electrical resistance in the presence of external mechanical stress, was first discovered in copper wires by Lord Kelvin in 1856 and first utilized in strain gauges in the 1930s [12]. Twenty years later, theory was developed outlining the implications of stress on semiconductors based on energy shifts resulting from deformation of the crystal lattice by Bardeen and Shockley [13]. In 1954, the first piezoresistance measurements of n and p type conduction for both Si and Ge were published [14]. The piezoresistive property of Si gave potential for Si pressure, flow, force, and acceleration sensors, as well as reducing the channel resistance of Si MOSFETs. In semiconductors, strain alters crystal symmetry and then alters the energy band structure by shifting bands, lifting band degeneracies, and warping bands. As a result, strain alters the carrier's mobility through mass change and of scattering change.

Stress can be introduced in a semiconductor through lattice-mismatched film growth in epitaxial heterostructures, deposited thin films, and applied external stress [15]. In the early 1980s, successful in-process implementation of beneficial strained epitaxial Si layers on relaxed $\text{Si}_{1-x}\text{Ge}_x$ demonstrated potential advantages of strain in Si technology [16], [17]. In-plane biaxial stress induced in the MOSFET channel results from mismatch in lattice constants between Si and SiGe. However, process integration challenges and almost negligible pMOSFET performance gains at typical operating voltages limited the usefulness of this technology [18], [19]. Uniaxial stress reduces crystalline symmetry more than biaxial stress providing superior enhancement in carrier mobility. In Si MOSFETs, tensile stress is beneficial for nMOSFETs and compressive stress is beneficial for pMOSFETs. Developing a process to implement both stresses on a single wafer challenged the semiconductor industry, particularly since biaxial stress was traditionally applied to entire wafer by growing strained Si on relaxed SiGe. These issues were overcome when the successful implementation of uniaxial stress in the CMOS process flow was achieved in the early 2000s, extending Moore's Law beyond the 90 nm node [20-22]. Longitudinal tensile stress was generated by nitride capping films for nMOSFETs, and longitudinal compressive stress was created by SiGe source drain for pMOSFETs. Soon after, dual stress liners capable of applying both tensile and compressive stresses were developed to eliminate SiGe source/drain integration issues [23]. Similar process-induced strain techniques remain implemented in nearly all commercial Si CMOS technologies to date.

Motivation

Although excellent AlGaIn/GaN HEMT performance has been demonstrated, electrical stability and reliability issues of these devices remain obstacles to further

development. Trapping centers at the AlGa_N surface, AlGa_N/Ga_N interface, and/or Ga_N bulk are considered the main origin of Ga_N reliability issues. Degradation effects associated with traps are characterized by low frequency noise [24-26], transconductance frequency dispersion [24], [27], current collapse [28], [29], gate-lag and drain-lag transients [30-32], threshold voltage shift [33], increased gate current [34], and light sensitivity [28], [30], [33]. Charging and discharging of traps can limit device performance. Generation of new traps can permanently degrade the device, even to breakdown. Understanding the degradation mechanisms is necessary for improving the performance and reliability of AlGa_N/Ga_N HEMTs.

One of the most widely accepted theories explaining AlGa_N/Ga_N HEMT degradation is based on the inverse piezoelectric effect [11], [35]. During operation, the large vertical field under the gate creates strain in the AlGa_N barrier, adding to the existing strain from lattice mismatch. Once the strain surpasses the material's critical limit (at the critical voltage), relaxation will occur through crystallographic defect formation. These generated defects act as trapping centers for electrons, degrading performance and reliability.

Large amounts of mechanical strain can certainly cause cracks and defects to form, however even nondestructive amounts of strain also can impact performance and reliability of the device. Strain reduces crystal symmetry, reorienting the energy band structure resulting in lifting of band degeneracies, shifting band energies, warping bands [15], and even altering trap energy levels [36]. This can affect carrier mobility by changing conductivity effective mass, density of states, and scattering, as well as impacting reliability, by increasing gate current, and increasing hot-carrier effects [37].

Since stress is a major factor in the operation, performance, and reliability in AlGaIn/GaN HEMT devices, a thorough understanding of the impact of stress on performance and reliability can lead to improvements in device design. The effects of strain in Si MOSFETs are well understood and used to improve the devices. Mechanical wafer bending is a cost-effective method to study the effects of stress on semiconductor devices which has been extensively used to isolate and study the effect of stress in Si MOSFETs. A systematic study of the effects of externally applied mechanical stress on the AlGaIn/GaN HEMT channel resistance and gate current can provide insights into the physical mechanisms responsible for stress-related performance and reliability issues.

Organization

The focus of this dissertation is to provide an improved understanding of the impact of mechanical stress on AlGaIn/GaN HEMT channel resistance and gate current which are key parameters for studying performance and reliability. Previous studies have suggested that catastrophic failure can be related to stress [11], [35]. Combining systematic mechanical wafer bending experiments and theory, physical models are presented to explain the incremental effect of stress on channel resistance and gate leakage current.

Background information will be provided in Chapter 2, beginning with fundamentals of AlGaIn/GaN HEMT operation. Then, a brief description of the characterization method is provided, followed by details on mechanical wafer bending. Chapter 3 presents experimental and theoretical details on the extraction of the AlGaIn/GaN HEMT gauge factor in the presence of traps. A comprehensive investigation of the vertical electric field in the AlGaIn barrier is given in Chapter 4. The

electric field model and simulation results assist in the analysis of the effect of stress on the gate leakage current presented in Chapter 5. Chapter 6 concludes the study with an overall summary and suggestions for future work.

Table 1-1. Key material parameters for high power high performance transistors

Parameter	Units	GaN	Si	GaAs	InP	4H-SiC
m^*	$m_0 \cdot \text{kg}$	0.22 [38]	1.56 [38]	0.06 [38]	0.07 [38]	0.58 [38]
μ_e	$\text{cm}^2/\text{V} \cdot \text{s}$	1245 [38]	1750 [38]	9340 [38]	6460 [38]	1000 [38]
DOS	10^{18} cm^{-3}	2.3 [39]	32 [39]	0.47 [39]	0.57 [39]	24.9 [39]
v_{sat}	10^7 cm/s	1.4 [40]	1 [41]	0.72 [41]	0.67 [41]	0.33 [39]
ϵ_r		9.4 [4]	11.9 [4]	12.5 [4]	12.9 [4]	10.0 [4]
E_G	eV	3.4 [4]	1.12 [38]	1.43 [38]	1.35 [38]	5.4 [38]
E_{br}	10^5 V/cm	20 [4]	3 [4]	4 [4]	4.5 [4]	35 [4]
κ	$\text{W}/^\circ\text{K} \cdot \text{cm}$	1.12 [38]	1.56 [38]	0.45 [38]	0.68 [38]	3.7 [38]

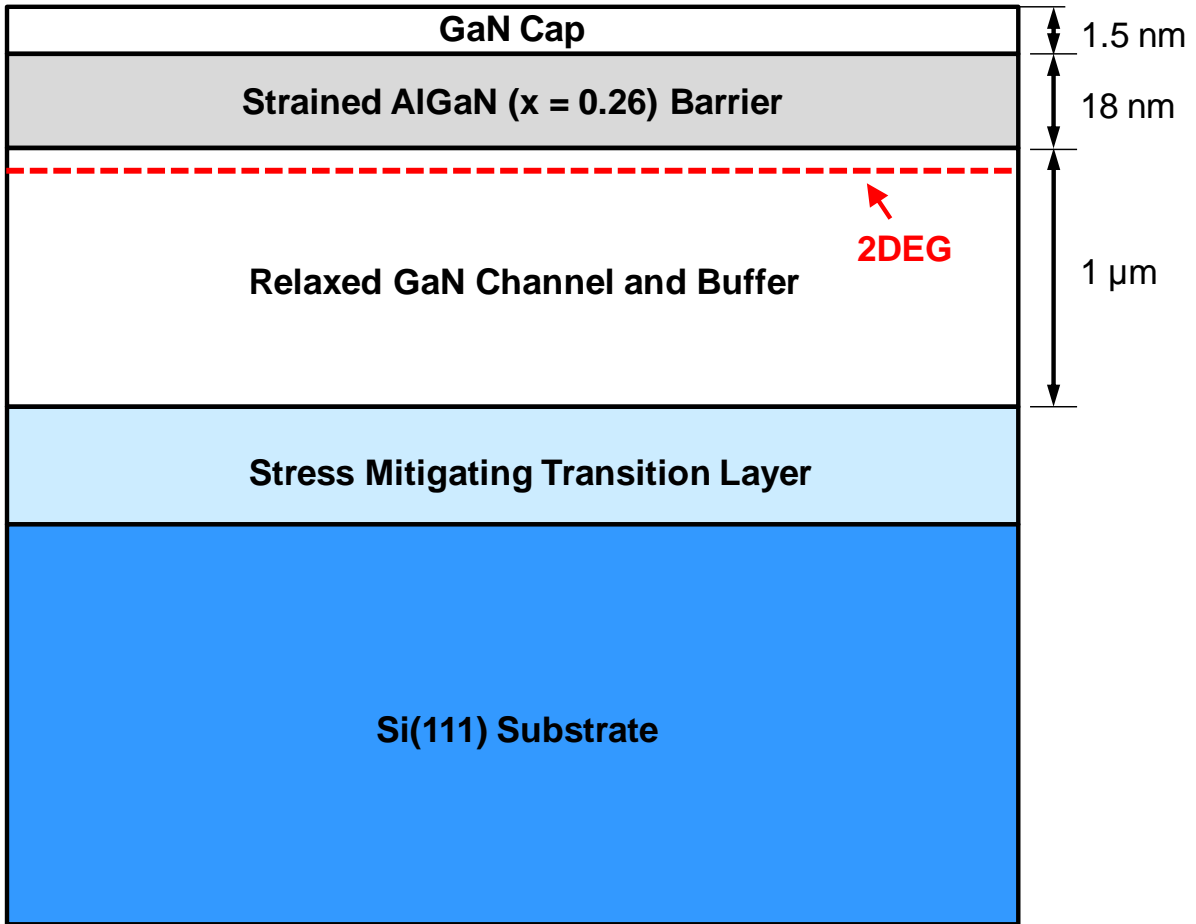


Figure 1-1. Cross-section schematic of AlGaN/GaN HEMT on Si(111) substrate.

CHAPTER 2 ALGAN/GAN HEMT AND WAFER BENDING BACKGROUND

GaN Fundamentals

AlGaIn/GaN HEMTs are depletion mode field effect transistors, benefiting from large 2DEG sheet carrier density, obtained without intentional doping or applied gate bias. The combination of spontaneous polarization (P_{SP}) and piezoelectric polarization (P_{PE}) in the AlGaIn and GaN layers create a macroscopic polarization which induces a 2DEG in the absence of electric field and intentional doping.

Spontaneous Polarization

There are two requirements for spontaneous polarization: lacking inversion symmetry and a bond between atoms that is not purely covalent. This results in a built-in dipole. In wurtzite semiconductors such as GaN, spontaneous polarization exists when the ratio c/a differs from the ideal value of $\sqrt{8/3}$, where c is the height and a is the spacing as shown in Figure 2-1. In order to induce a 2DEG of electrons desirable for AlGaIn/GaN HEMT performance, polarization must result in a net positive fixed charge at the AlGaIn/GaN interface. To achieve this, GaN is epitaxially grown in the direction normal to the (0001) basal plane, which lacks inversion symmetry. The top atomic layer is intentionally fabricated to be GaN, or GaN-faced. The \hat{z} direction or $\langle 0001 \rangle$ direction is defined as a vector originating from a Ga atom pointing to the nearest N atom as shown in Figure 2-1. In this orientation, spontaneous polarization exists only in the \hat{z} direction, therefore $P_{SP} = P_{SP} \hat{z}$. In AlGaIn, spontaneous polarization can be expressed in terms of AlN and GaN spontaneous polarization constants and the mole fraction x .

© [2010] IEEE. Reprinted with permission from [A.D. Koehler, A. Gupta, M. Chu, S. Parthasarathy, K.J. Linthicum, J.W. Johnson, T. Nishida, S.E. Thompson, Extraction of AlGaIn/GaN HEMT Gauge Factor in the Presence of Traps, IEEE Elec. Dev. Lett., vol. 31, pp 665-667, May 2010]

$$P_{SP}^{Al_xGa_{1-x}N}(x) = xP_{SP}^{AlN} + (1-x)P_{SP}^{GaN} \quad (2-1)$$

It is important to note that spontaneous polarization in AlN ($P_{SP}^{AlN} = -0.081 \text{ C/m}^2$) is larger than in GaN ($P_{SP}^{GaN} = -0.029 \text{ C/m}^2$) [9].

Piezoelectric Polarization

A crystal which becomes electrically polarized in the presence of applied mechanical stress is described as piezoelectric. Piezoelectric polarization is observed in crystals lacking a center of inversion, such as GaN and AlGaN. Piezoelectric polarization is described by the piezoelectric tensor $[e]$ and strain tensor $[\epsilon]$

$$P_{PE} = [e][\epsilon]. \quad (2-2)$$

The piezoelectric tensor is a 3 x 6 matrix and the strain vector can be written with six dimensional components. In wurtzite GaN, the piezoelectric polarization is given by,

$$\begin{bmatrix} P_{PE,x} \\ P_{PE,y} \\ P_{PE,z} \end{bmatrix} = \begin{bmatrix} 0 & 0 & 0 & 0 & e_{15} & 0 \\ 0 & 0 & 0 & e_{15} & 0 & 0 \\ e_{31} & e_{31} & e_{33} & 0 & 0 & 0 \end{bmatrix} \begin{bmatrix} \epsilon_{xx} \\ \epsilon_{yy} \\ \epsilon_{zz} \\ \epsilon_{yz} \\ \epsilon_{zx} \\ \epsilon_{xy} \end{bmatrix}. \quad (2-3)$$

In the case of an AlGaN/GaN HEMT, the GaN layer is significantly thicker relative to the AlGaN barrier layer, so the AlGaN barrier strains to lattice match the relaxed GaN layer. Strain which is generated from this lattice mismatch is in the out-of-plane direction (along the c-axis) defined by the lattice distortion as $\epsilon_{zz} = (c - c_0)/c_0$. Also, an isotropic in-plane strain results, where $\epsilon_{xx} = \epsilon_{yy} = (a - a_0)/a_0$, where a and c are the strained and a_0 and c_0 are the unstrained lattice constants. The polarization induced by lattice mismatch strain in AlGaN/GaN HEMT devices grown along the $\langle 0001 \rangle$ direction only exists in the $\langle 0001 \rangle$ direction. Therefore, the piezoelectric polarization resulting

from lattice mismatch strain in the AlGa_N layer of an AlGa_N/Ga_N HEMT can be expressed as:

$$P_{PE,lattice} = e_{33}\epsilon_{zz} + e_{31}(\epsilon_{xx} + \epsilon_{yy}). \quad (2-4)$$

Stress $[\sigma]$ and $[\epsilon]$ can be related by Hooke's law, where,

$$[\sigma] = [\epsilon][C], \quad (2-5)$$

and analogously

$$[\epsilon] = [S][\sigma]. \quad (2-6)$$

The stiffness tensor $[C]$ and compliance tensor $[S] = [C]^{-1}$ are 6x6 element tensors of the following form for hexagonal symmetry

$$[C] = \begin{bmatrix} C_{11} & C_{12} & C_{13} & 0 & 0 & 0 \\ C_{12} & C_{11} & C_{13} & 0 & 0 & 0 \\ C_{13} & C_{13} & C_{33} & 0 & 0 & 0 \\ 0 & 0 & 0 & C_{44} & 0 & 0 \\ 0 & 0 & 0 & 0 & C_{44} & 0 \\ 0 & 0 & 0 & 0 & 0 & C_{66} \end{bmatrix} \quad (2-7)$$

$$[S] = \begin{bmatrix} S_{11} & S_{12} & S_{13} & 0 & 0 & 0 \\ S_{12} & S_{11} & S_{13} & 0 & 0 & 0 \\ S_{13} & S_{13} & S_{33} & 0 & 0 & 0 \\ 0 & 0 & 0 & S_{44} & 0 & 0 \\ 0 & 0 & 0 & 0 & S_{44} & 0 \\ 0 & 0 & 0 & 0 & 0 & S_{66} \end{bmatrix} \quad (2-8)$$

The polarization resulting from built-in lattice mismatch stress in the AlGa_N layer of an AlGa_N/Ga_N HEMT can be simplified in terms of atomic distortion, piezoelectric constants, and stiffness constants, giving

$$P_{PE,lattice} = 2 \frac{a - a_0}{a_0} \left(e_{31} - e_{33} \frac{C_{13}}{C_{33}} \right). \quad (2-9)$$

Formation of 2DEG

The net positive fixed sheet charge at the AlGa_xN/GaN heterostructure interface (σ_{int}) results from the polarization difference between AlGa_xN and GaN, which induces the mobile 2DEG. Figure 2-2 shows a plot of the polarizations for a strained Al_xGa_{1-x}N ($x = 0.26$) layer on relaxed GaN. The spontaneous polarization in AlGa_xN and GaN, as well as the piezoelectric polarizations in the AlGa_xN layer, are oriented downward, toward the substrate. The sum of spontaneous and piezoelectric polarizations, or the total polarization in the AlGa_xN layer (P_{total}^{AlGaN}) is larger than the total polarizations in GaN (P_{total}^{GaN}). The net polarization ($\sigma_{PZ} = P_{total}^{AlGaN} - P_{total}^{GaN}$) is equivalent to a positive fixed sheet charge density at the AlGa_xN/GaN interface. In a device with interface trapped charge (Q_{it}), the interface sheet charge is reduced by Q_{it} ,

$$\sigma_{int} = \sigma_{PZ} - Q_{it} = (P_{SP}^{AlGaN} + P_{PE,lattice}^{AlGaN} - P_{SP}^{GaN}) - Q_{it}. \quad (2-10)$$

In actual devices, surface roughness, variations in Al composition, and strain gradients can alter the local polarization induced 2DEG, but the total 2DEG density is nearly equal to the theoretical value [9]. Free electrons accumulate at the AlGa_xN/GaN interface to compensate the effective positive fixed sheet charge corresponding to the net polarization. Unlike operation of Si MOSFETs, the conductive channel is not formed through inversion since in GaN, the intrinsic carrier density is low ($n_i = 10^{-10} \text{ cm}^{-3}$). Electrons originating from surface states on the surface of the AlGa_xN barrier accumulate at the AlGa_xN/GaN interface to form the 2DEG in the GaN, as described by Ibbetson's surface donor model [42]. Figure 2-3 shows a schematic of the space charges for an ideal AlGa_xN/GaN. The 2DEG sheet carrier density (n_s) is described by Equation 2-11.

$$n_s = \frac{\sigma_{int}}{q} - \left(\frac{\epsilon_0 \epsilon_r}{q^2 t_{AlGaN}} \right) [\phi_b + E_F - \Delta E_C]. \quad (2-11)$$

The maximum 2DEG sheet carrier density (n_{s0}) occurs at $V_G = 0$ V.

$$n_{s0} = \frac{\sigma_{int}}{q} - \left(\frac{\epsilon_0 \epsilon_r}{q^2 t_{AlGaN}} \right) [\phi_b + E_{F0} - \Delta E_C] \quad (2-12)$$

The electronic charge is q , the dielectric constant of AlGaN is ϵ_r , the thickness of the AlGaN barrier is t_{AlGaN} , the Schottky barrier height of the gate is $\phi_b = (1.3x + 0.84)eV$, the conduction band offset in the AlGaN/GaN interface is ΔE_C , and the Fermi level with respect to the GaN conduction band is E_F . At equilibrium, the Fermi level can be described as,

$$E_{F0} = E_0 + \frac{\pi \hbar^2}{m^*} n_s, \quad (2-13)$$

where E_0 is given by

$$E_0 = \left\{ \frac{9\pi \hbar^2 e^2}{8\epsilon_0 \sqrt{8m^*}} \frac{n_s}{\epsilon_r} \right\}, \quad (2-14)$$

and m^* is the effective mass of AlGaN. The parameters n_s , σ_{int} , ϕ_b , E_{F0} , ΔE_C , ϵ_r , and m^* are all a function of the Al mole concentration.

Device Description

State-of-the art, commercially available AlGaN/GaN HEMTs [43] were characterized in this dissertation. Figure 2-4 shows a cross-section scanning electron microscope (SEM) image of the devices. The GaN and $Al_xGa_{1-x}N$ ($x = 0.26$) layers were deposited through metalorganic chemical vapor deposition (MOCVD) on high resistivity (111) Si substrates. The AlGaN barrier is 18 nm thick with a ~1.5 nm GaN cap and a 1 μ m GaN channel layer. Ti/Al/Ni/Au metal stack was used for the ohmic source and drain contacts. The wafers were passivated with a PECVD deposited SiN_x passivation

layer. In a separate lithography step, Ni/Au Schottky gates were formed. Gate-to-source spacing of 1.0 μm , gate lengths of 0.5 μm and 1 μm , and gate-drain spacing of 3.2 μm , gives a total channel length of 4.7 μm . The channel width is 50 μm . The substrate was thinned to a thickness of 150 μm using standard Si grinding techniques. Devices with and without field plates were analyzed. Typical DC I_D - V_G characteristics are shown in Figure 2-5 for $V_{DS} = 0.1$ V. Although these devices were fabricated on a 100 mm diameter wafer, the wafer was diced in approximately 1 cm^2 samples to maximize the number of usable devices for mechanical wafer bending experiments used to study the effect of stress on the AlGaIn/GaN HEMTs.

Mechanical Wafer Bending Experiment Setup

Mechanical wafer bending is a simple and cost effective way to investigate the underlying physics of strain in semiconductors. Fabricating several wafers with varying amounts of process-induced stress is expensive, and it can be difficult to accurately quantify the amount of stress present in to the device. Also, modifying the process flow to alter the internal stresses can impact other characteristics of the device. Therefore mechanical wafer bending is fundamental in performing controlled stress experiments.

Several methods have been used to externally apply external mechanical stress to semiconductors. The first piezoresistance measurements by Smith [14] were achieved by hanging weights from slabs of semiconductors. This method requires large samples, therefore only bulk measurements can be taken, and the maximum stress achieved in Smith's study is 10 MPa. Bending of cantilevers, or beams anchored at one end is another possible way to apply stress. While cantilevers are often found in microelectromechanical systems (MEMS) for transducer and resonator applications, the stress profile is nonuniform along the length of the beam, making specification of the

applied stress difficult. Three-point bending can also be used, however, like cantilevers, estimation of stress is difficult since stress varies between the three point loads. In this work, we use a flexure based four-point wafer bending system, capable of applying greater than 1 GPa of uniaxial stress to Si wafers [47] to isolate the effect of stress on AlGaIn/GaN HEMT devices due to the significantly improved uniformity of stress in the region between the inner load points.

Four-Point Bending

In four-point bending, a beam is supported by two anchored points while being deformed by two driving loads as shown in Figure 2-7. Between the center two rods, the sample is bent with a constant radius of curvature resulting in uniform stress. Therefore, unlike cantilevers and three-point bending, variation of device position does not affect the accuracy of the measurements. The magnitude of uniaxial stress on the top surface of a homogenous material sample between the center two rods can be represented as [44]

$$\sigma = E \cdot \varepsilon = E \cdot \frac{t \cdot d}{2a \left(\frac{L}{2} - \frac{2a}{3} \right)}, \quad (2-15)$$

where, E is Young's modulus, t is the sample thickness, and L and a are rod spacing distances indicated in Figure 2-6. The magnitude of applied stress was calibrated by comparing the calculated stress to readings from a noncontact fiber optical displacement system and strain gauge measurements [45].

Bending Measurements of Small Samples

AlGaIn/GaN HEMT samples were diced into $\sim 1 \text{ cm}^2$ size to maximize the number of measureable samples since wafer bending tests are potentially destructive and AlGaIn/GaN HEMT wafers are costly. However, the samples are smaller than the

minimum size that can be directly bent in the four-point wafer bending setup. So, to apply stress to these small samples, we developed a technique to bend small wafer samples in the standard flexure based wafer bending setup.

This technique of applying mechanical stress to a small AlGaIn/GaN HEMT wafer sample starts by attaching the wafer sample to a heat treated high carbon stainless steel plate (Figure 2-7). First, the steel strip was sanded with fine grit sand paper to remove oxidation and to provide a rough surface for adhesion. A thin layer of Epoxy Technology H74 two part epoxy was then applied to the middle of the steel strip. The wafer sample was placed on top of the epoxy and pressed down, and excess epoxy was wiped away. To eliminate air pocket formation during curing of the epoxy, a metal washer was placed on top of the wafer sample, and the sample was clamped with a metal binder clip. Then, the sample was inserted into a 100°C oven for 5 minutes. The washer and metal binder were removed and the sample was placed on a 150°C hotplate for 5 minutes to complete the curing process. The sample attached to the steel plate was then inserted into the wafer bending setup.

Under the amount of stress applied (360 MPa) in the experiments, the stainless steel plate does not permanently deform. A strain gauge is mounted on the top of the III-V wafer with epoxy to calibrate the stress. As shown in Figure 2-8, stress is applied and released to the sample. The amount of stress read from the strain gauge returns to the starting point, verifying that stress applied to the sample is elastic.

To characterize the impact of mechanical stress on the AlGaIn/GaN HEMT devices, electrical measurements need to be taken while simultaneously varying the amount of applied stress. In order to achieve this, wires were attached to the device

bond pads. Standard ball and wedge wire-bonding techniques resulted in delamination of bond pads destroying the device. Therefore, a novel technique was developed to attach wires to the bond pads without the use of heat or ultrasonic energy. First, a ball was formed on the end of a 1 mil Au wire in a ball bonding machine. Then, the wire was cut to approximately 1 cm length and removed from the ball bonder. A small amount of electrically conductive Epoxy Technology EE129-4 two part epoxy, was placed on the end of a probe tip. The probe tip was brought into contact with the end of the wire without the ball and cured for 24 hours at room temperature. The ball end of the wire was dipped in conductive epoxy and the probe tip was inserted into the micropositioner. Using the micropositioner, the ball end of the wire with conductive epoxy was landed on the device's bond pad and left to cure for another 24 hours at room temperature. After the epoxy cured, the micropositioner was lowered to allow slack on the wire for displacement of the wafer while applying stress.

Summary

The background on the fundamentals of AlGaIn/GaN HEMT operation and the details of the wafer bending experiments were presented. The accumulation of mobile electrons to form the 2DEG is a result of a net positive charge at the AlGaIn/GaN interface. This interface sheet charge is induced by the difference in polarization between the AlGaIn and GaN layers. The strained AlGaIn layer has piezoelectric polarization as well as spontaneous polarization, whereas the relaxed GaN layer only has spontaneous polarization. To investigate the impact of mechanical stress on AlGaIn/GaN HEMT devices, four-point mechanical wafer bending is used. Wires are attached to the device bond pads to simultaneously take electrical measurements while the level of applied stress is varied.

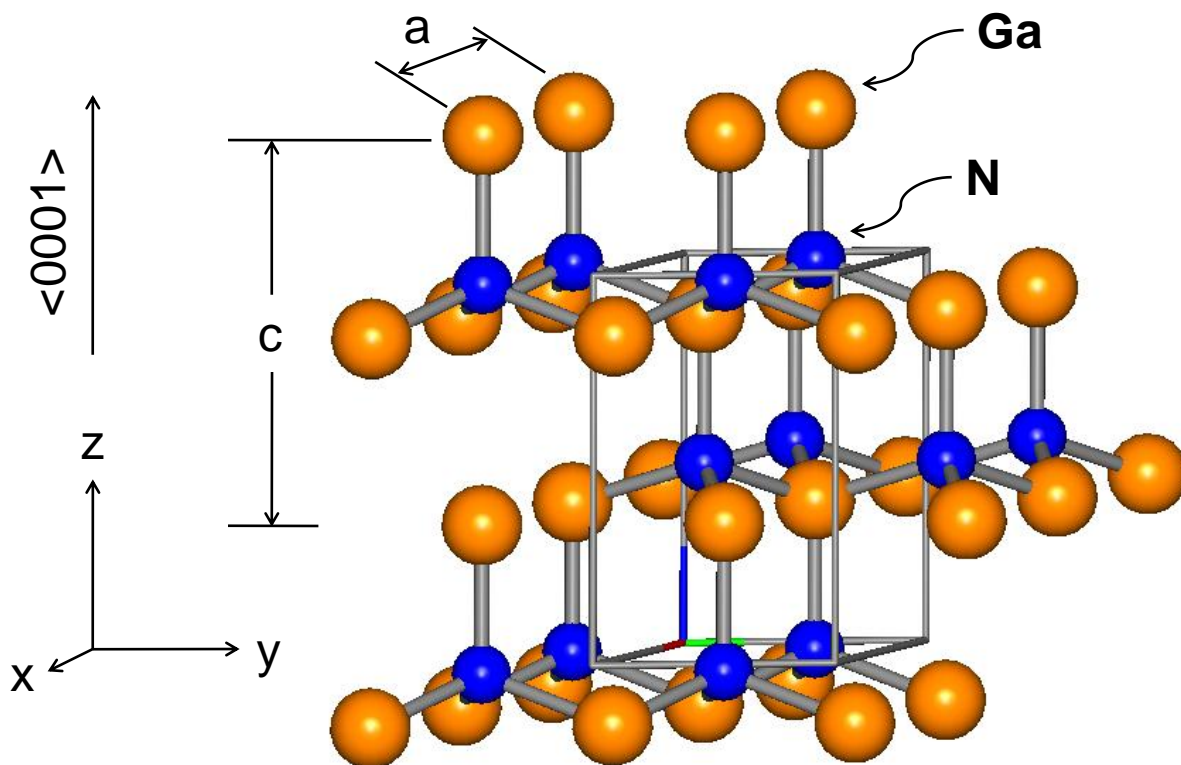


Figure 2-1. GaN-faced GaN crystal lattice, oriented along the $\langle 0001 \rangle$ direction.

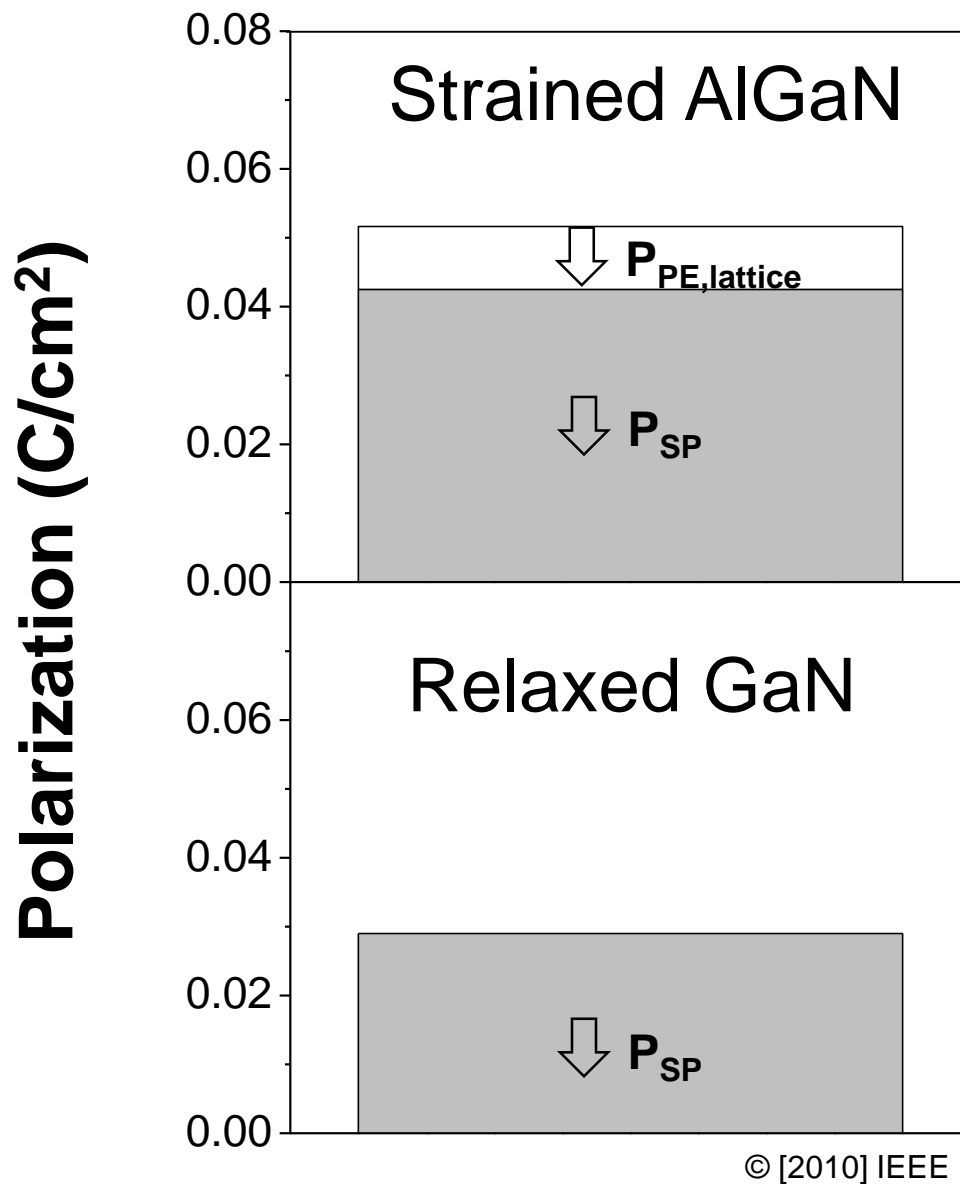


Figure 2-2. Polarizations in strained $Al_xGa_{1-x}N$ ($x = 0.26$), relaxed GaN heterostructure. The strained AlGaIn layer has larger spontaneous polarization than the GaN layer, as well as additional polarization from the piezoelectric effect. [Reprinted, with permission, from A.D. Koehler, et al., Extraction of AlGaIn/GaN HEMT Gauge Factor in the Presence of Traps, IEEE Elec. Dev. Lett., vol. 31, pp 665-667, Figure 3, May 2010]

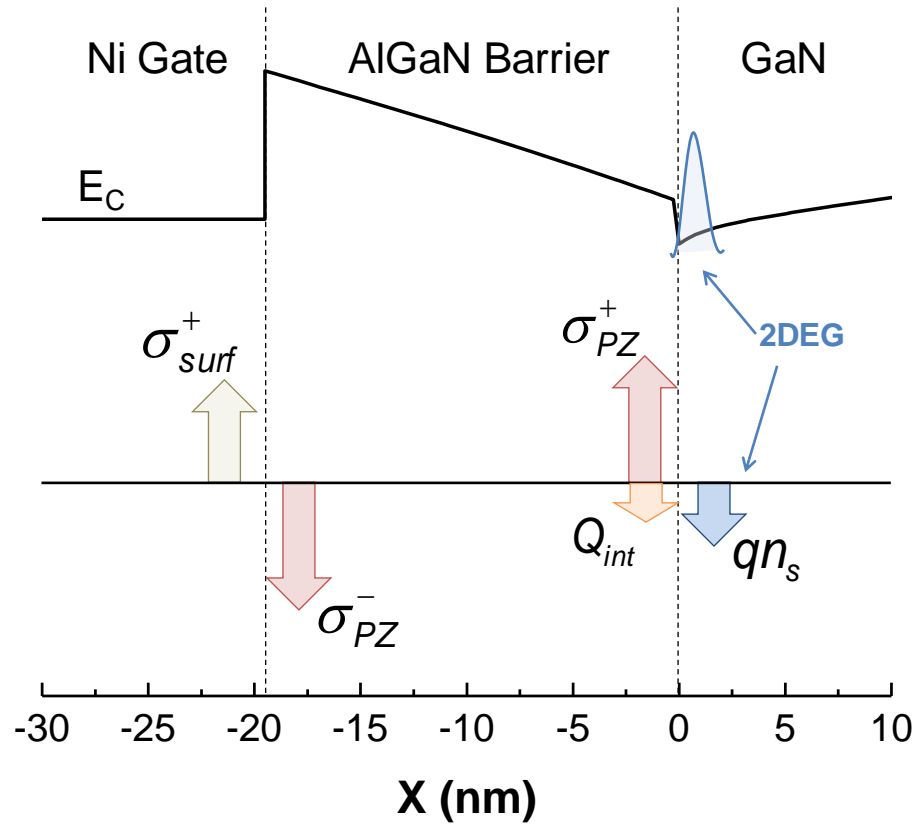


Figure 2-3. Conduction band schematic diagram of an AlGaN/GaN HEMT showing charge balance.

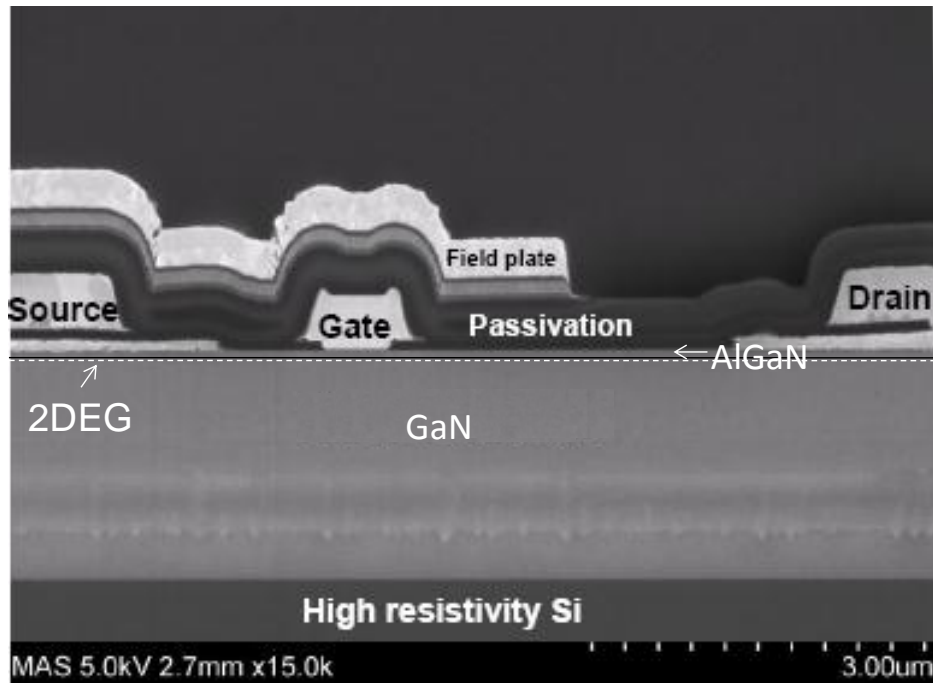


Figure 2-4. Cross-section SEM of commercial devices characterized in this dissertation. Image from Nitronex [46].

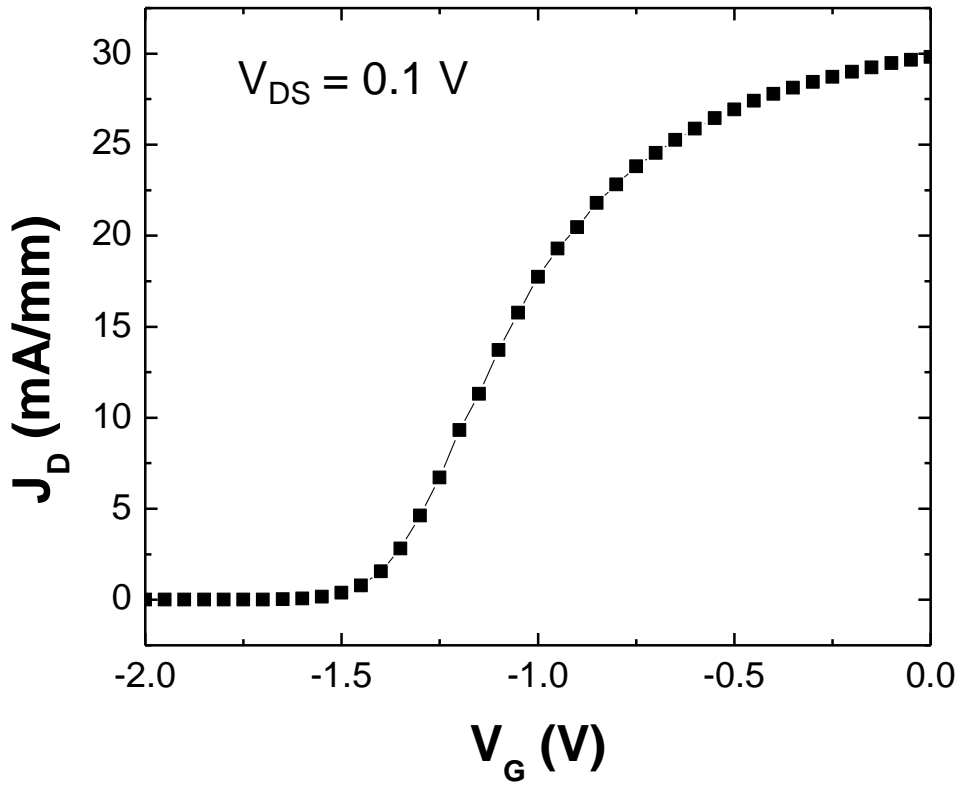


Figure 2-5. Typical I_D - V_G curve of a depletion mode AlGaIn/GaN HEMT measured at $V_{DS} = 0.1$ V.

a.



b.

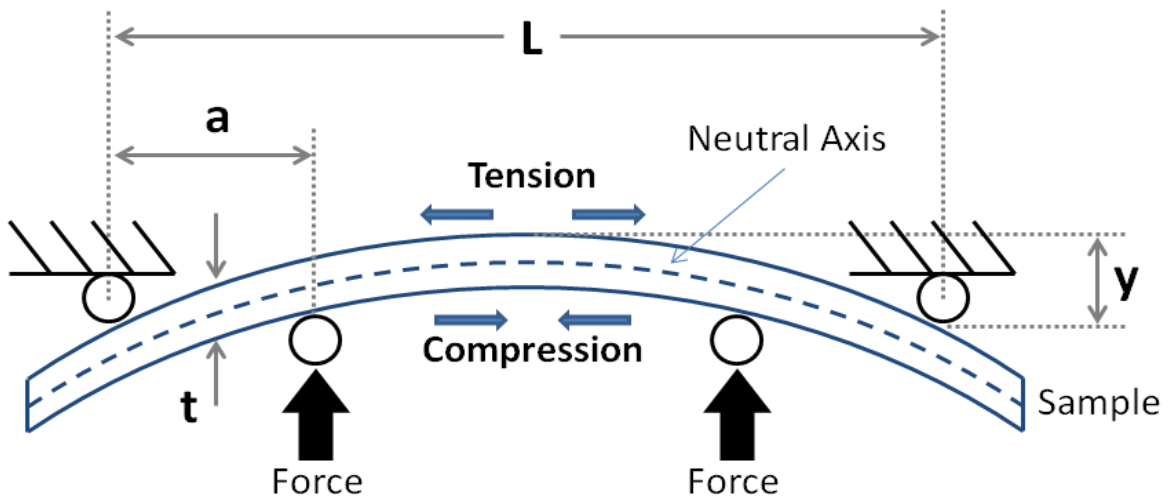


Figure 2-6. Mechanical wafer bending setup: showing (a) a photograph of Si wafer under ~ 1 GPa of stress, and (b) a schematic of wafer under four-point bending, showing tensile stress on the top and compressive stress on the bottom with a neutral axis in the middle.

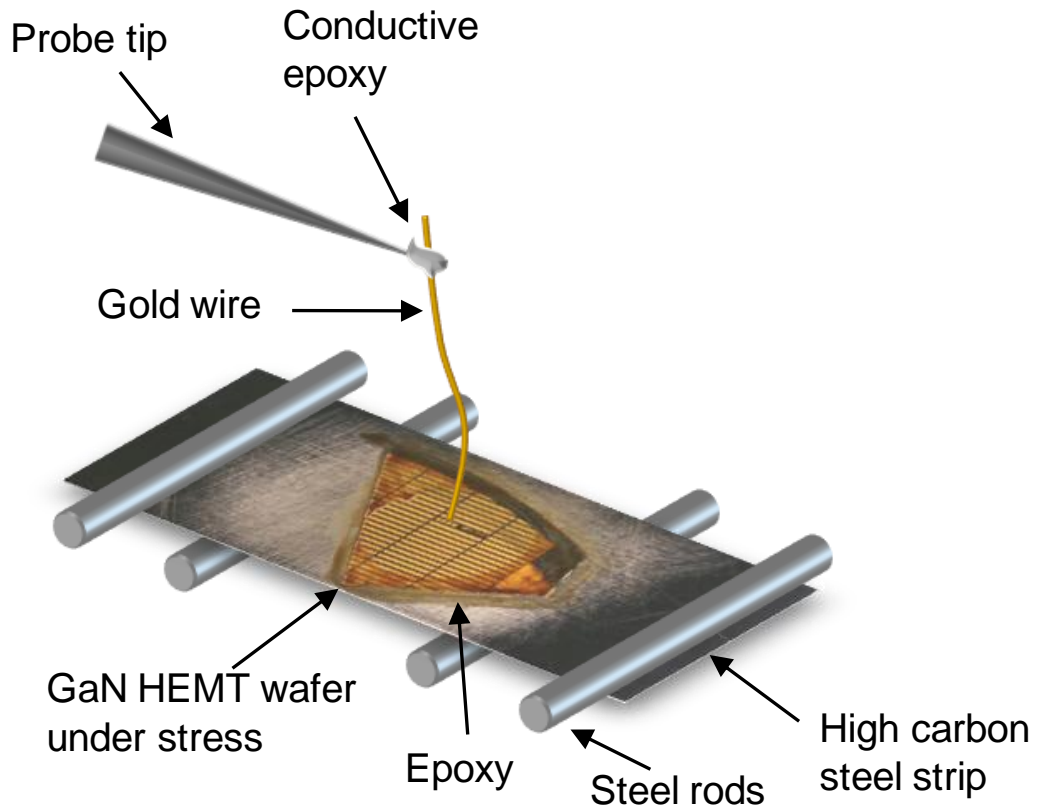


Figure 2-7. GaN wafer sample attached to heat treated high carbon stainless steel inserted in a four-point bending setup.

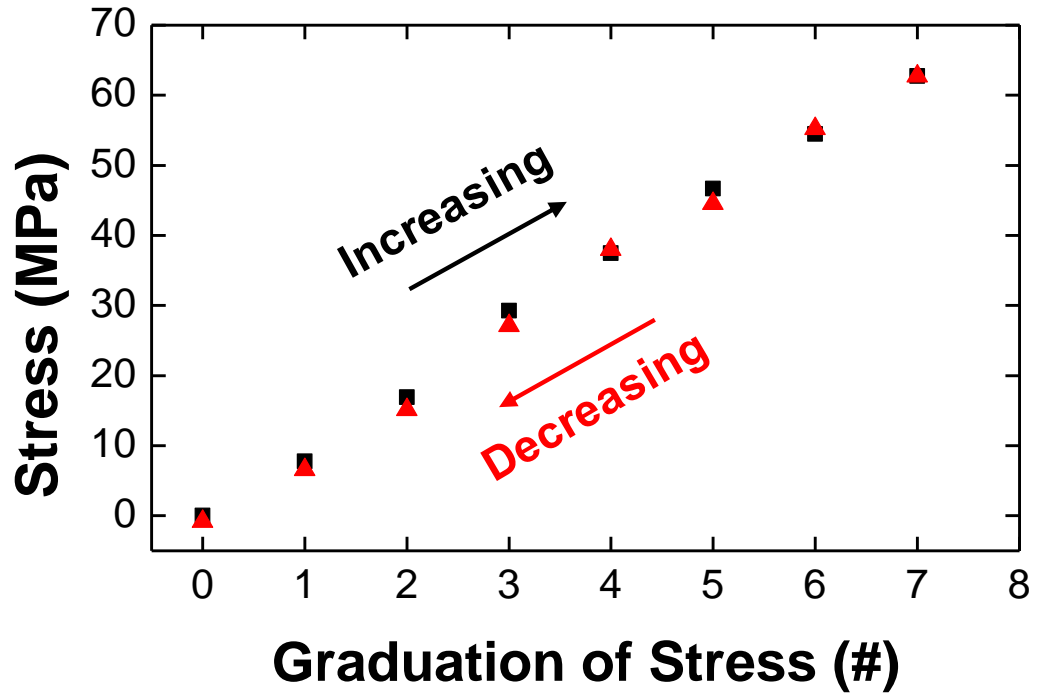


Figure 2-8. Increasing and decreasing stress applied to a wafer mounted on a stainless steel strip. A strain gauge is used to determine the amount of applied stress.

CHAPTER 3 EXTRACTION OF ALGAN/GAN HEMT GAUGE FACTOR IN THE PRESENCE OF TRAPS

Introduction

Sensitivity to change in electrical resistance with stress can be represented by a gauge factor (GF), or the normalized change in resistance (R) per mechanical strain (ϵ) ($GF = (\Delta R/R)/\epsilon$). Obtaining an accurate measurement of the gauge factor of AlGaIn/GaN HEMTs is essential in understanding device degradation as well as improving design of piezoresistive sensors. A large discrepancy in gauge factors (GF) ranging from -4 to -40,000 for AlGaIn/GaN HEMTs are reported in literature (E. Y. Chang, 2009; Eickhoff, Ambacher, Krotz, & Stutzmann, 2001; Gaska et al., 1998; Kang et al., 2005, 2004; Yilmazoglu, Mutamba, & Pavlidis, 2006; Zimmermann et al., 2006). This large disagreement likely results from inaccuracies in resolving the applied stress and changes in the trapped charge density over the time elapsed during measurement. These past studies used three-point bending [47-49], cantilevers [50], [52], complex lever mass system [51], and circular membranes [53] to apply stress, which can be difficult to accurately quantify the amount of stress applied to the device and therefore extract the gauge factor. We use four-point bending, while mitigating the effects of charge traps to experimentally characterize the effect of stress on AlGaIn/GaN HEMTs.

Effects of Trapped Charge

The effect of charge trapping due to surface states, traps in the AlGaIn barrier, or bulk traps can lead to measurable changes in device characteristics, such as current collapse [54], gate-lag [55], drain-lag [55], increased gate leakage [11], threshold

© [2010] IEEE. Reprinted with permission from [A.D. Koehler, A. Gupta, M. Chu, S. Parthasarathy, K.J. Linthicum, J.W. Johnson, T. Nishida, S.E. Thompson, Extraction of AlGaIn/GaN HEMT Gauge Factor in the Presence of Traps, IEEE Elec. Dev. Lett., vol. 31, pp 665-667, May 2010]

voltage shift [56], and light sensitivity [57]. These traps can be formed during processing and crystal growth [58], or generated during device operation via the inverse piezoelectric effect [11], or by hot carriers [59]. Trapped electrons between the source and drain can be modeled as a virtual gate in series with the actual metal gate, depleting channel electrons. Therefore, the drain current is a function of both the mechanism supplying electrons to the virtual gate as well as the external bias applied to the metal gate.

Similar to many AlGaIn/GaN HEMTs described in literature, the commercial devices characterized in this dissertation also exhibit charge trapping effects. The drain current and threshold voltage depend strongly on the concentration of trapped charge in the device. Biasing the device during measurements can alter the concentration of trapped charge, increasing or decreasing the device's threshold voltage. This instability in the devices can be demonstrated by first initializing the device with a large V_G pulse ($V_G = -10$ V held for 1 minute), filling available trap states with electrons (right side of Figure 3-1). Then, 40 consecutive V_G sweeps from -2 V to 0 V were performed over 1200 seconds in the dark. These sweeps are unable to maintain the large charge density of trapped electrons which were filled from the large V_G pulse. This results in electrons thermally detrapping. This in turn, shifts the threshold voltage less negative. Shining the incandescent microscope light on a device without a field plate photoionizes trapped charges (left side of Figure 3-1). Consecutive sweeps of V_G from -2 V to 1 V in the dark fills the available traps, shifting the threshold voltage more negative. The threshold was demonstrated to shift ~ 0.1 V during 1200 seconds of measurement as shown in Figure 3-2. Also, it was observed that simply turning on the incandescent

microscope light during measurement causes a 15% reduction in channel resistance (Figure 3-3). In fact, although an enormous gauge factor of -40,000 was reported, the measured change in resistance was only 15% [53], which could easily result from a change in trapped charge during the experiment. To eliminate parasitic charge trapping effects, we developed a technique to expose the sample to continuous sub-bandgap optical excitation to photoionize trapped charge in order to obtain an accurate gauge factor measurement.

Experimental Setup

Wafer samples were attached to heat-treated high-carbon steel plates with epoxy and stressed in a four-point wafer bending setup. Compressive and tensile uniaxial stress up to 360 MPa was applied longitudinal to the channel direction. To obtain an accurate measurement of the AlGaIn/GaN HEMT gauge factor, parasitic charge trapping transients and external resistances were addressed. After the effects of charge trapping were eliminated, and external resistances were accounted for, an accurate gauge factor measurement was performed.

Elimination of Charge Trapping Effects

To combat the instability issue associated with trapped charges, the HEMT device was exposed to light with a photon energy near, but below the band-gap of GaN (~3.4 eV or 365 nm wavelength) to photoionize all trapped electrons influencing the resistance measurement without band-to-band generation of electron-hole pairs. Initially, a mercury arc ultraviolet (UV) spotlight with peak wavelength of 377.7 nm or 3.284 eV was chosen to illuminate the device under test. A sweep of I_D - V_G under UV spotlight illumination compared to dark (Figure 3-4a) showed a large increase in off-state drain current and a decrease in subthreshold slope. The spectral intensity of the

light source was measured in a spectrometer. A significant portion of the photon energy was above the band-gap of GaN (3.39eV ~ 365 nm) as shown in Figure 3-4b. Under illumination of above bandgap light, mobile electron-hole pairs are photogenerated. An increase in off-state current and a decrease in subthreshold slope are consistent with carrier photogeneration. A 380 nm band-pass filter was measured to filter out wavelengths below 365 nm (Figure 3-5b). A horizontal shift in subthreshold slope and similar off-state leakage current (Figure 3-5a) verifies a decrease in the effect of trapped charge without photogeneration of electron-hole pairs.

A schematic of the experimental setup is shown in Figure 3-6. The standard wafer bending setup described in Chapter 2 is illuminated by the UV light source. The band-pass filter is mounted in a 4 inch thick polystyrene heat shield to block ambient heat from the mercury arc lamp and block nonfiltered light from illuminating the device. As shown in Figure 3-7, over 1500 seconds, the change of the measured channel resistance is less than 0.02%. Since the resistance measurement has been stabilized, it is now appropriate to apply stress to monitor the gauge factor.

External Resistance Consideration

The stress dependence of the channel resistance (R_{CH}) was measured at $V_{GS} = -1V$ and $V_{DS} = 0.1V$, by excluding source/drain contact resistances. The high conductivity of GaN 2DEG results in a small channel resistance, especially for the commercial devices characterized with W/L ratio of 25. The measured resistance (R_{meas}) is the sum of the channel resistance (R_{CH}), source contact resistance (R_S), drain contact resistance (R_D), and external parasitic resistances (R_{ext}) and was on the order of 100 Ω .

$$R_{meas} = R_{CH} + R_S + R_D + R_{ext} \quad (3-1)$$

The source and drain contact resistances ($R_S = R_D = 5 \Omega$), measured by transmission line measurements, are subtracted from the measured resistance and are assumed to have a negligible stress dependence. A four-point Kelvin measurement is used to eliminate the effect of external resistances. Two wires were bonded to both the source and drain pad and one to the gate. One pair of source and drain contacts are used to supply a dc current via the force connections on the semiconductor parameter analyzer. The other pair of connections are used to sense the voltage drop across the source and drain pads.

Results and Discussion

Gauge Factor Measurement

Longitudinal uniaxial stress was varied in 60 MPa increments and held for 100 seconds at each interval. The normalized change in R_{CH} was measured for incrementally applied compressive and tensile stress up to 360 MPa, which was then released incrementally to zero as shown by the dotted lines of Figure 3-8. Tensile stress decreases R_{CH} , while compressive stress increases R_{CH} are seen by the solid experimental lines of Figure 3-8. At the maximum applied stress (360 MPa), the normalized resistance change was $\sim 0.83\%/100$ MPa, which is much smaller than what is observed in (001)/ $\langle 110 \rangle$ silicon nMOSFETs of $3.2\%/100$ MPa [60]. The resistance returned to the initial unstressed value after increasing and decreasing the compressive and tensile stress. This demonstrates that the change in resistance observed is due to a reversible strain effect, opposed to charge trapping/detrapping transients.

The gauge factor was determined by averaging the R_{CH} measurements over each time interval during which the stress was held constant (Figure 3-9). Error bars

represent a three standard deviation confidence interval for the measurement. The slope of a total least squares linear fit of the averaged R_{CH} versus strain curve was obtained to determine a gauge factor of -2.5 ± 0.4 . Total least squares analysis included uncertainty of the measurements. The determined gauge factor (-2.5 ± 0.4) is small relative to values in literature ranging from -4 to $-40,000$ [47-53].

Resistance Change with Stress

To provide understanding of the small measured gauge factor, the factors influencing the change in channel resistance with stress are investigated. The channel resistance is inversely related to the 2DEG sheet carrier density and electron mobility (μ_e).

$$R_{CH} = \frac{A}{qn_s\mu_e}, \quad (3-2)$$

where the A is cross sectional area of the 2DEG. In the presence of stress, the normalized change in channel resistance can be written as:

$$\frac{\Delta R_{CH}}{R_{CH}} = -\frac{\Delta n_s}{n_s} - \frac{\Delta \mu_e}{\mu_e}. \quad (3-3)$$

To evaluate the effect of stress on the channel resistance, both the effect of stress on the 2DEG sheet carrier density and mobility needs to be considered.

2DEG Change with Stress

To analyze the effect of stress on the 2DEG sheet carrier density, the additional piezoelectric polarization induced by mechanical wafer bending must be analyzed. Mechanical wafer bending induces additional polarization in the $\langle 0001 \rangle$ direction. Stress resulting from uniaxial mechanical wafer bending is approximately equal in both the AlGaIn barrier and the GaN layer because the AlGaIn barrier (18 nm) and GaN layer

(1 μm) are thin compared to the total thickness of the wafer (150 μm). Therefore, these two layers are near the top surface of the sample, far from the neutral axis of bending, and experience the same magnitude of stress. Spontaneous polarization in both the AlGaN and GaN remains unchanged by wafer bending since it is an intrinsic material parameter. As shown in Figure 3-10 for 1 GPa of uniaxial tensile stress, mechanical wafer bending induced piezoelectric polarization ($P_{PE,mech.}$) adds to the polarization in both the AlGaN and GaN layers [57]. The magnitude of the mechanical wafer bending induced piezoelectric polarization $P_{PE}^{mech.} = [e][\epsilon]$ is calculated for uniaxial stress where σ_{xx} is the only nonzero element in the stress tensor, and $[\epsilon] = [S][\sigma]$. The mechanical wafer bending induced piezoelectric polarization is similar for both AlGaN (0.00148 C/cm²) and GaN (0.00143 C/cm²) since the elastic and piezoelectric coefficients in GaN and AlGaN are similar for a small Al mole fraction (26%). The total polarization at the interface under uniaxial mechanical stress is

$$P_{total,mech.} = (P_{PE,mech}^{AlGaN} + P_{PE,lattice}^{AlGaN} + P_{SP}^{AlGaN}) - (P_{PE,mech}^{GaN} + P_{SP}^{GaN}). \quad (3-4)$$

Relating the total polarization at the interface to n_s according to Ambacher et al. [61] gives an increase in n_s ranging from 0.064% to 1% for 360 MPa of tensile stress. Uncertainty of n_s results from variation in stiffness constants and piezoelectric coefficients reported in literature [62-70].

Electron Mobility Change with Stress

Strain-enhanced mobility can result from reduced average conductivity effective mass from carrier repopulation and band warping, suppression of intervalley scattering from subband splitting, and change in density of states with stress. Unlike Si, GaN is a direct semiconductor with a non-degenerate conduction band minimum at the Γ -point.

Therefore, stress-induced change of the average effective mass due to electron repopulation and scattering can be neglected. Thus, the mobility change is dominated by a change in the effective mass through band warping. Band warping can be simulated using a tight-binding model with a sp^3d^5 basis [71]. Since strain alters the atomic positions, and consequently the bond lengths and bond angles strain modifies the elements of the new Hamiltonian matrix. Solving for the eigenvalues of the strained matrix allows the strain effect on the effective mass to be calculated. Mobility enhancement from a reduction in effective mass was determined to be 0.29% to 0.49% for 360 MPa of stress [72].

Simulated Gauge Factor

Figure 3-10 shows the experimental normalized change in R_{CH} with stress (symbols) compared to the calculation (shaded bands). The change in 2DEG sheet carrier density and mobility is combined using Equation 3-3 to calculate the normalized change in resistance. Depending on the coefficient values used in the calculation, the change in R_{CH} can range from 0.29% to 1.5% for 360 MPa of stress illustrated as shaded bands in Figure 3-11. This corresponds to a GF of -7.9 ± 5.2 . Comparing the experimental results with the model, the best fitting set of elastic and piezoelectric coefficients from literature is $C_{ij}(\text{GaN})$ [73] $C_{ij}(\text{AlN})$ [74] $e_{ij}(\text{GaN})$ [75] $e_{ij}(\text{AlN})$ [76].

Summary

Illuminating the AlGaIn/GaN HEMT device with photon energy near but below the band-gap of GaN provided a reliable gauge factor measurement. After eliminating trap charging effects, the gauge factor of the AlGaIn/GaN HEMT was determined to be -2.8 ± 0.4 . A reliable gauge factor measurementThe small gauge factor indicates a small stress dependence on the device resistivity. This is explained by small changes in the

2DEG sheet carrier density and channel mobility. The experimental results were compared with simulated gauge factor (-7.9 ± 5.2) to determine the best fitting set of elastic and piezoelectric coefficients of GaN and AlN.

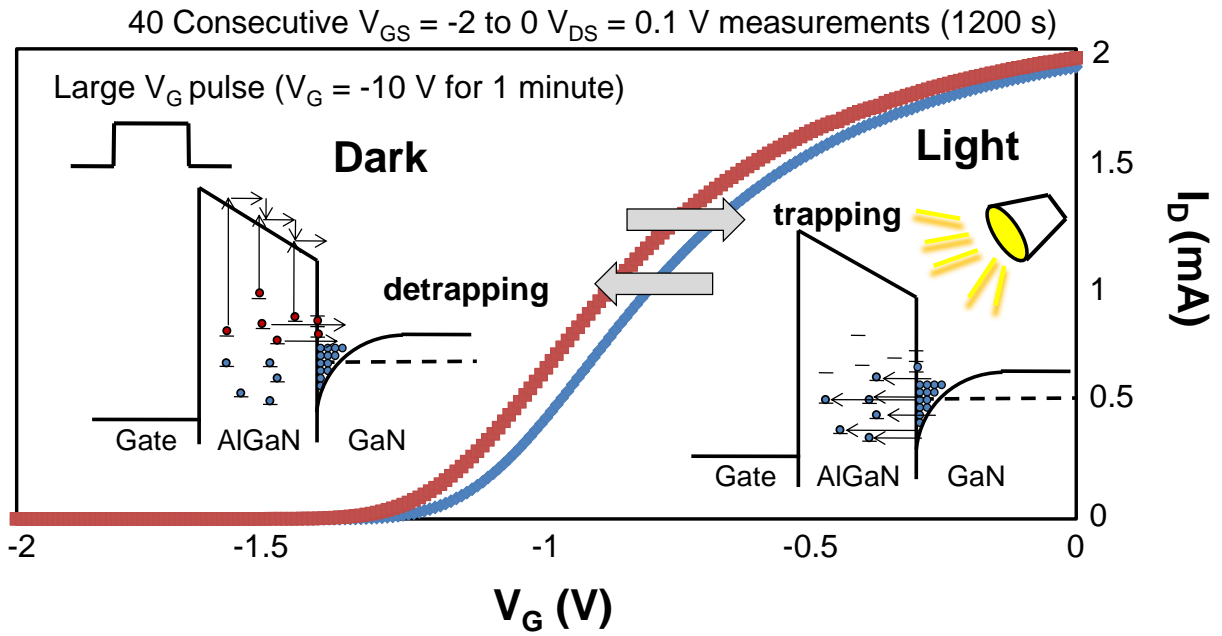


Figure 3-1. Results of consecutive $V_{GS} = -2$ to 0 $V_{DS} = 0.1$ V measurement sweeps resulting in charge trapping and detrapping.

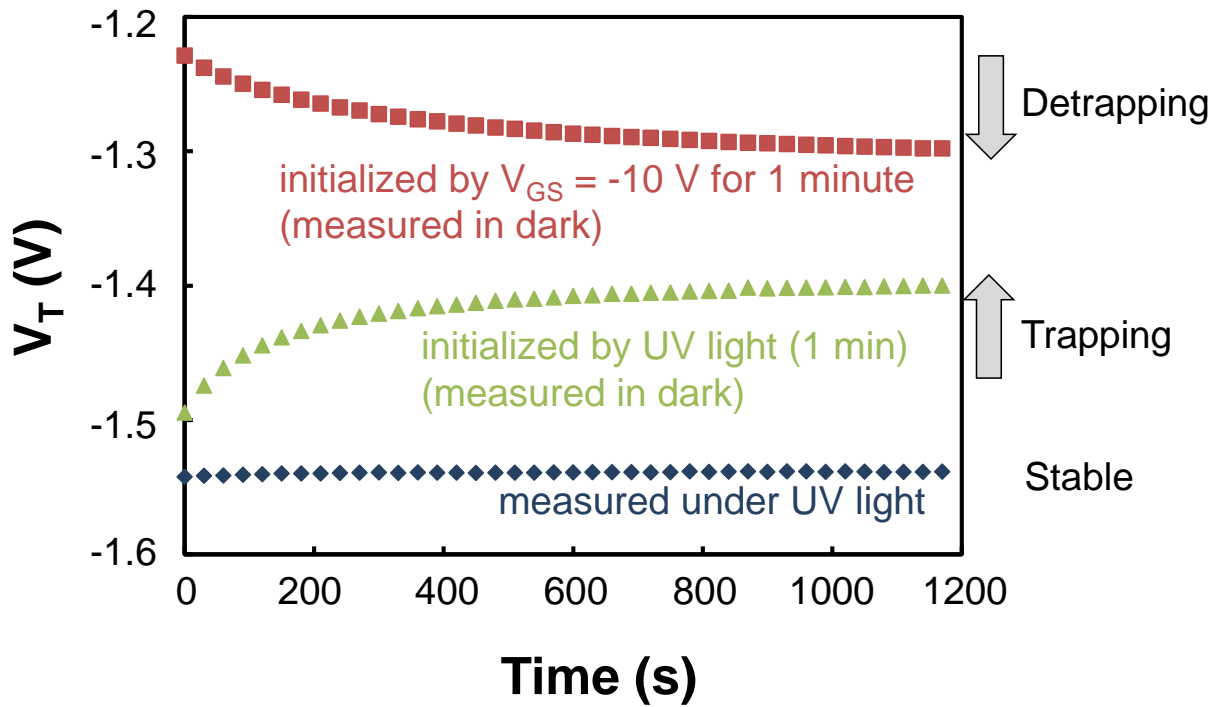


Figure 3-2. V_T measured in consecutive $I_D - V_G$ sweeps. In dark, $|V_T|$ can increase (decrease) from detrapping (trapping) of electrons, depending the device initialization. Under unfiltered UV illumination, V_T does not fluctuate.

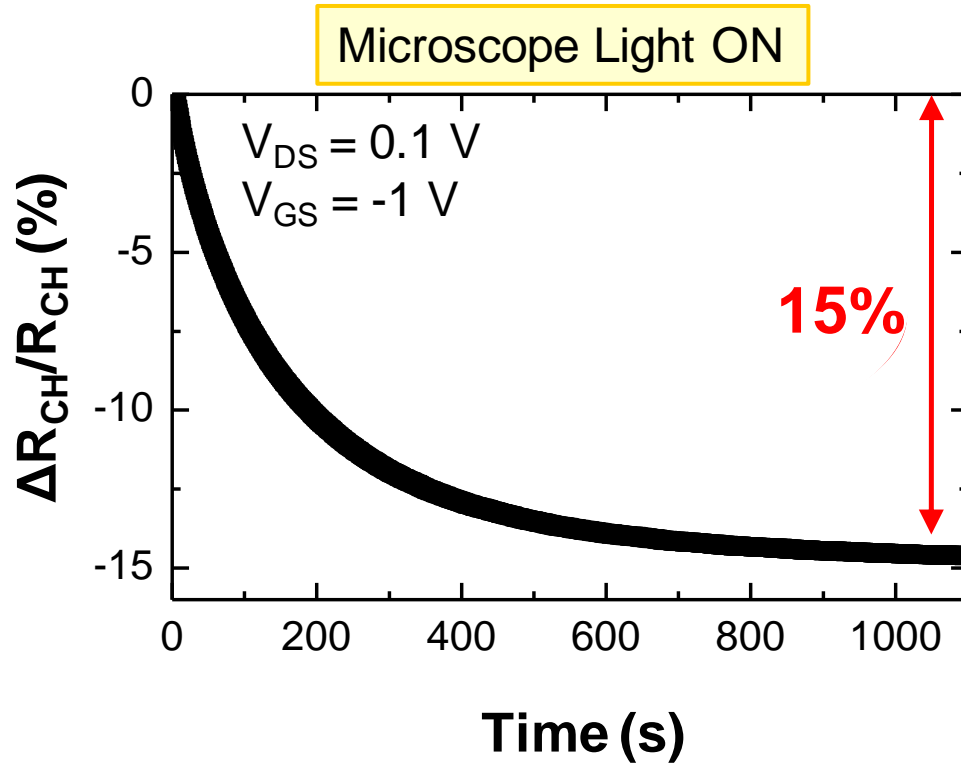


Figure 3-3. A decrease in channel resistance of 15% observed during 1200 seconds of measuring after turning on the incandescent microscope light.

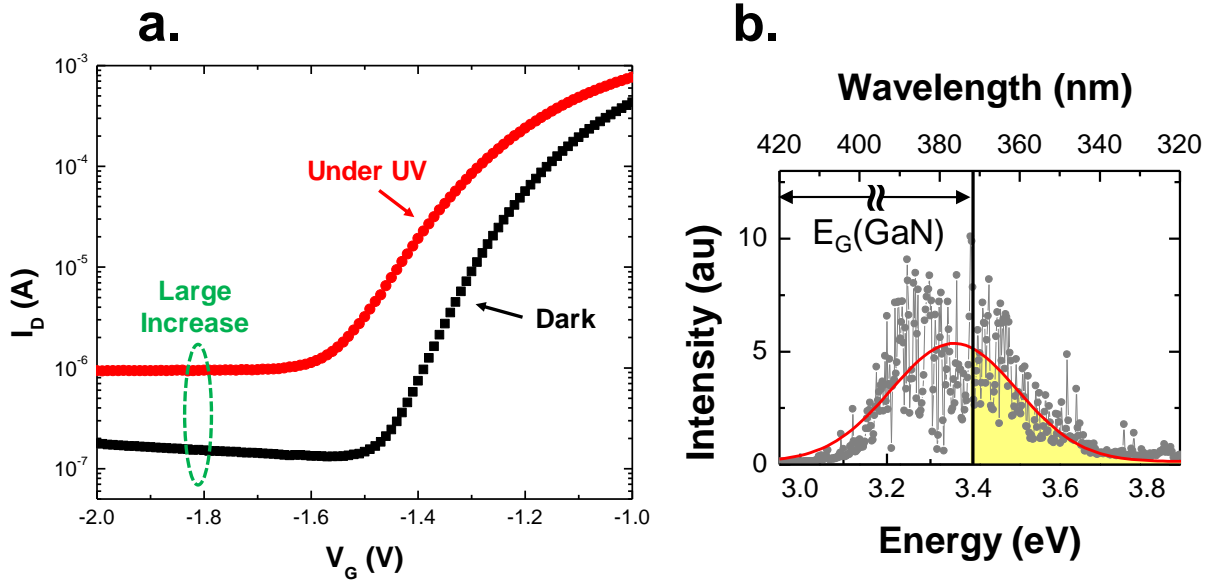


Figure 3-4. Unfiltered UV measurement (a) I_D - V_G measurements in dark and under unfiltered UV light with a large increase in off-state current and a decrease in subthreshold slope. (b) The spectral output of the unfiltered UV light.

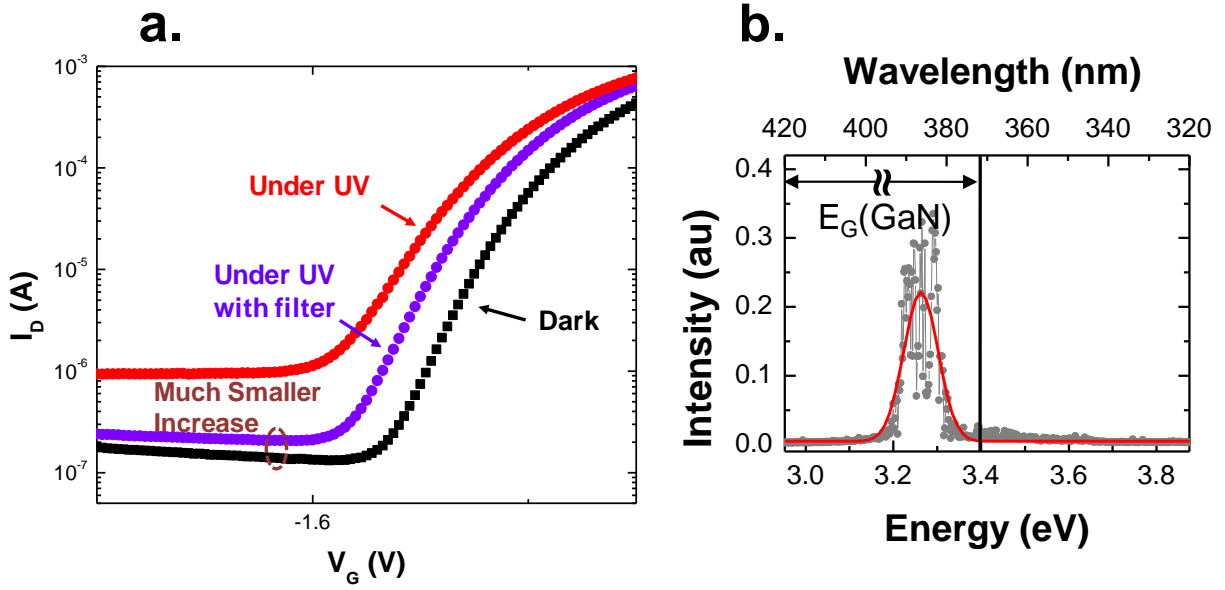


Figure 3-5. Filtered UV measurement (a) I_D - V_G measurements in dark and UV light filtered by a 380 nm bandpass filter with a much smaller increase in off-state current and no subthreshold slope change. (b) The spectral output of UV light with 380 nm bandpass filter.

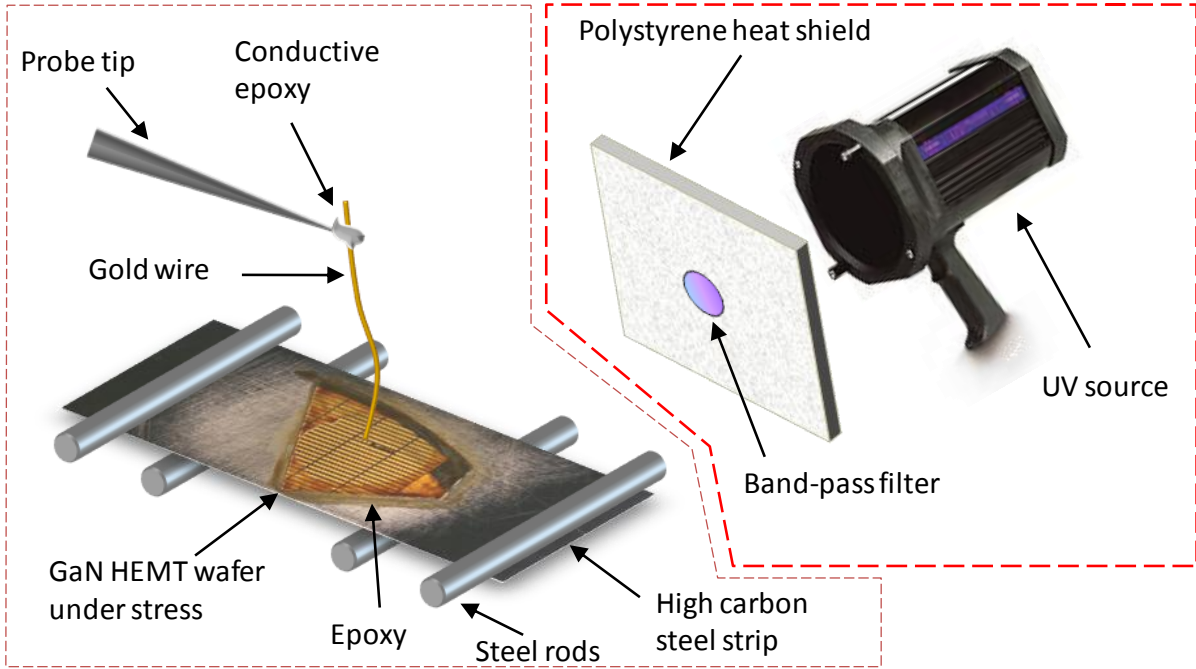


Figure 3-6. Experimental setup for photoionizing trapped charge to measure the gauge factor.

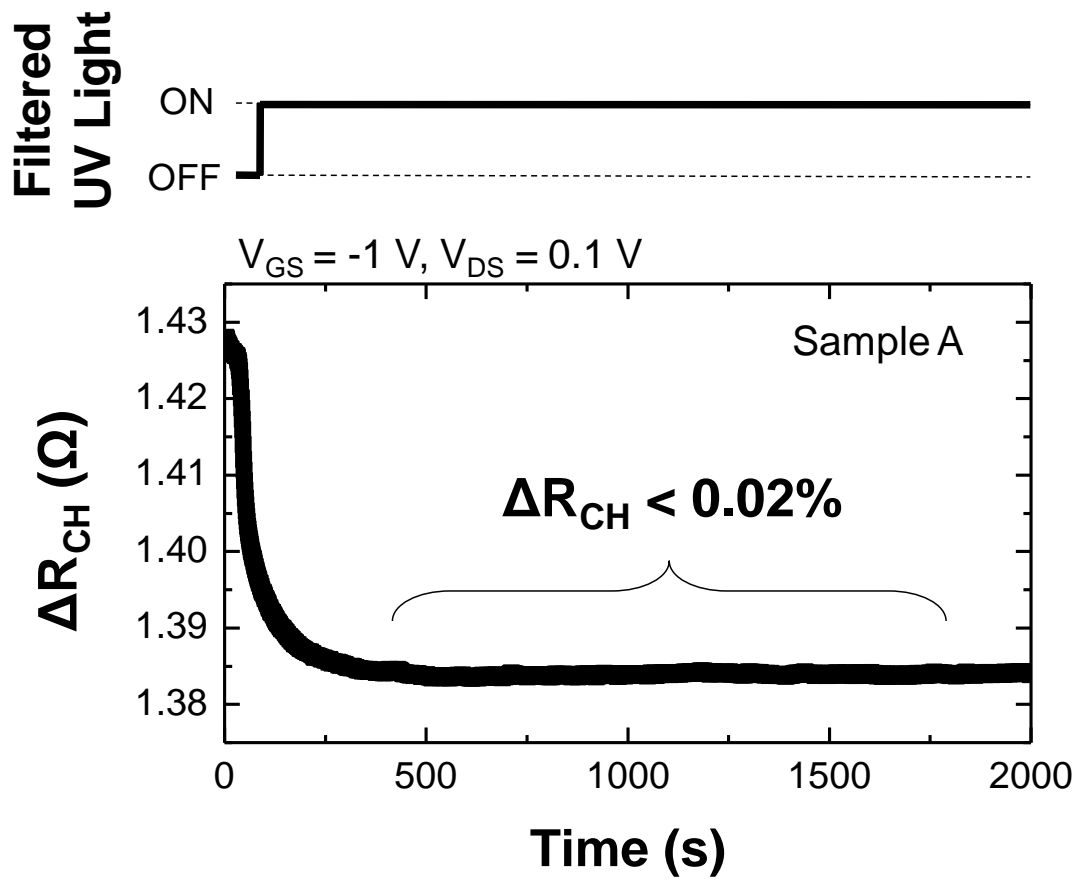


Figure 3-7. Illuminating the device under test with UV light stabilized R_{CH} to less than 0.02% variation for 1200 seconds of measurement.

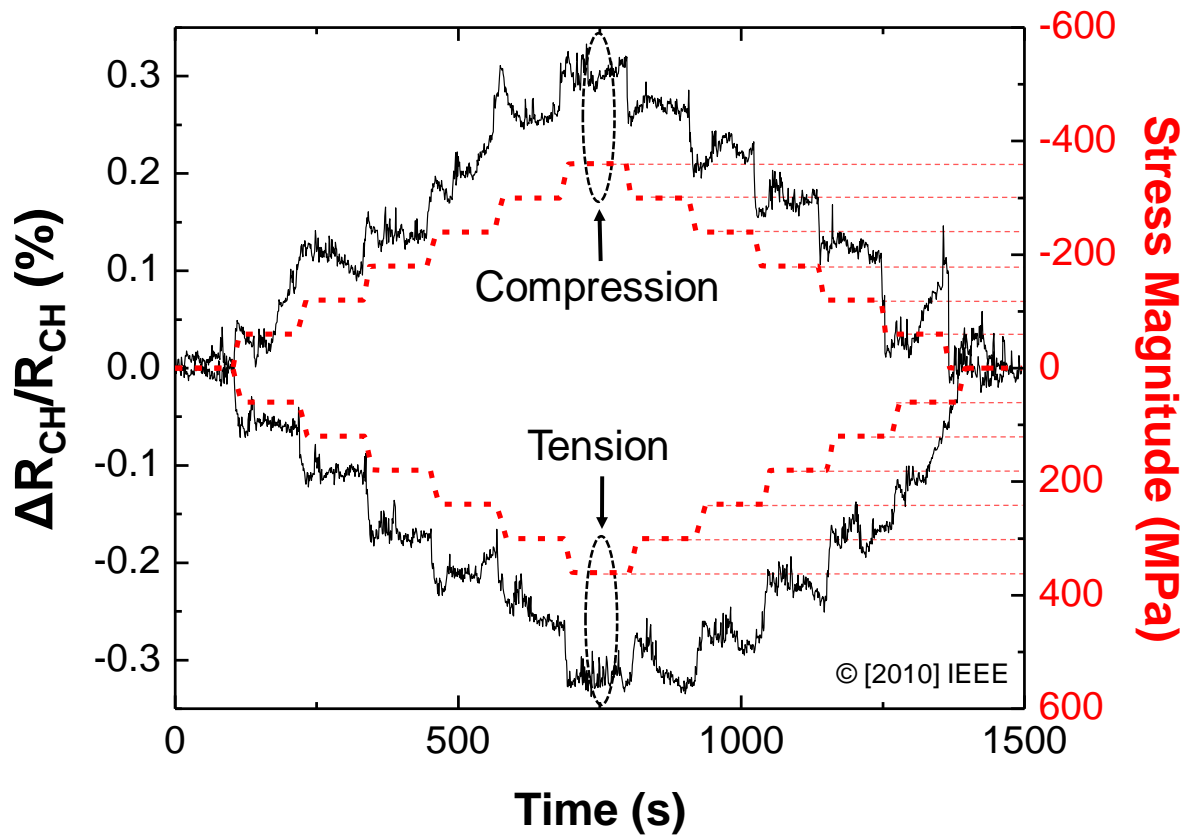


Figure 3-8. Normalized change in channel resistance with incrementally increasing and decreasing uniaxial stress. [Reprinted, with permission, from A.D. Koehler, et al., Extraction of AlGa_N/Ga_N HEMT Gauge Factor in the Presence of Traps, IEEE Elec. Dev. Lett., vol. 31, pp 665-667, Figure 2, May 2010]

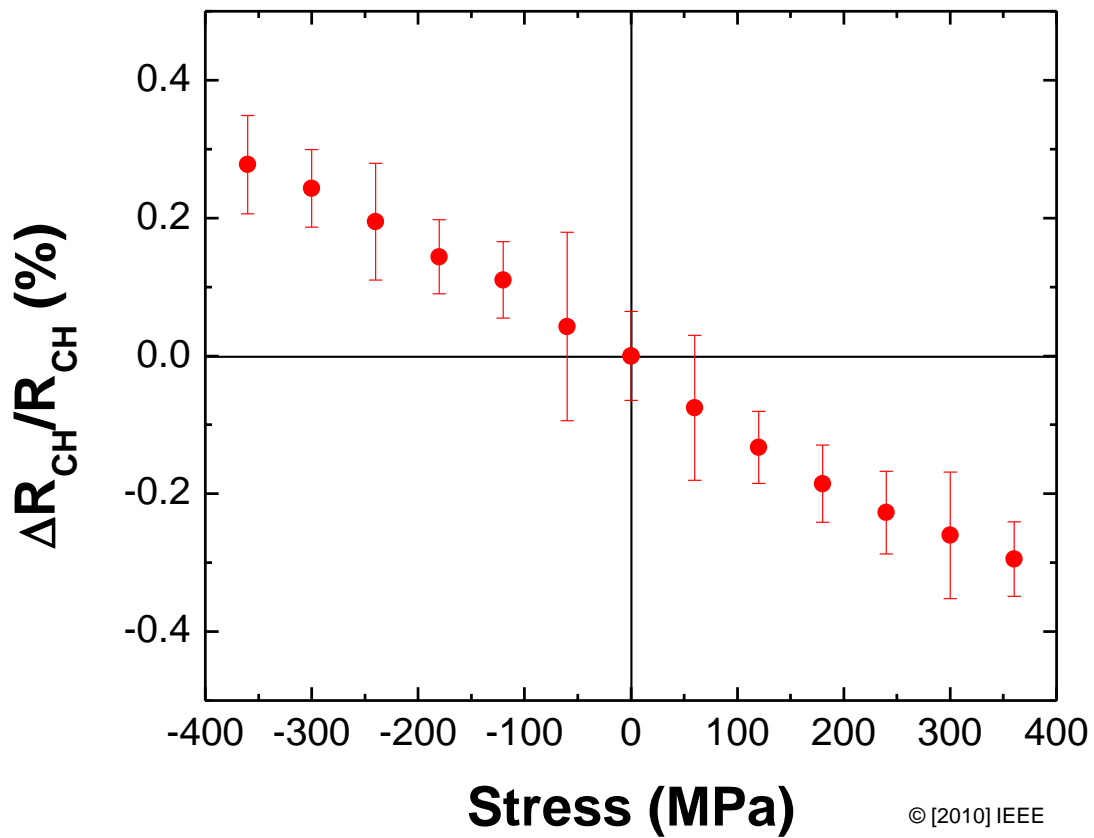


Figure 3-9. R_{CH} measurements at each time interval stress was held constant. Error bars represent a three standard deviation confidence interval for the measurement. [Reprinted, with permission, from A.D. Koehler, et al., Extraction of AlGaIn/GaN HEMT Gauge Factor in the Presence of Traps, IEEE Elec. Dev. Lett., vol. 31, pp 665-667, Figure 4, May 2010]

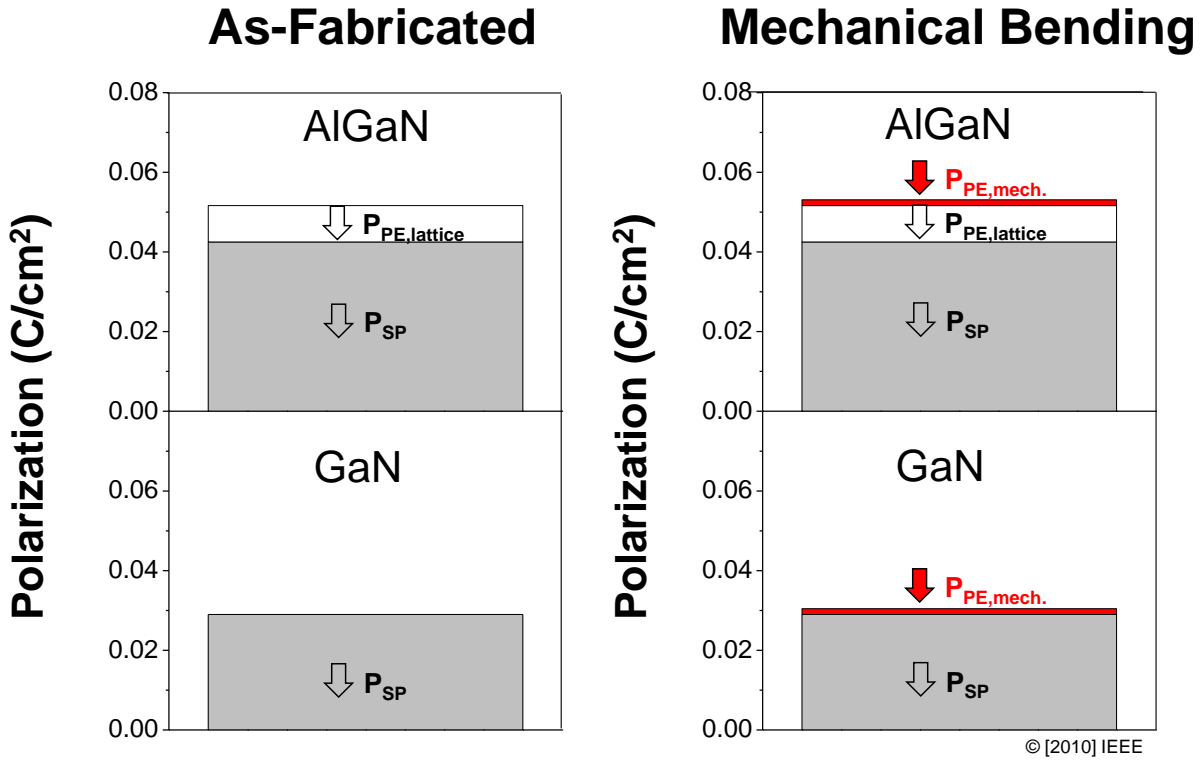


Figure 3-10. Schematic showing polarizations in AlGaIn/GaN HEMTs as fabricated (left), and 1 GPa mechanically applied stress (right) generating additional $P_{PE,mech}$ similar in magnitude for both AlGaIn and GaN layers. [Reprinted, with permission, from A.D. Koehler, et al., Extraction of AlGaIn/GaN HEMT Gauge Factor in the Presence of Traps, IEEE Elec. Dev. Lett., vol. 31, pp 665-667, Figure 3, May 2010]

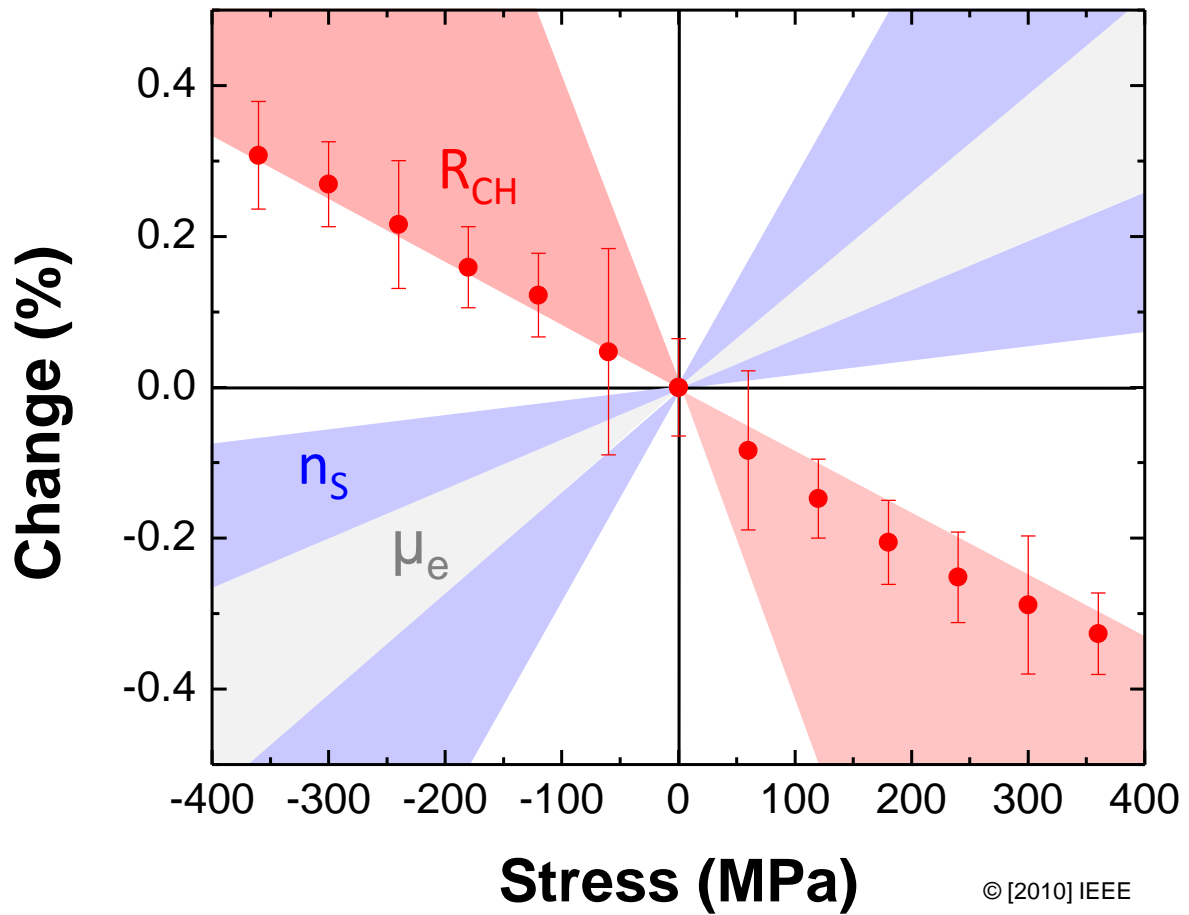


Figure 3-11. Simulated change in n_s , μ_e and R_{CH} with uniaxial stress shown in bands of uncertainty. The bands signify variations in numerical results due to uncertainty in elastic and piezoelectric coefficients. [Reprinted, with permission, from A.D. Koehler, et al., Extraction of AlGaIn/GaN HEMT Gauge Factor in the Presence of Traps, IEEE Elec. Dev. Lett., vol. 31, pp 665-667, Figure 4, May 2010]

CHAPTER 4 VERTICAL ELECTRIC FIELD IN THE ALGaN BARRIER

Introduction

Reliability is a major concern with AlGaIn/GaN HEMTs, and a systematic study of the impact of stress on gate leakage current is essential to gain physical insight into the degradation mechanisms in order to improve device reliability. Gate leakage currents for AlGaIn and GaN Schottky interfaces in literature are significantly larger than what would be theoretically predicted based purely on the thermionic emission model [77]. Determining the dominant gate leakage transport mechanism through the AlGaIn barrier in AlGaIn/GaN HEMT is necessary for investigating the physics behind the effect of stress on the gate leakage current. An accurate determination of the electric field in the AlGaIn barrier (E_{AlGaIn}) is required to investigate the gate leakage models.

Several models have been proposed to explain the gate leakage mechanism in AlGaIn/GaN HEMTs, such as trap-assisted tunneling [34], [78-81], direct or Fowler-Nordheim (FN) tunneling [78-80], [82], temperature assisted tunneling [78], [83], multi-step trap-assisted tunneling [84], thermionic trap assisted tunneling [82], [85-87], tunneling through a thin surface barrier [88], and Poole-Frenkel (PF) emission [89-94]. The dominant leakage mechanism is strongly dependent on the materials and processing conditions and the electric field in the AlGaIn Barrier, E_{AlGaIn} . To characterize the effect of mechanical stress on the state-of-the-art commercial AlGaIn/GaN devices, an accurate model for the leakage mechanism is necessary. To compare different leakage models to the experimental measurements, an accurate calculation of E_{AlGaIn} is needed. In past works, E_{AlGaIn} has been simplified to a linear relationship with the gate voltage [91][89], simulated using Medici 2D simulations [95], and experimentally

measured [96]. The $V_{DS} = 0$ state is of particular interest for exploring reliability since both the source and drain sides of the device gate are electrically stressed simultaneously. A complete investigation of the electric field relationship as a function of V_G at the $V_{DS} = 0$ state will be presented.

Ideal 1D Calculation of E_{AlGaN}

A one-dimensional (1D) calculation of E_{AlGaN} provides insight into the general relationship between voltage and field. In this condition, the gate is assumed to be infinitely wide. Also, for simplicity, E_{AlGaN} is assumed to be a constant throughout the entire thickness of the AlGaN barrier. Based on these assumptions, a simple expression for the electric field in the AlGaN barrier can be derived from the voltage drop across the AlGaN barrier (V_{AlGaN}) from inspection of the energy band diagram (Figure 4-1). E_{AlGaN} can be written as,

$$E_{AlGaN} = \frac{V_{AlGaN}}{t_{AlGaN}} = \frac{\phi_b - (\Delta E_C - E_F)}{qt_{AlGaN}}. \quad (4-1)$$

Recalling Equation 2-11, n_s can be rewritten in terms of E_{AlGaN} ,

$$n_s = \frac{\sigma_{int}}{q} - \left(\frac{\epsilon_0 \epsilon_r}{q^2 t_{AlGaN}} \right) [\phi_b + E_F - \Delta E_C] = \frac{\sigma_{int} - \epsilon_0 \epsilon_r E_{AlGaN}}{q}. \quad (4-2)$$

Then, the simple expression for E_{AlGaN} is

$$E_{AlGaN} = \frac{\sigma_{int} - qn_s}{\epsilon_0 \epsilon_r}. \quad (4-3)$$

In the expression for E_{AlGaN} (Equation 4-3), only the 2DEG sheet carrier density (n_s) is a function of gate voltage. The total fixed charge density at the AlGaN/GaN interface (σ_{int}) is assumed to be independent of bias because it is based on the polarization. Charge trapped at the AlGaN/GaN interface is estimated to be constant

with bias. To analyze the dependence of n_s with gate voltage, n_s is rewritten to include the contribution of V_G in terms of the equilibrium 2DEG concentration n_{s0} .

$$n_s = \frac{\sigma_{int}}{q} - \left(\frac{\epsilon_0 \epsilon_r}{q^2 t_{AlGaN}} \right) [\phi_b + E_{F0} - \Delta E_C + qV_G] = n_{s0} + \left(\frac{C_{AlGaN}}{q} \right) V_G, \quad (4-4)$$

where, $C_{AlGaN} = \frac{\epsilon_0 \epsilon_r}{t_{AlGaN}}$ is the AlGa_N capacitance per unit area. At equilibrium, $V_G = 0$ V and $n_s = n_{s0}$, which is the maximum induced 2DEG sheet carrier density. The fixed positive charge at the AlGa_N/Ga_N interface induces accumulation of electrons at the interface in the Ga_N. The electrons that form the 2DEG originate from the AlGa_N surface [42], not from the source, drain, and substrate as in a Si MOSFET inversion layer. A negative bias applied to the gate depletes the 2DEG, decreasing n_s linearly, as shown by Equation 4-4. The threshold voltage for the depletion mode AlGa_N/Ga_N HEMT is defined as the voltage required on the gate to entirely deplete the 2DEG ($n_s = 0$). Since the AlGa_N/Ga_N HEMT is a depletion mode device with a negative V_T , the device is considered to be turned off below threshold ($|V_G| > |V_T|$). Above threshold, the 2DEG is formed ($|V_G| < |V_T|$). Below threshold, the 2DEG remains depleted. Since the intrinsic carrier concentration of Ga_N is extremely low ($n_i \sim 1 \times 10^{-10}$ cm⁻³ at 300 K), hole accumulation at the surface is negligible. Figure 4-2 shows for an ideal device, without interface trapped charge, the 2DEG sheet carrier density plotted against V_G . The charge at the AlGa_N/Ga_N interface ($\sigma_{int} = 2.2 \times 10^{-6}$ C/cm²) is only a result of the polarization differences between AlGa_N and Ga_N. Parameters described in Table 4-1 were used for the calculation.

To express E_{AlGaN} as a function of gate voltage, the voltage dependent 2DEG equation (Equation 4-4) was incorporated into the expression for E_{AlGaN} (Equation 4-3) to give,

$$E_{AlGaN}(V_G) = \frac{-\left(\frac{\epsilon_0\epsilon_r}{qt_{AlGaN}}\right)[q\phi_b + E_{F0} - \Delta E_C + qV_G]}{\epsilon_0\epsilon_r} \text{ for } V_G > V_T. \quad (4-5)$$

For gate bias below threshold, E_{AlGaN} saturates at $E_{AlGaN} = -\sigma_{int}/(\epsilon_0\epsilon_r)$. Figure 4-3 shows E_{AlGaN} increasing linearly with bias for gate biases above threshold.

1D Experimentally Measured E_{AlGaN}

Estimation of E_{AlGaN} for an actual AlGaN/GaN HEMT device based on the 1D model requires both σ_{int} and n_s to be experimentally measured. The threshold voltage determined by the standard linear extrapolation method ($V_T = -1.4$ V) is not consistent with the definition of $V_G = V_T$ when $n_s = 0$. A more appropriate threshold of -1.9 V is used based on the initial increase of the capacitance-voltage curve (Figure 4-5).

Trapped charge in the actual device reduces the amount of fixed charge at the AlGaN/GaN interface, shifting the threshold voltage more positive than the ideal value. From Equation 4-4 and the definition of threshold ($V_G = V_T$ when $n_s = 0$), the 2DEG sheet carrier density at $V_G = 0$ can be calculated from the measured V_T .

$$n_{s0} = \frac{-C_{AlGaN}V_T}{q} \quad (4-6)$$

Which gives $n_{s0} = 5.3 \times 10^{12} \text{ cm}^{-3}$ for $V_T = -1.9$ V. Then, the fixed charge at the AlGaN/GaN interface can be estimated by solving for σ_{int} in Equation 2-12.

$$\sigma_{int} = qn_{s0} + \left(\frac{\epsilon_0\epsilon_r}{qt_{AlGaN}}\right)[q\phi_b + E_{F0} - \Delta E_C] \quad (4-7)$$

Resulting in $\sigma_{int} = 1.25 \times 10^{-6} \text{ C/cm}^2$, which is nearly half the ideal value ($\sigma_{int} = 2.2 \times 10^{-6} \text{ C/cm}^2$) using the constants in Table 4-1. The interface trapped charge density is estimated from the subthreshold slope (SS) measurements [97], [98]

$$SS \approx \frac{kT}{q} \ln 10 \left[1 + \frac{C_{it}}{C_{AlGaN}} \right]. \quad (4-8)$$

The capacitance associated with the interface trapped charge (C_{it}) can be related to the density of interface traps by $C_{it} = qD_{it}$. For the measured device with $SS = 100$ mV/dec, the interface trap density is $D_{it} = 1.92 \times 10^{12} \text{ cm}^{-2}\text{eV}^{-1}$. Assuming all traps are full, integrating over the bandgap of AlGa_N gives an interface trapped charge $Q_{it} = 1.2 \times 10^{-6} \text{ C/cm}^2$. Figure 4-4 shows a bar chart of the charge density in the ideal device compared to the actual device. In the ideal device ($Q_{it} = 0$) $\sigma_{pz} = \sigma_{int}$. However, in the actual device, fixed charge at the AlGa_N/Ga_N interface induced by polarization is reduced by negative trapped charge.

To obtain E_{AlGaN} for the actual device, the n_s versus V_G relationship needs to be obtained. A high-frequency (1 MHz) capacitance-voltage curve (Figure 4-5) was integrated from pinch-off to voltage V . The experimental bias range was limited to $V_G = -2 \text{ V}$ to 0 V to avoid additional charge trapping from larger applied biases. The value of $n_s(V)$ is also shown in Figure 4-5. The experimentally obtained n_s versus V_G relationship is used in Equation 4-3 to calculate the experimentally obtained E_{AlGaN} versus V_G relationship.

Implementing the experimentally determined σ_{int} and n_s versus V_G relationship provides the experimentally determined 1D calculation of E_{AlGaN} versus V_G . Figure 4-6 shows a comparison between the experimental and ideal 1D calculation for E_{AlGaN} versus V_G . Since both methods are based on the 1D expression, they have similar trends. Above threshold, $|E_{AlGaN}|$ increases linearly with increasing reverse bias, and below threshold E_{AlGaN} saturates at $E_{AlGaN} = -\sigma_{int}/(\epsilon_0\epsilon_r)$. The presence of Q_{it} reduces σ_{int} and the magnitude of the saturated value of E_{AlGaN} below threshold in the actual

device compared to the ideal 1D calculation. In addition, V_T is shifted toward the positive direction by the negative Q_{it} . At $V_G = 0$, the experimental $|E_{AlGaIn}|$ is larger than the ideal 1D case because the experimentally extracted n_{s0} is lower than what is theoretically predicted, making the numerator of Equation 4-3 larger.

2D Simulation of E_{AlGaIn}

Simulation Details

The AlGaIn/GaN HEMT structure was simulated using the Sentaurus device simulator. A two-dimensional (2D) simulation was performed to gain a physical understanding of 2D effects on E_{AlGaIn} . The thin (~1.5 nm) GaN cap layer was neglected in the simulation for simplicity. The device structure is quantized into a mesh or grid of discrete elements. The grid was condensed in areas where large variations of carrier concentration are expected at short distances to optimize computational accuracy (Figure 4-7).

At each point on the grid, three variables are solved for simultaneously. The electrostatic potential, electron concentration, and hole concentration are solved for through Poisson's equation and the electron and hole continuity equations respectively. The boundary conditions used to solve for the three variables are: the metal-contact work function difference, the ohmic contacts at the source and drain, and local conservation of charge. In the actual device, the high resistivity Si layer isolates the GaN layer from the back side of the wafer, leaving it electrically floating. The bulk is left floating in simulation to model this. Shockley-Read-Hall recombination and generation were included in the calculation. Also, a hydrodynamic model was used where the carrier temperature is not assumed to be equal to the lattice temperature. Electron mobility was modeled including doping dependence, high field saturation, and

temperature. Doping was introduced under the source and drain contacts to emulate metal spikes to provide an ohmic contact to the 2DEG [99]. The piezoelectric effect is modeled by incorporating a fixed charge at the AlGaIn/GaN interface equal to σ_{int} and at the AlGaIn surface equal to σ_{PZ} to match experiment. The parameters used in the simulation are given in Table 4-1.

Simulation Results

The simulated dependence of E_{AlGaIn} versus V_G at the center of the gate is compared to the 1D model with experimentally determined parameters (Figure 4-8). In the simulation, σ_{int} was matched to the experimentally obtained value of 1.25×10^{-6} C/cm². The trend of the 2D simulated E_{AlGaIn} is similar to the 1D calculation. Above threshold, $|E_{AlGaIn}|$ increases until threshold with decreasing reverse gate bias. Below threshold, $|E_{AlGaIn}|$ tends to saturate. Although σ_{int} is matched, the saturation value of E_{AlGaIn} in the 2D simulation at the center of the gate is slightly lower than the experimentally determined curve. Since the simulated device has a finite gate width (1 μ m), it is important to analyze the edges of the gate for a comprehensive understanding of the E_{AlGaIn} versus V_G relationship.

Vertical cross-section plots of E_{AlGaIn} through the middle of the gate and drain edge of the gate are shown in Figure 4-9. The AlGaIn/GaN interface is referenced at $y = 0$ μ m and the AlGaIn surface is at $y = -0.018$ μ m. In the middle of the gate, E_{AlGaIn} remains essentially constant throughout the depth of the AlGaIn layer for $V_G = -2$ to -10 V. As shown in Figure 4-5, the magnitude of E_{AlGaIn} increases more above V_T than below V_T as a function of V_G , demonstrating the saturation of E_{AlGaIn} below V_T . However, at the gate edge, E_{AlGaIn} varies with depth in the AlGaIn barrier, and E_{AlGaIn} continues increasing with increasing reverse gate bias.

A horizontal cross section 1 nm below the gate contact in the AlGa_N barrier shows a large increase in E_{AlGaN} at the gate edges (Figure 4-10). At $V_G = 0$ V, $|E_{AlGaN}|$ is lower directly under the Schottky gate than under the passivation layer. This is a result of the negative polarization charge at the top surface of the AlGa_N. Under the nitride, the surface polarization exists, however, the gate has control of the potential under the gate electrode.

To explain the large increase in E_{AlGaN} at the gate edges, a plot of the potential at the GaN surface, 0.5 nm below the AlGa_N/GaN interface is shown (Figure 4-11). At large reverse gate biases, there is a large horizontal potential drop in the GaN surface near the gate edges. This potential drop results in a large horizontal electric field at the gate edge. The horizontal field at the gate edge is much larger than in the center of the gate (Figure 4-12). The contribution of the horizontal electric field at the gate edge adds to the vertical electric field increasing the magnitude of E_{AlGaN} increasing at the gate edges.

Summary

The relationship between E_{AlGaN} and V_G was calculated for an ideal 1D device. It was experimentally matched to the actual device, and a 2D simulation was performed. A 1D model was used to investigate the dependence of E_{AlGaN} with V_G . Adjusting σ_{int} and n_s based on experimental measurements provides an accurate relationship above threshold. The 1D model fails to capture the edge physics of a realistic device. 2D Sentaurus device simulation showed the 1D model is accurate above threshold, but below threshold, E_{AlGaN} at the gate edges continues increasing. Above threshold, $|E_{AlGaN}|$ increases linearly with increasing reverse gate bias and the field is approximately constant throughout the depth of the AlGa_N layer. Below threshold, $V_G <$

V_T , 2D effects change the field profile. In the middle of the gate, E_{AlGaN} saturates, but at the gate edges, E_{AlGaN} increases. With the relationship between E_{AlGaN} and V_G understood, this relationship can be used to explain the gate leakage transport mechanism in the AlGaN/GaN HEMT.

Table 4-1. List of parameters used in 1D E_{AlGaN} calculation

Parameter	Symbol	Value	Units
Temperature	T	300	K
Intrinsic carrier concentration	n_i	10^{-10}	cm^{-3}
AlGaN thickness	t_{AlGaN}	18	nm
Permittivity of GaN	ϵ_{GaN}	9.5	-
Permittivity of AlN	ϵ_{AlN}	8.5	-
Bandgap of GaN	$E_{G,\text{GaN}}$	3.4	eV
Bandgap of AlN	$E_{G,\text{AlN}}$	6.13	eV
Electron affinity of GaN	χ_{GaN}	4.1	eV
Ni work function	ϕ_m	5.27	eV
Mass of GaN	m_{GaN}^*	$0.2 \cdot m_0$	-
Mass of AlN	m_{AlN}^*	$0.48 \cdot m_0$	-
Fixed charge at AlGaN/GaN interface	σ_{int}	2.2×10^{-6}	C/cm^2

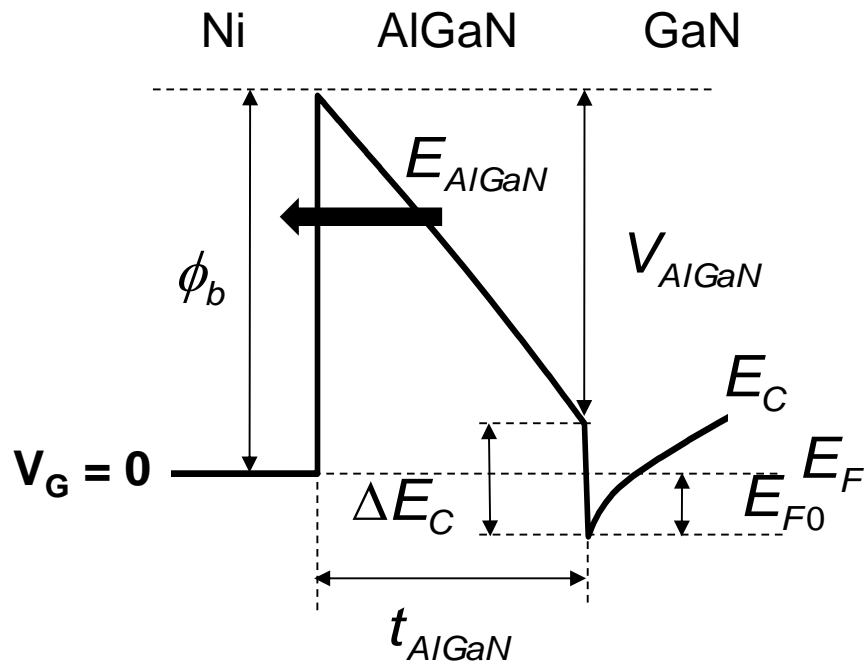


Figure 4-1. Energy band diagram schematic showing Ni/AlGaN/GaN interface

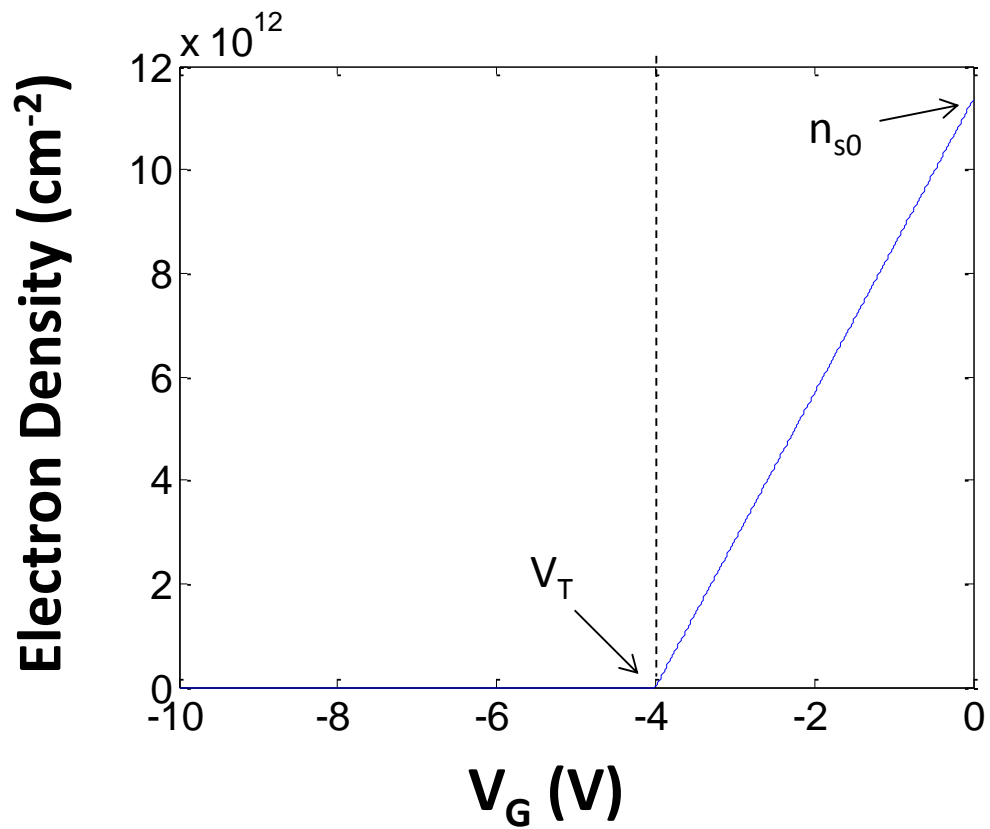


Figure 4-2. Dependence of the 2DEG density (n_s) with gate bias for the 1D case, with no interface trapped charge. Threshold is defined when n_s is entirely depleted ($n_s = 0$).

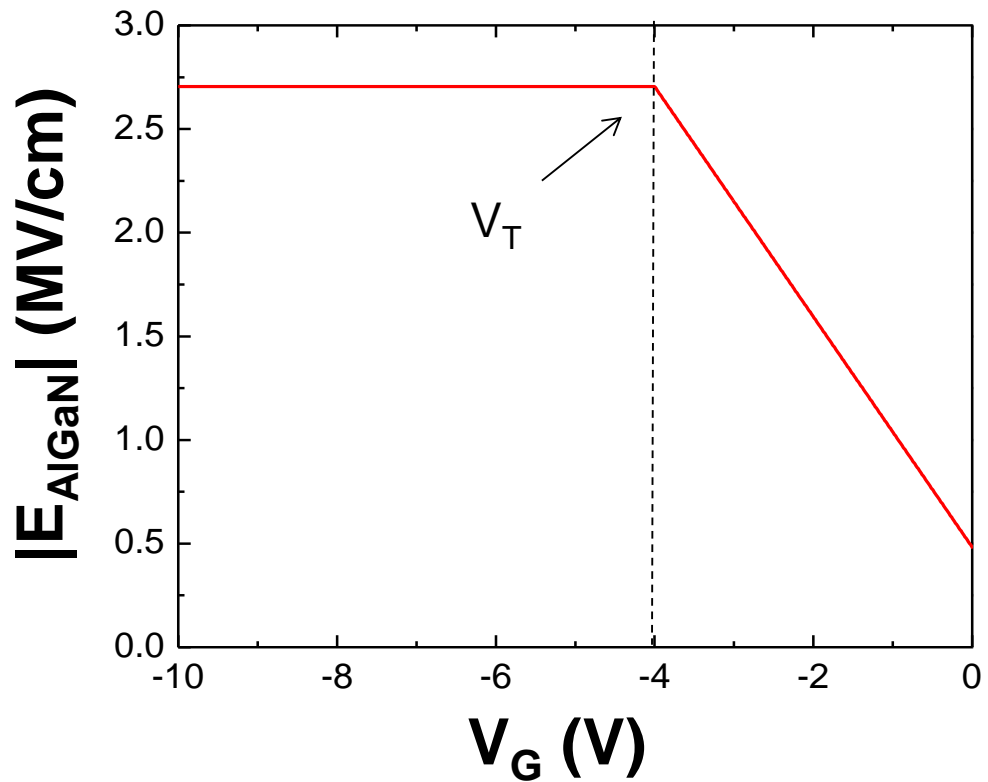


Figure 4-3. Idealistic 1D calculation of E_{AlGaIn} , assuming no interface trapped charge. E_{AlGaIn} increases linearly until the threshold voltage, then saturates.

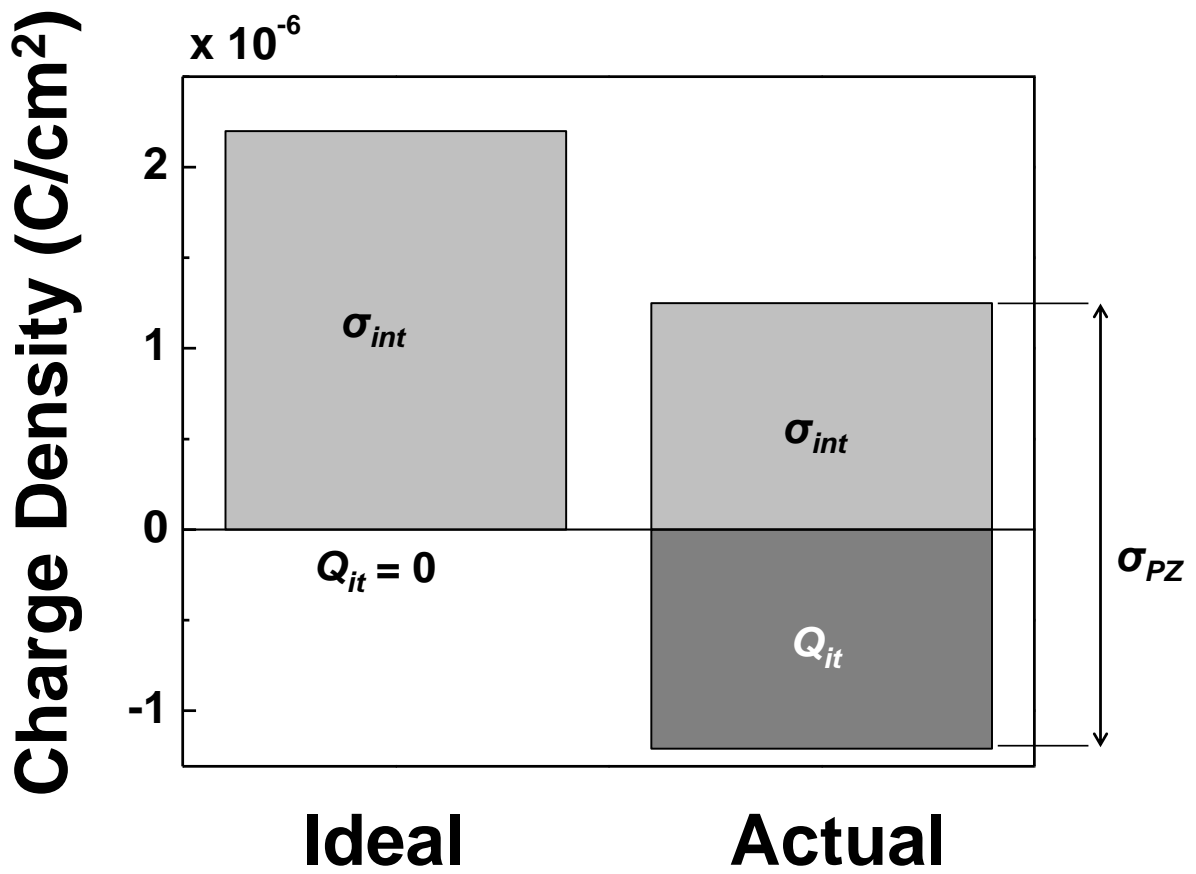


Figure 4-4. Bar diagram of the AlGaIn/GaN interface charge for an ideal device with no trapped charge and an actual device. Trapped charge reduces the positive fixed sheet charge density at the AlGaIn/GaN interface.

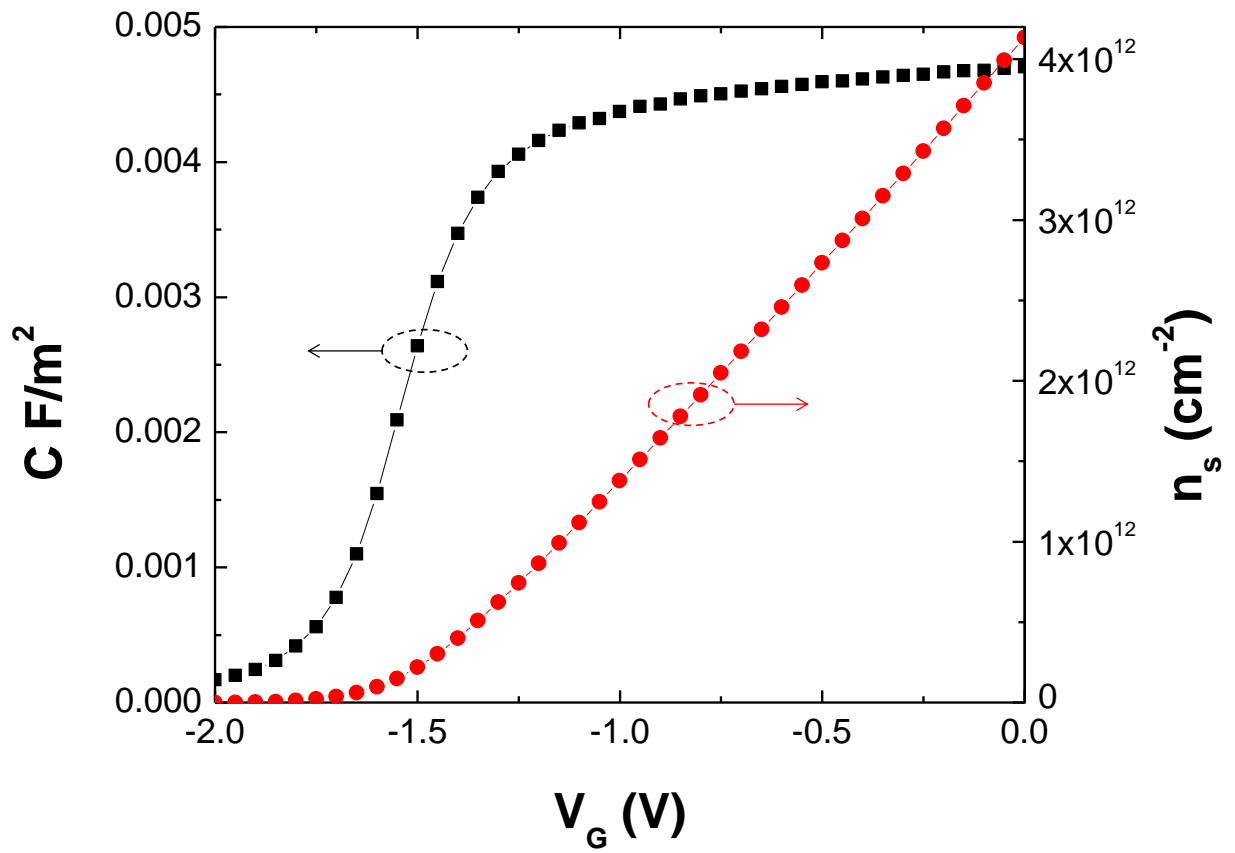


Figure 4-5. Capacitance-Voltage measurement, which is integrated in order to determine $n_s(V)$.

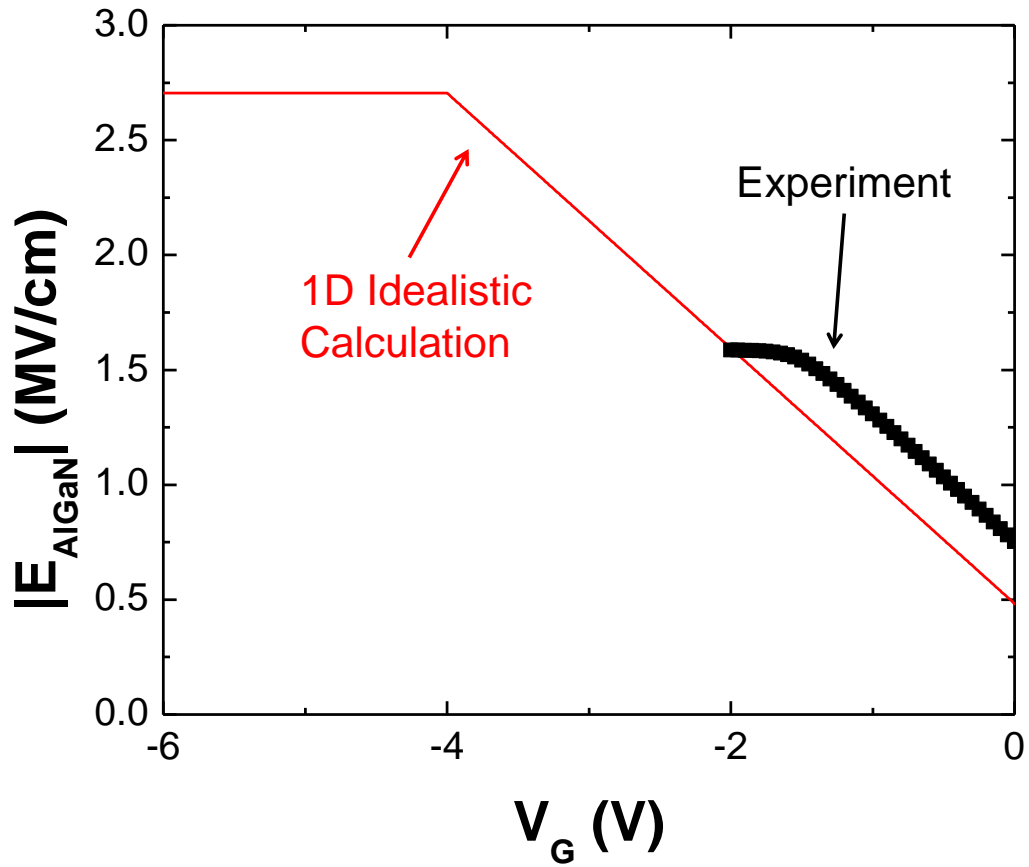


Figure 4-6. 1D ideal (no interface trapped charge) calculation and the experimental result from experimental parameters obtained by adjusting σ_{int} and obtaining n_s from C-V

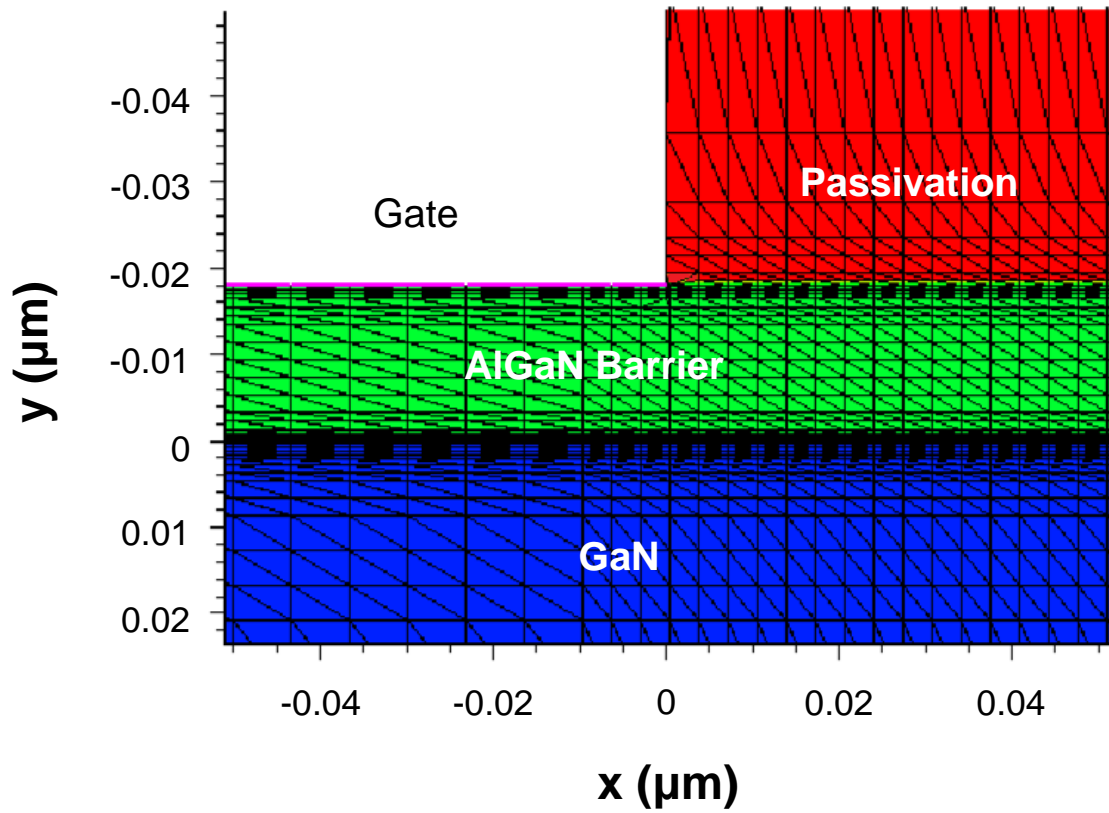


Figure 4-7. Optimized grid for Sentaurus simulation of the AlGaIn/GaN HEMT device.

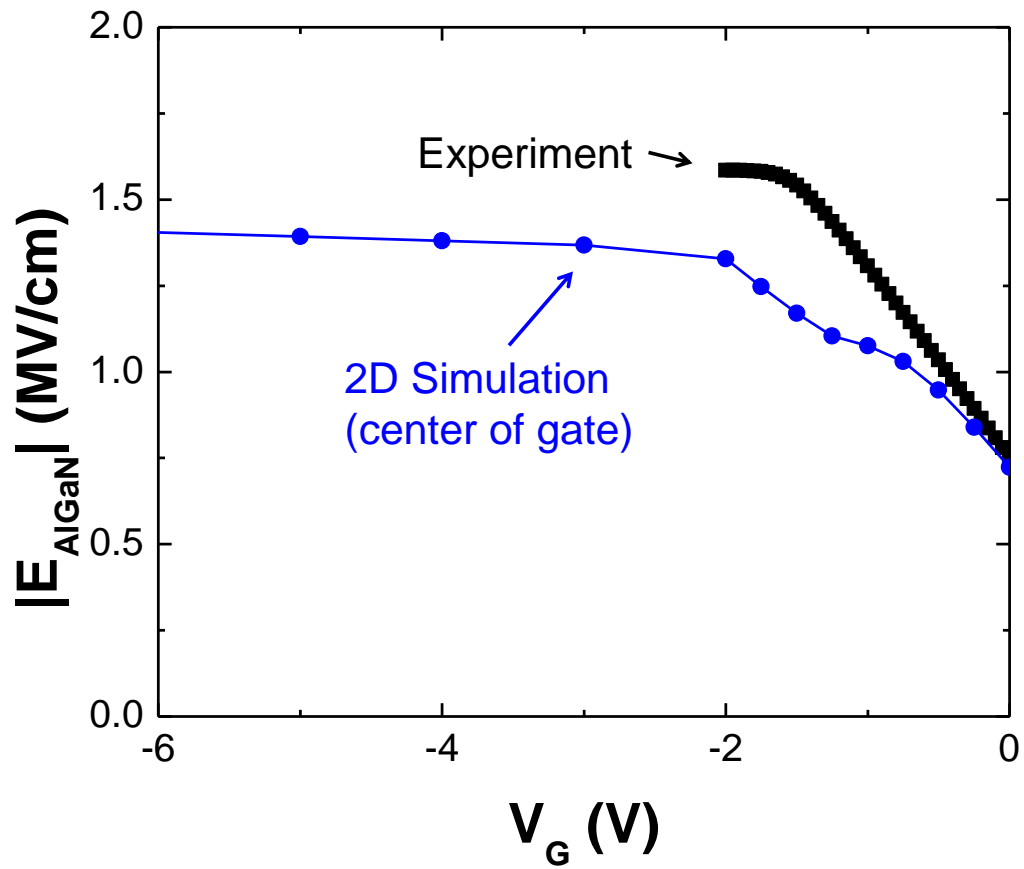


Figure 4-8. Experimental calculation of E_{AlGaIn} versus V_G compared to 2D simulation results.

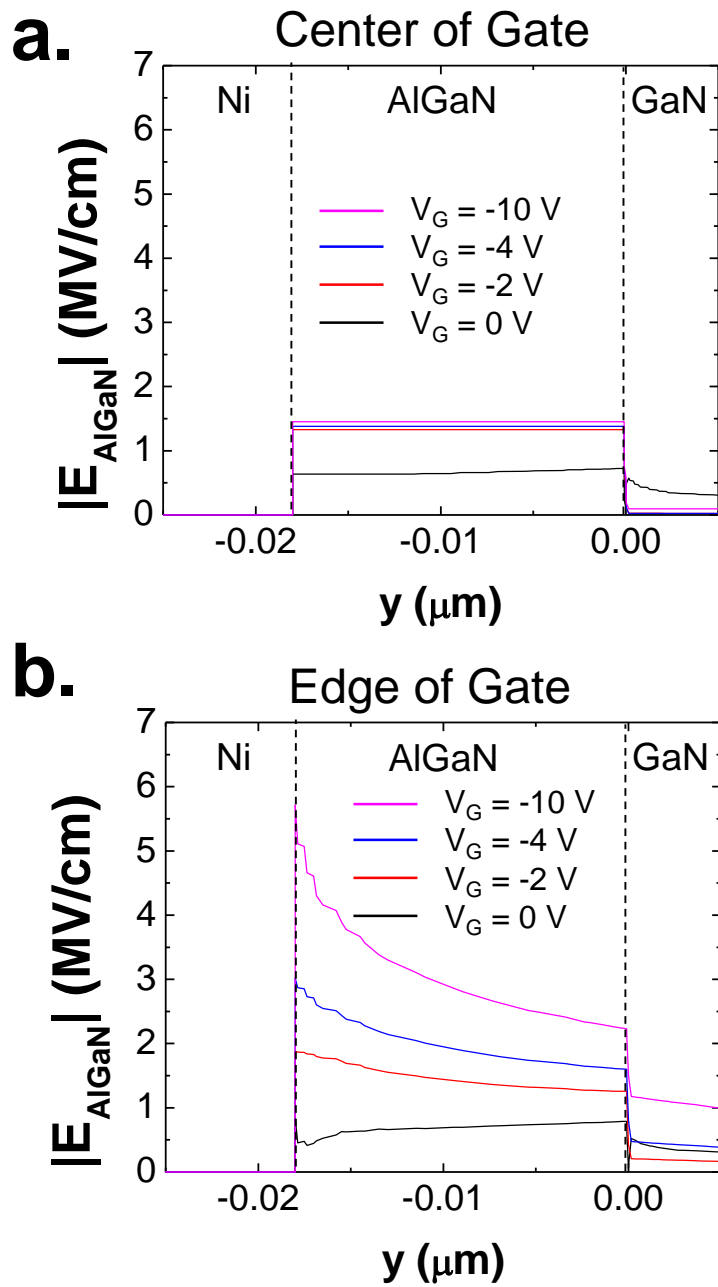


Figure 4-9. Vertical cross-section of electric field of the AlGaN/GaN HEMT at the (a) center of the gate and (b) drain edge of the gate.

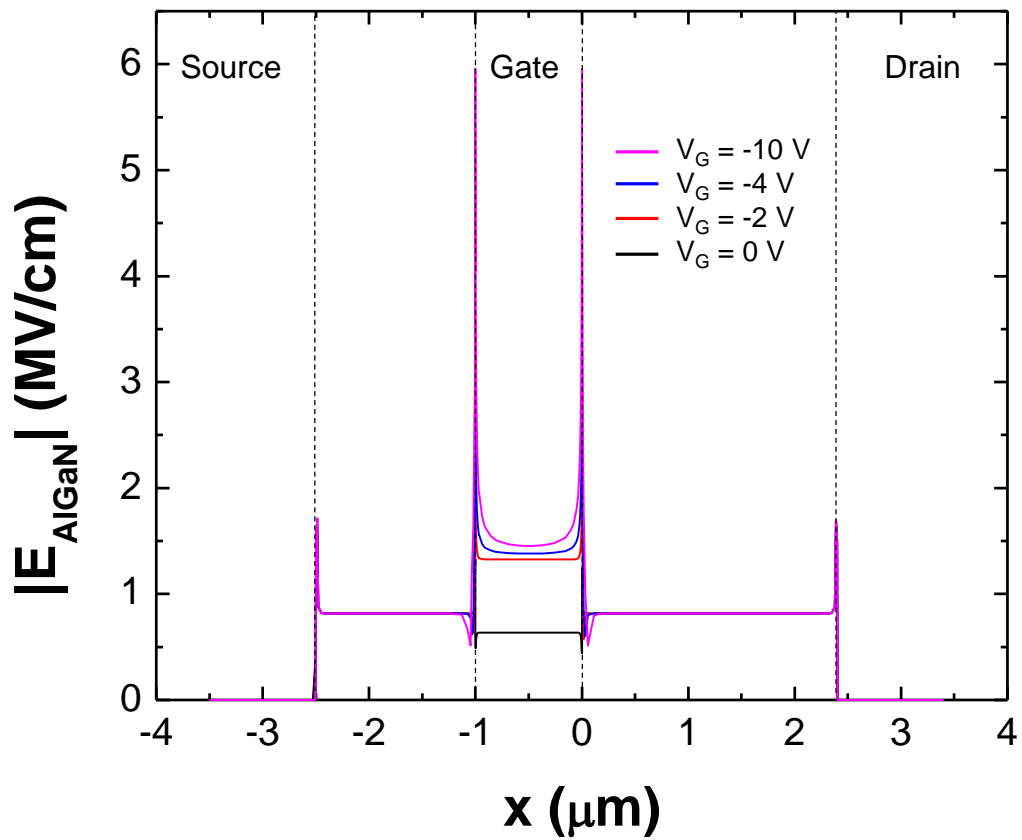


Figure 4-10. Horizontal cross-section of E_{AlGaN} taken near the top surface of the AlGaN barrier 1 nm below the gate contact.

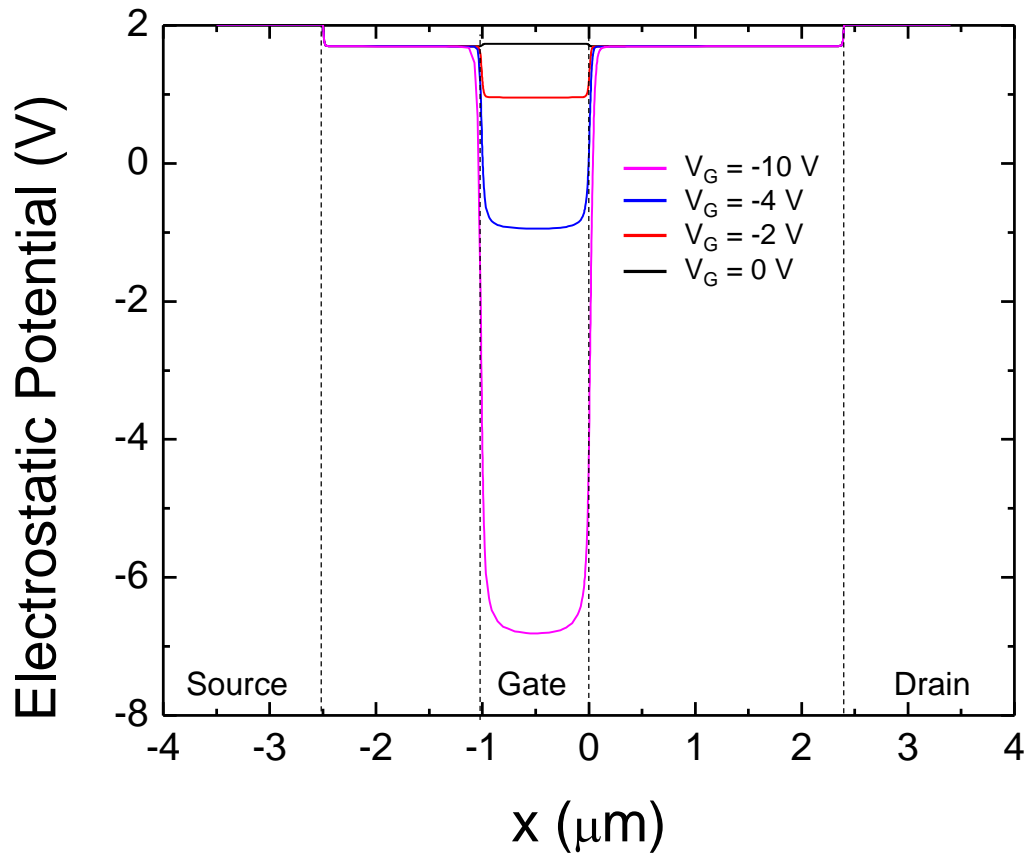


Figure 4-11. Horizontal cross-section of the electrostatic potential taken near the top surface of the GaN 0.5 nm below the AlGaIn/GaN interface.

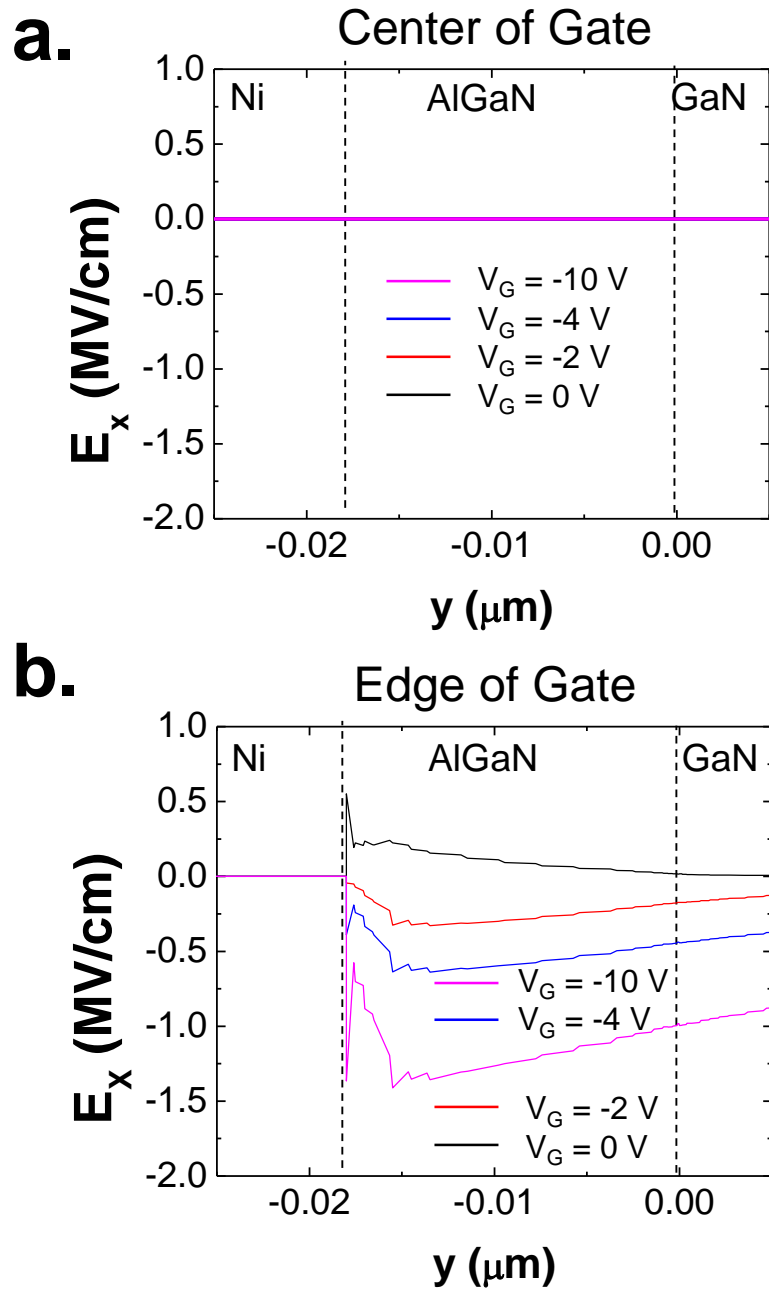


Figure 4-12. Horizontal component of E_{AlGaIn} at the (a) center and (b) edge of the gate.

CHAPTER 5
FIELD DEPENDENT MECHANICAL STRESS SENSITIVITY OF ALGaN/GaN HEMT
GATE LEAKAGE CURRENT

Introduction

AlGaN/GaN HEMTs provide benefits over Si, SiGe, SiC and GaAs material systems for high frequency and high power applications. Unique advantages include a built-in polarization and a wide bandgap which allow for high sheet charge carrier density and high voltage operation. However, the device reliability of AlGaN/GaN HEMTs still requires improvement. Particularly, generation of defects during high bias operation has been shown to increase the gate leakage current density (J_G), reducing the output power and power added efficiency (PAE), limiting its prolonged usefulness in high power applications [100]. A systematic study of gate leakage transport mechanisms in the presence of defects is required.

The physical breakdown of the AlGaN barrier has been shown to occur at voltages beyond the critical voltage (V_{crit}), creating an irreversible increase in J_G [11]. To demonstrate this crucial AlGaN/GaN HEMT failure mode, a step voltage stress is applied and the gate current is monitored. Figure 5-1 shows the results of V_G step electrical stress on J_G at the $V_{DS} = 0$ V state, showing a sudden increase in J_G at V_{crit} . This type of degradation has been hypothesized to be related to the generation of crystallographic defects via the inverse piezoelectric effect [11]. At large V_G , as seen from the Sentaurus 2D simulations in Chapter 4, increased vertical field occurs at the gate edges. This creates additional tensile stress in the AlGaN barrier through the inverse piezoelectric effect. This stress adds to the pre-existing built-in tensile stress resulting from lattice mismatch between the AlGaN barrier and the GaN layer. It has been suggested that when stress reaches the material critical limit, defect to form in

order to relax the internal elastic energy [11]. These defects cause a low resistance leakage path through the AlGa_N barrier resulting in a sudden increase in J_G . A mechanical wafer bending experiment in literature showed a reduction of V_{crit} with applied mechanical stress, however, only five pairs of devices were investigated in this study and a more comprehensive study is required [101].

Since stress is inherent in AlGa_N/Ga_N HEMTs, understanding the role of stress on J_G is essential to improve reliability. However, there are discrepancies in the published literature explaining the gate leakage mechanism of unstressed devices. Several transport mechanisms have been suggested to explain J_G such as trap-assisted tunneling [34], [78-81], direct or FN tunneling [78-80], [82], temperature assisted tunneling [78], [83], multi-step trap-assisted tunneling [84], thermionic trap assisted tunneling [82], [85-87], tunneling through a thin surface barrier [88], and PF emission [89-94]. We endeavor to resolve the mechanisms of gate leakage in AlGa_N/Ga_N HEMT by varying external mechanical stress and reverse gate bias simultaneously, and discuss implications on the effect of mechanical stress on device degradation.

Experiment

Wafer samples were attached to heat-treated high-carbon steel plates with epoxy and stressed in a four-point wafer bending setup. Compressive and tensile uniaxial stress up to 360 MPa was applied longitudinal to the channel direction. The stress dependence of the AlGa_N/Ga_N HEMT J_G was characterized at the $V_{DS} = 0$ state, isolating the effect of electric field induced by the gate. Various reverse biases (-0.1 V to -4 V) were applied to the gate and held constant until J_G reached steady-state to eliminate transient trapping effects before each measurement. At each bias, mechanical stress was incrementally applied then released, while simultaneously

measuring J_G . High-temperature measurements were taken on a temperature-controlled probe station using sample stage heaters.

Results and Discussion

Wafer Bending Results

Longitudinal stress, up to 360 MPa, was incrementally applied to the AlGaIn/GaN HEMT device while J_G was simultaneously measured over a period of 1800 seconds. Averaging J_G over 1800 seconds was done to account for random fluctuations in the measured current. It was found that a time duration of 1800 seconds while the stress was held constant was adequate to obtain a reasonable statistical confidence in the measured J_G . The normalized change in J_G due to applied stress ($\Delta J_G(\sigma)/J_G(0)$) was measured for several constant applied gate biases ($V_G = -0.1, -0.25, -0.5, -1, -2,$ and -4 V) using the above mentioned procedure. Figure 5-2 shows results of $\Delta J_G(\sigma)/J_G(0)$ for $V_G = -0.25$ V and -4 V. The stress dependence of J_G was weaker at $V_G = -4$ V than at $V_G = -0.25$ V. Tensile (compressive) stress increased (decreased) J_G for all applied gate biases. At each bias, after the compressive or tensile stress was applied to its maximum magnitude of 360 MPa, then the stress was incrementally released. Upon releasing the stress to zero, J_G returned to its initial, unstressed value. This demonstrates that the measured change in J_G is purely a reversible consequence of the applied stress, and not a transient effect. Also, it demonstrates that the applied mechanical stress (up to 360 MPa) does not induce permanent damage to the device.

To quantify the magnitude of the normalized change in gate current density, $\Delta J_G(\sigma)/J_G(0)$, for each applied gate bias and stress level, J_G is averaged over the duration of time the stress was held constant. Figure 5-3 shows $\Delta J_G(\sigma)/J_G(0)$ averaged for all levels of compressive and tensile stress at $V_G = -0.25$ V and -4 V. Error bars

representing the uncertainty in the measurement of $\Delta J_G(\sigma)/J_G(0)$ are three times the standard deviation of the J_G measurements over the duration when the stress was held constant.

The sensitivity of J_G to stress defined as the normalized change in J_G per stress, $[\Delta J_G(\sigma)/J_G(0)]/\sigma$, is calculated from the slope of the weighted total least squares linear fit of $\Delta J_G(\sigma)/J_G(0)$ versus stress, including uncertainty in J_G at each stress increment. The stress sensitivity of J_G is plotted as a function of reverse gate bias in Figure 5-4. Increasing the reverse gate bias is observed to decrease the sensitivity of J_G to stress. The sensitivity of J_G to stress decreased from $1.7 \pm 0.3 \%$ /100MPa at $V_G = -0.25$ V to $0.6 \pm 0.1 \%$ /100MPa at $V_G = -4$ V as shown in Figure 5-4. To interpret the decreasing sensitivity for increasing reverse gate bias, the dominant gate leakage transport mechanism needs to be analyzed.

Discussion

To understand the decreasing stress dependence of J_G with increasing reverse gate bias and compare the measurements to gate leakage transport models, the experimentally determined 1D E_{AlGaIn} values discussed in Chapter 4 are used. Since the 2D edge effects complicate the E_{AlGaIn} profile under the gate for gate biases below V_T , the simple 1D model cannot be used. Therefore, we analyze the gate leakage mechanism only for V_G above V_T . Simulations performed indicate that thermionic emission, bulk trap assisted tunneling, and Fowler-Nordheim (FN) tunneling models underestimate the magnitude of the experimental data [102]. However, the Poole-Frenkel (PF) emission model for gate leakage current closely matches the experimental data.

PF emission refers to the lowering of the Coulombic potential barrier of a trapped electron due to a large electric field, increasing the probability for the electron to be emitted into the conduction band. The general expression for PF emission current considering compensation is [103-105]:

$$J_{PF} = CE_{AlGaN} \exp \left[-\frac{qE_A - \beta \sqrt{E_{AlGaN}}}{rkT} \right], \quad (5-1)$$

where,

$$\beta = \sqrt{\frac{q^3}{\pi \epsilon_0 \epsilon_{AlGaN}}}, \quad (5-2)$$

C is a constant related to mobility and density of states, E_A is the trap activation energy, ϵ_0 is the vacuum permittivity, and ϵ_{AlGaN} is the relative permittivity of the AlGaN. The compensation, or slope parameter, r ranges from 1 to 2 depending on the amount of acceptor concentration and position of the Fermi energy with respect to E_A [103-105]. This compensation parameter is used as a first order model parameter to describe acceptor compensation. Often, the assumption of $r = 1$ is used to model PF emission data [93], [94]. When $r = 1$, the concentration of electrons excited up to the conduction band is small relative to the donor and acceptor densities. When $r = 2$, the concentration of acceptor levels is small compared to the number of donor levels and excited electrons. The E_A extracted from the PF model represents the average trap energy level with respect to the conduction band of the traps contributing to PF current. Traps are distributed both in energy and space throughout the AlGaN barrier; the extracted E_A only represents the traps participating in emitting electrons to the conduction band via the PF effect. Also, the trap levels are assumed to be located

physically close to the top surface of the AlGa_N layer, under the gate, therefore the traps are assumed to be filled, and only the emission is considered.

To determine the dominate gate leakage mechanism of the experimentally measured devices, the J_G versus V_G curves (Figure 5-5) were measured from 300 K to 400K. Since PF emission is a thermal assisted process whose efficiency increases at higher temperatures, the gate current was measured at temperatures larger room temperature. The temperature and field dependence of J_G were plotted in a PF plot (plot of the natural logarithm of the gate current divided by the electric field versus square root of the electric field) as shown in Figure 5-6. When plotted in this manner, the linear region of the PF plot signifies that PF emission dominates the gate leakage for that range of E_{AlGaN} .

By taking the natural log of Equation 5-1, the PF equation can be written as a linear equation, $y = m(T)x + b(T)$. The slope and y -intercept of the PF plot are $m(T)$ and $b(T)$ respectively.

$$\ln\left(\frac{J_{PF}}{E_{AlGaN}}\right) = \frac{1}{rkT} \beta \sqrt{E_{AlGaN}} - \frac{qE_A}{rkT} + \ln C \quad (5-3)$$

$$m(T) = \frac{\beta}{rkT} \quad (5-4)$$

$$b(T) = -\frac{qE_A}{rkT} + \ln C \quad (5-5)$$

To analyze the stress results systematically, the data is assumed to fit the PF model beginning with an assumption of the limiting case of high compensation, when $r = 1$ independent of stress. Then, a more physical fit to the PF model is used where r is determined by adjusting for a realistic value of the high frequency permittivity. Finally, a

reverse tunneling current is included into the overall expression to satisfy the equilibrium condition, $J_G(V_G = 0) = 0$.

Maximum compensation ($r = 1$)

We begin the analysis by assuming the simple case, where the maximum acceptor compensation level in the PF model is assumed ($r = 1$). The permittivity is extracted including the entire range of measured temperatures ($T = 300$ K to 400 K). First, the slope of the PF plot is plotted against $1/T$ (Figure 5-7). The slope of the linear fit to the plot in Figure 5-7 with the y -intercept forced to zero (m'), is

$$m' = \frac{q}{k} \sqrt{\frac{q}{\pi\epsilon_0\epsilon_{AlGaN}}}. \quad (5-6)$$

Then, the permittivity is calculated from

$$\epsilon_{AlGaN} = \frac{q^3}{m'^2 k^2 \pi \epsilon_0}, \quad (5-7)$$

giving a value of 5.88. Including the uncertainty in the measured J_G of 3.3% from a control measurement of 1200 simultaneous measurements, the uncertainty in the extracted value of ϵ_{AlGaN} is determined by including the error in the linear fit when calculating m' . The resulting uncertainty in ϵ_{AlGaN} is approximately ± 0.16 . So, for $r = 1$, $\epsilon_{AlGaN} = 5.88 \pm 0.16$.

Then, the trap activation energy is extracted using the y -intercept of the PF plot (Equation 5-5). First, the y -intercept of the PF plot is plotted against $1/T$ (Figure 5-8). The value of E_A is calculated from the slope (m''), and $\ln(C)$ is the y -intercept of the linear fit to the plot in Figure 5-8, where

$$m'' = \frac{-qE_A}{k}. \quad (5-9)$$

Hence,

$$E_A = \frac{-m''k}{q}. \quad (5-10)$$

E_A was determined to be 0.37 eV and $\ln(C) = -14.23$. The uncertainty in E_A and $\ln(C)$ is estimated by including the uncertainty of the linear fit when obtaining m'' . This gives an estimate for the error of ± 0.05 eV for E_A and ± 1.55 for $\ln(C)$.

The stress dependence of the PF current can be derived by first defining the unstressed PF current for $r = 1$ as:

$$J_{PF}(0) = CE_{AlGaN} \exp\left(\frac{-qE_A + \beta\sqrt{E_{AlGaN}}}{kT}\right). \quad (5-11)$$

In the PF expression, only E_A is assumed to be affected by mechanical stress. Stress has been known to change the trap activation energy level in Si/HfSiON devices dominated by PF tunneling through altering bond angle and lengths [106][107]. Although the nature of the trap is likely different in the AlGaN/GaN system than Si/HfSiON, similar physics will apply where stress changes the bond lengths and angles, which will in turn affect the trap activation energy. The compensation parameter, permittivity, and other parameters are assumed to remain independent of stress. During four-point bending, equal stress is applied to both the AlGaN and GaN layer since the AlGaN/GaN interface is located close to the top surface of the wafer, far from the neutral axis of bending. Therefore, E_{AlGaN} will not be affected by the externally applied stress. Under these assumptions, the PF current under stress is given by

$$J_{PF}(\sigma) = CE_{AlGaN} \exp\left(-\frac{qE_A + \Delta E_A(\sigma) - \beta\sqrt{E_{AlGaN}}}{kT}\right) = J_{PF}(0) \exp\left(\frac{\Delta E_A(\sigma)}{kT}\right), \quad (5-12)$$

where $\Delta E_A(\sigma)$ is the change in trap energy level due to the applied mechanical stress. The normalized change in PF current with stress is:

$$\frac{\Delta J_{PF}(\sigma)}{J_{PF}(0)} = \frac{J_{PF}(\sigma) - J_{PF}(0)}{J_{PF}(0)} = \exp\left(\frac{\Delta E_A(\sigma)}{kT}\right) - 1. \quad (5-13)$$

Based on Equation 5-13, the expected normalized change in PF current for a given amount of stress is constant independent of E_{AlGaN} or V_G . However, the experimentally measured $[\Delta J_G(\sigma)/J_G(0)]/\sigma$ from wafer bending experiments decreases with increasing reverse gate bias. Therefore, the simplistic model ($r = 1$ independent of stress) fails to capture the correct trend observed experimentally.

Reduced compensation ($1 < r < 2$)

The permittivity used in the PF model should be the high frequency permittivity [103]. This is because the trapping/detrapping effects are quick transients. The high frequency permittivity of AlGaN is $\epsilon_{AlGaN} = 5.1 \pm 0.5$, based on the high frequency permittivities of AlN (4.6) and GaN (5.3) [108]. However, the value of permittivity extracted from the PF model assuming the high compensation case with $r = 1$ was 5.88 ± 0.16 . Since the extracted permittivity based on the assumption that $r = 1$ does not match the required high permittivity value, the compensation factor r is adjusted. From Equation 5-4 using $\epsilon_{AlGaN} = 5.1$, the value $r = 1.07 \pm 0.02$ is extracted in order to provide a more physical fit to the PF model. This value of r still signifies very high compensation. Since the r value is adjusted to match the high frequency permittivity of AlGaN, the E_A value is also adjusted. Based on Equation 5-5 including $r = 1.07 \pm 0.02$, the value of E_A becomes 0.40 ± 0.05 eV and $\ln(C)$ is -13.55 ± 1.55 .

Since r is no longer fixed at the limit of maximum compensation, when E_A changes with stress, r also will change with stress. Figure 5-9 shows a schematic of the trap

level change with stress, and how compensation affects PF emission. When E_A increases (compressive stress), the trap energy level moves farther away from the conduction band. The acceptor compensation increases while the probability of emission into the conduction band decreases. In the case of decreasing E_A (tensile stress), the opposite is true. Including the change in E_A and change in r with stress (Δr) the PF current under stress is written as

$$J_{PF}(\sigma) = CE_{AlGaN} \exp\left(\frac{-qE_A + \Delta E_A(\sigma) - \beta\sqrt{E_{AlGaN}}}{(r + \Delta r)kT}\right). \quad (5-14)$$

The normalized change in J_{PF} with stress is

$$\frac{\Delta J_{PF}(\sigma)}{J_{PF}(0)} = \exp\left(\frac{r(\Delta E_A(\sigma)) + E_A(\Delta r) - \beta(\Delta r)\sqrt{E_{AlGaN}}}{r(r + \Delta r)kT}\right) - 1. \quad (5-15)$$

Both ΔE_A and Δr are obtained by simultaneously solving for $\Delta J_{PF}(\sigma)/J_{PF}(0)$ at two biases (-0.5 and -1 V). These bias points were chosen because the gate leakage mechanism is primarily PF emission in this range. Incorporating uncertainties from E_A and r gives $\Delta E_A = -0.26 \pm 0.07$ meV/100 MPa and $\Delta r = 0.0017 \pm 0.0001$ /100 MPa.

Tensile stress decreases E_A and compressive stress increases E_A .

This result is unlike the Si/HfSiON system, where both tensile and compressive stress decreased the trap energy level, increasing J_G [106][107]. In the Si/HfSiON device, the dielectric is unstressed. Both compressive and tensile stress perturbs the bond angles and bond lengths from equilibrium, reducing E_A . In the AlGaIn/GaN HEMT, the AlGaIn layer already has a large amount of tensile stress from lattice mismatch. Therefore, applied tensile stress will continue perturbing the bond angles and lengths decreasing E_A , and compressive stress will tend to return the bond angles and lengths back to equilibrium increasing E_A .

Figure 5-10 shows the simulated $\Delta J_{PF}(\sigma)/J_{PF}(0)$ per 100 MPa calculated from Equation 5-15 compared to experiment. Although we use E_{AlGaN} in simulation, for the purpose of plotting, the V_G values are used to compare to experiment. Considering r changing with stress provides a reasonable fit to experiment within the range of experimental uncertainty. The V_G range shown is from 0 to -2 V, since the experimentally obtained 1D E_{AlGaN} values are only valid until $\sim V_T$. It can be observed that there is some small discrepancy in the fit at low V_G . We investigate the effect of reverse current in the following discussion.

Reduced compensation ($1 < r < 2$) with reverse current

At equilibrium, polarization creates a relatively large E_{AlGaN} (0.75 MV/cm). This field should produce a significant forward PF current. However, at $V_G = 0$ V, the net current must be zero. Therefore, to balance the PF current, a reverse current (J_R) of equal and opposite magnitude should be present to balance the PF current at equilibrium. The exact transport mechanism of the reverse current is not well understood at this time, however Yan, et al. proposed that in equilibrium $J_{R0} \propto \exp(\alpha\epsilon^{3/2}/E_{AlGaN})$ where α is a constant [94]. Figure 5-11 shows a schematic diagram showing J_{PF} and J_R , assuming J_R is assisted by bulk traps. In the PF plot (Figure 5-6), the experimentally measured J_G differs from the ideal linear fit. The difference between the ideal linear extrapolated PF plot and the measured data is assumed to be the reverse current. Figure 5-12 shows the ideal PF (J_{PF}) current, reverse current (J_R), and the total measured gate current (J_G), where

$$J_G = J_{PF} - J_R \quad (5-16)$$

The derived expression in Equation 5-15 describes the normalized change in PF current only, neglecting the reverse current. Therefore, to incorporate the reverse current in the normalized change in the total gate current, the expression for normalized change in PF current is written as:

$$\frac{\Delta J_{PF}(\sigma)}{J_{PF}(0)} = \frac{\Delta J_G(\sigma) + \Delta J_R(\sigma)}{J_G(0) + J_R(0)}. \quad (5-17)$$

Solving for $\Delta J_G(\sigma)/J_G(0)$ based on Equation 5-15 for $\Delta J_{PF}(\sigma)/J_{PF}(0)$ gives

$$\frac{\Delta J_G(\sigma)}{J_G(0)} = \left[\exp\left(\frac{r(\Delta E_A) + E_A(\Delta r) - \beta(\Delta r)\sqrt{E_{AlGaN}}}{r(r + \Delta r)kT}\right) - 1 \right] \frac{J_G(0) + J_R(0)}{J_G(0)} - \frac{\Delta J_R(\sigma)}{J_G(0)}. \quad (5-18)$$

Excluding the last term, $\Delta J_R(\sigma)/J_G(0)$, this expression is straight forward to calculate. Since the exact mechanism of J_R is not well characterized, interpreting the stress dependence of J_R is also not clear. However, making some simple assumptions about $\Delta J_R(\sigma)/J_G(0)$ can provide a better fit to the experimental stress results. Figure 5-13 shows the experimental fit including reverse current for two situations. First, the $\Delta J_R(\sigma)/J_G(0)$ is neglected, but the calculation over estimates $\Delta J_G(\sigma)/J_G(0)$ at low V_G . Then, $\Delta J_R(\sigma)/J_G(0)$ is set to 1.5% to achieve a very good fit to the experimental data. It is likely that J_R may depend slightly with stress, in particular at very low V_G . However, more measurements at lower reverse gate biases will be needed to make a definitive conclusion. The inclusion or omission of $\Delta J_R(\sigma)/J_G(0)$ only affects the fit at low V_G . Once E_{AlGaN} increases enough to cause $J_{PF} \gg J_R$, the first part of Equation 5-18 captures the physics of carrier transport.

At voltages below threshold, E_{AlGaN} at the gate edges continues to increase. Also, the thickness of the AlGaN potential barrier reduces as shown in Figure 5-14. This results in the probability of FN tunneling increasing. Around 3 MV/cm, the FN tunneling current becomes significant [102]. The FN tunneling will occur at the gate edges, where E_{AlGaN} is the largest, in parallel with the PF tunneling in the middle of the gate. At extremely large E_{AlGaN} values where degradation occurs, the majority of J_G will likely be dominated by FN tunneling. The stress dependence of FN tunneling will be dominated by the out-of-plane effective mass, which is relatively independent of stress [72]. Hence, stress will not cause an incremental change in J_G , but can cause defect formation.

Summary

We have developed a model to explain the gate leakage mechanism in an AlGaN/GaN HEMT. This model explains the experimentally observed decreasing stress dependence of J_G with increasing reverse gate bias at a given stress. Tensile (compressive) stress increases (decreases) J_G for all applied gate biases ($V_G = -0.1$ to -4 V). We conclude, based on our model, that both PF and a reverse current mechanism are present for $V_G > V_T$. Table 5-1 summarizes the key parameters extracted to match the experimentally measured data. Below V_T , E_{AlGaN} at the gate edges increases due to 2D edge effects. FN tunneling current likely dominates for very large reverse V_G , where $E_{AlGaN} > 3$ MV/cm. At the critical voltage, J_G is dominated by FN tunneling at the edges of the gate, which will have negligible incremental stress dependence, but defect formation can occur.

Table 5-1. Key parameters extracted to match experimental data

Parameter	Maximum Compensation	Reduced Compensation
r	1	1.07 ± 0.04
Δr	-	$0.0017 \pm 0.0001 / 100 \text{ MPa}$
E_A	$0.37 \pm 0.05 \text{ eV}$	$0.4 \pm 0.05 \text{ eV}$
ΔE_A	-	$-0.26 \pm 0.07 \text{ meV}/100 \text{ MPa}$
ϵ_{AlGaN}	5.88 ± 0.16	5.10
$\ln(C)$	-14.23 ± 1.55	-13.56 ± 1.55

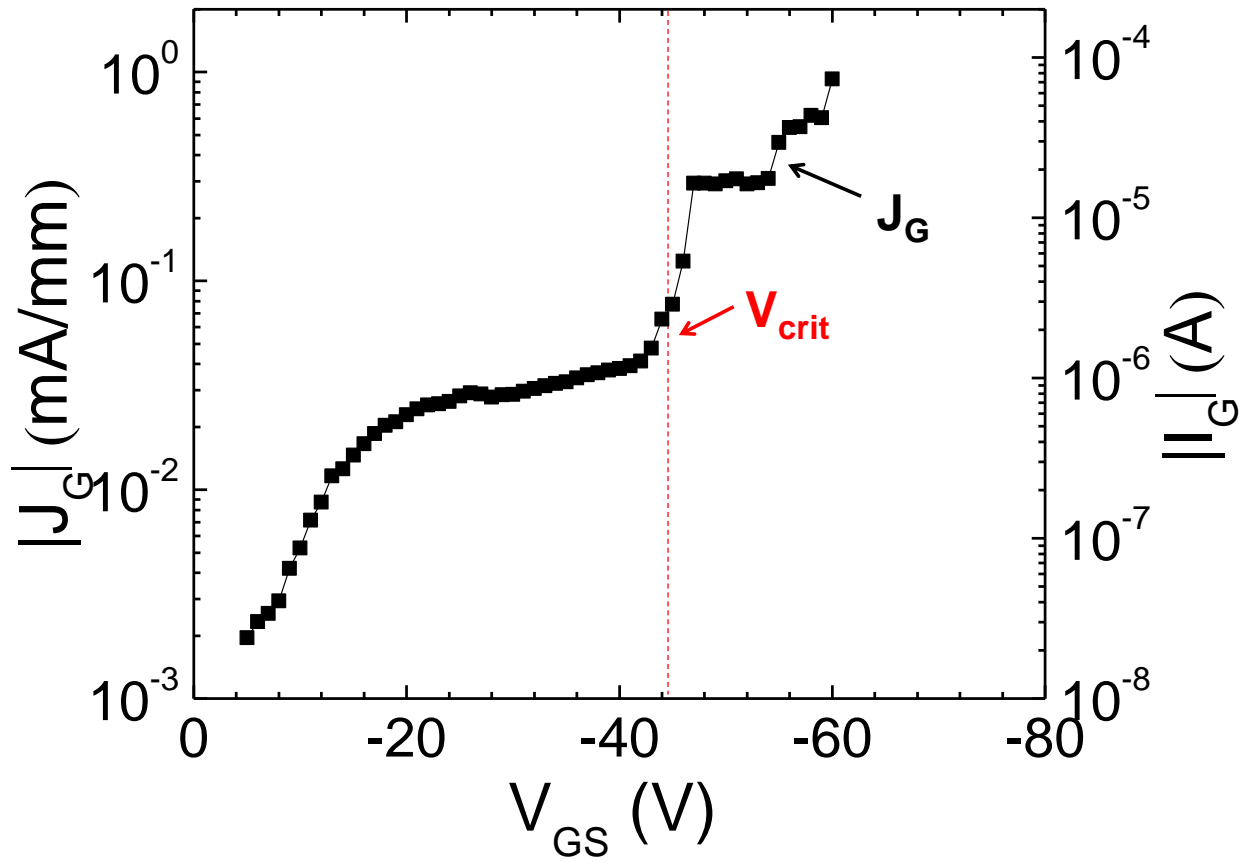


Figure 5-1. Electrical step stress measurement showing the breakdown of J_G at the critical voltage.

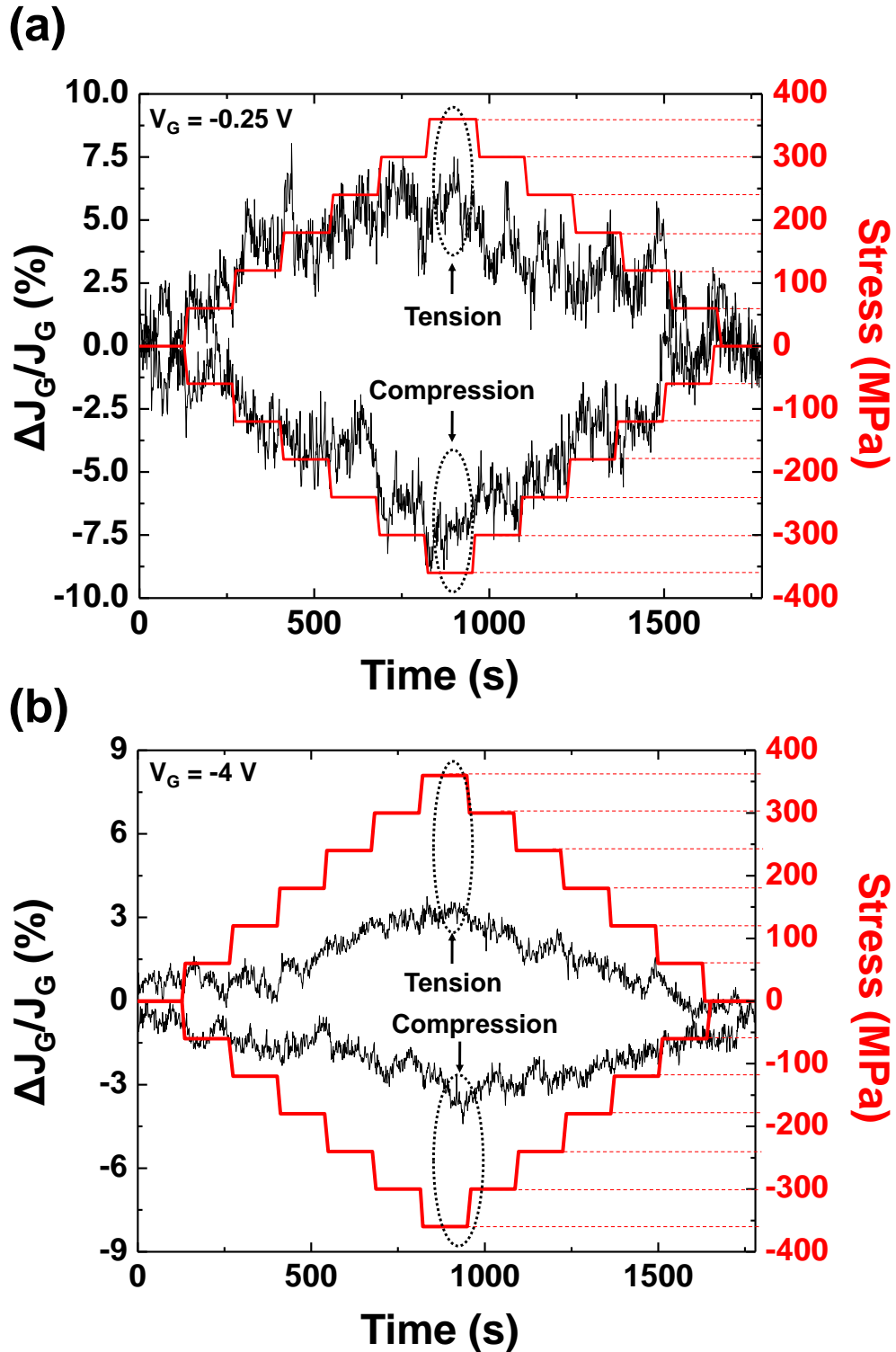
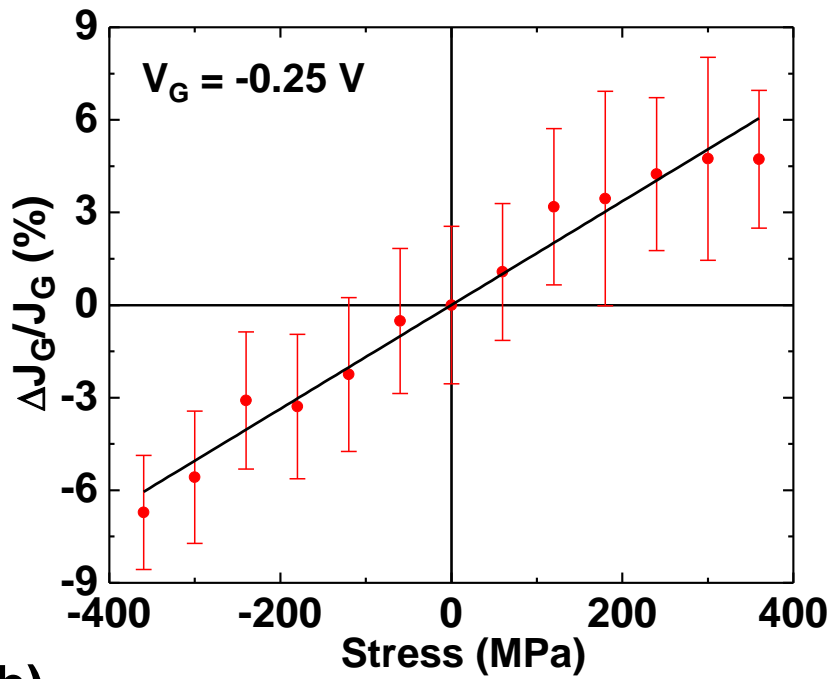


Figure 5-2. Normalized change in J_G for incrementally increasing and decreasing uniaxial stress for (a) $V_G = -0.25 \text{ V}$ and (b) $V_G = -4 \text{ V}$.

(a)



(b)

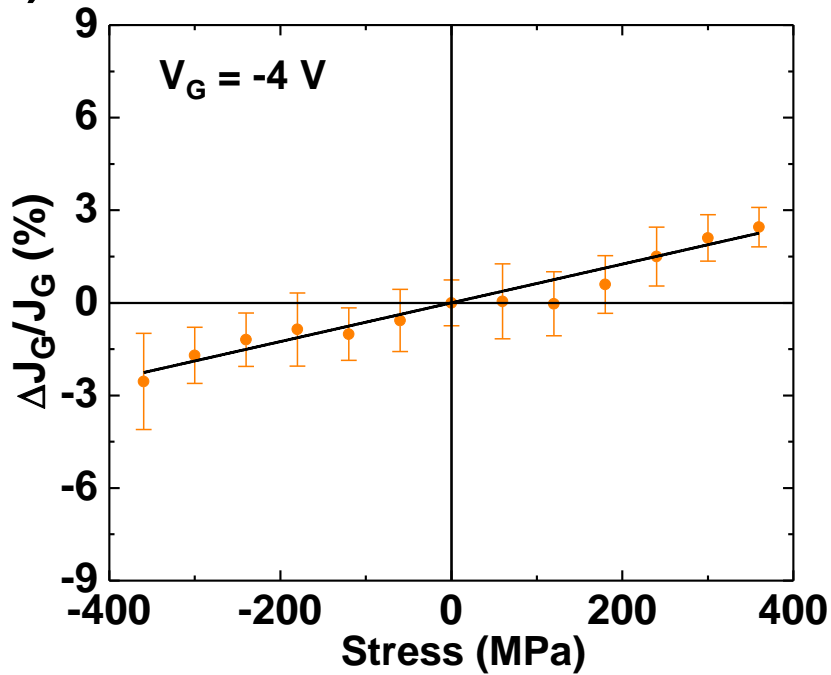


Figure 5-3. $\Delta J_G(\sigma)/J_G(0)$ averaged for all levels of compressive and tensile stress at $V_G = -0.25$ V and -4 V. Uncertainty comes from three standard deviation from the measurement of $\Delta J_G(\sigma)/J_G(0)$ over the duration stress was held constant.

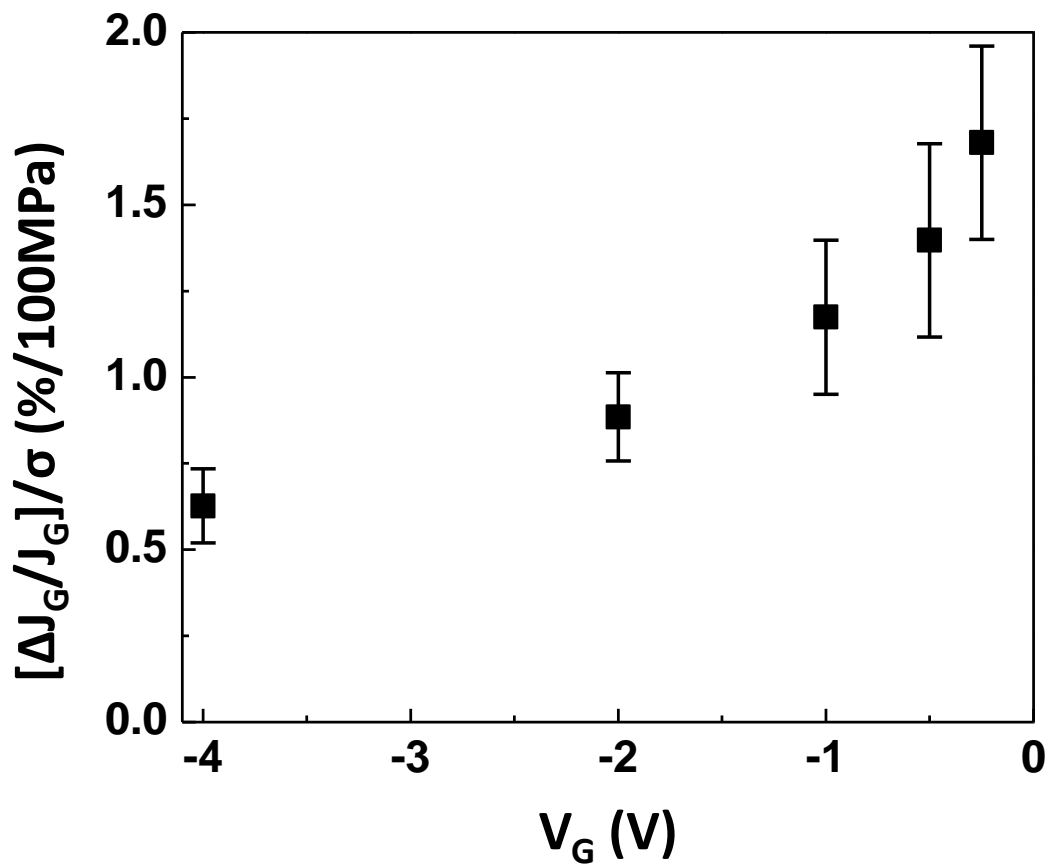


Figure 5-4. Experimentally measured stress sensitivity of J_G per 100 MPa of stress, as a function of reverse gate bias.

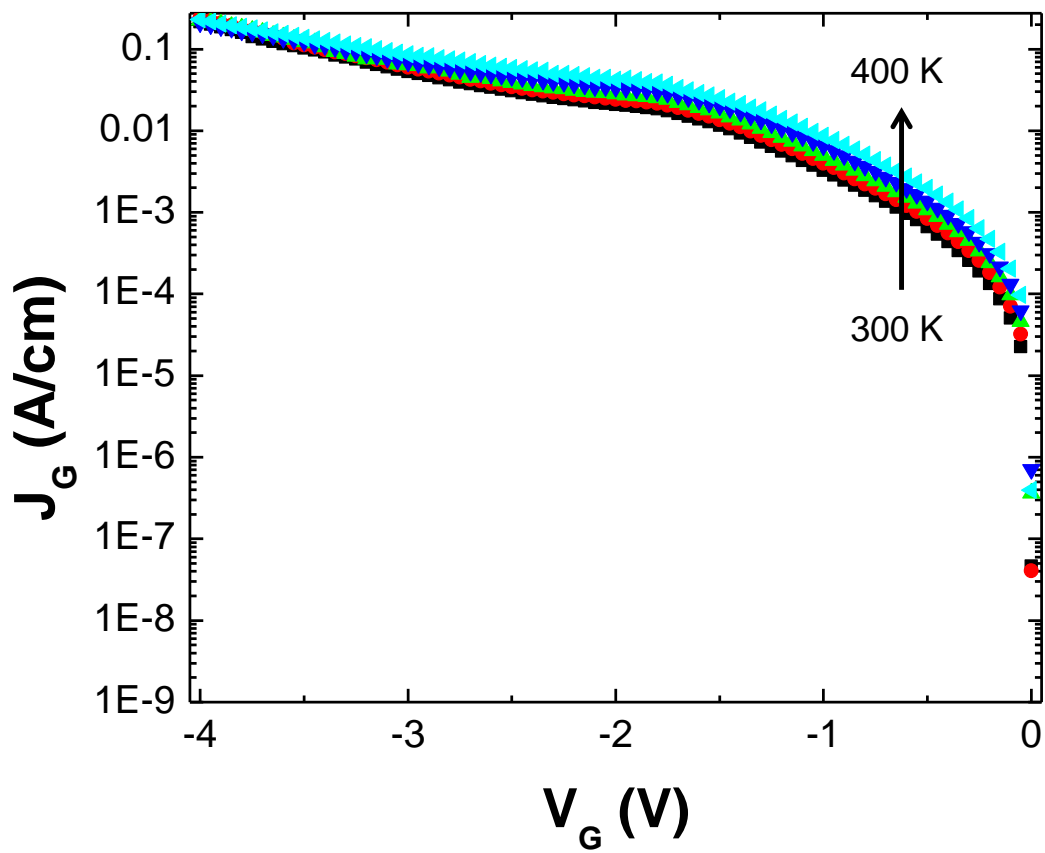


Figure 5-5. Measured gate leakage current density versus gate voltage from $T = 300$ K to 400 K for unstressed AlGaN/GaN HEMT.

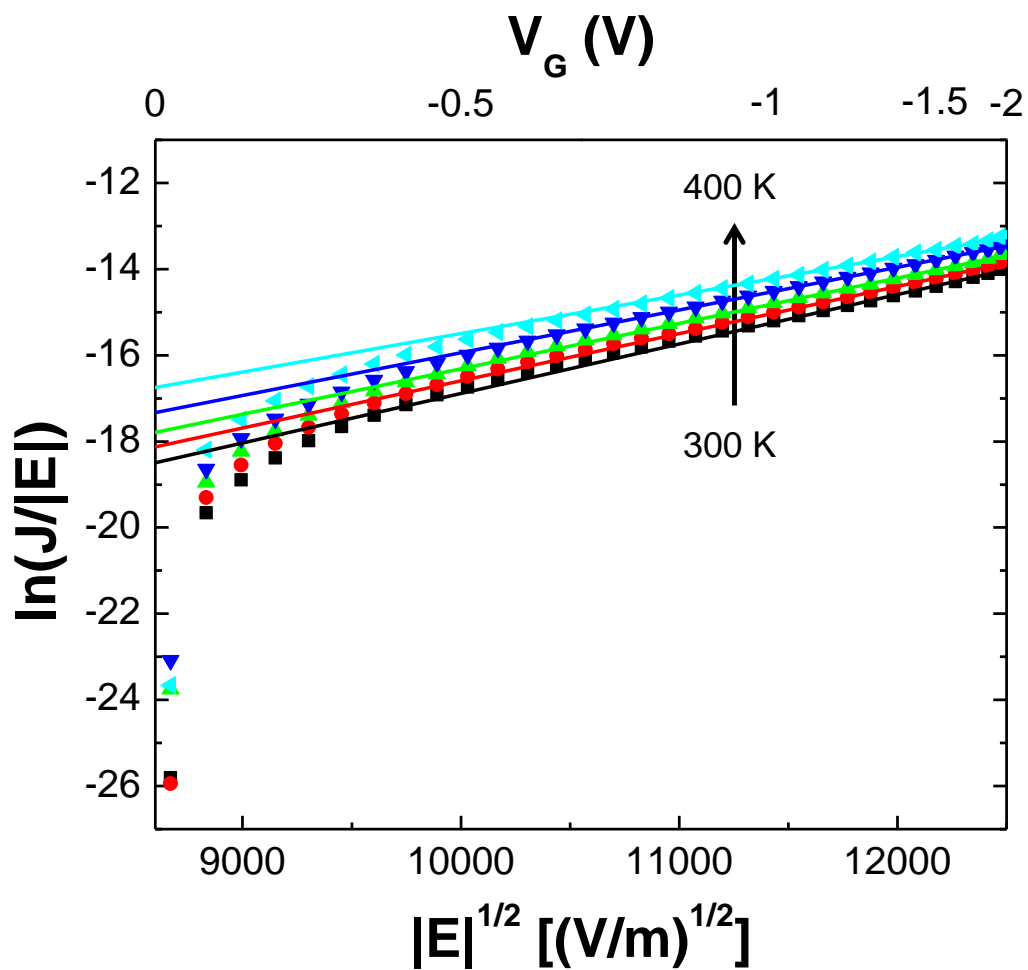


Figure 5-6. PF plot showing linear fit to the measured data for $T = 300$ K to 400 K.

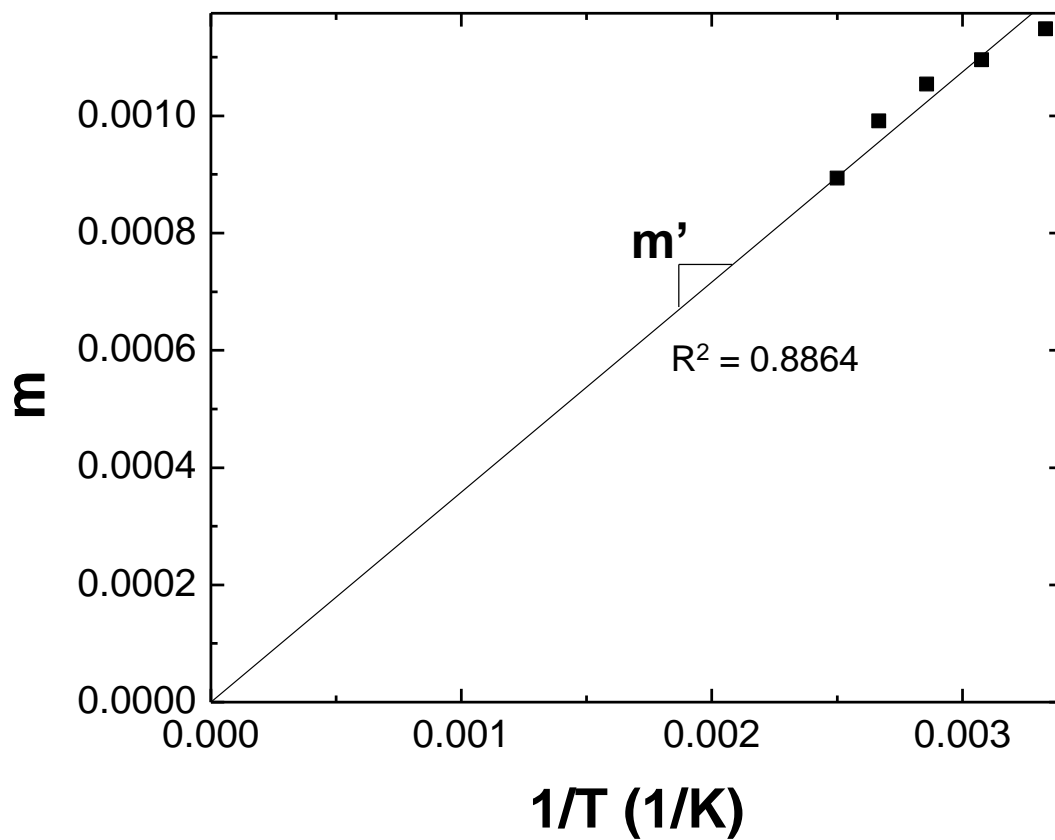


Figure 5-7. The slope of the PF plot (m) plotted versus $1/T$. The slope of this plot (m') is used to calculate ϵ_{AlGaN} .

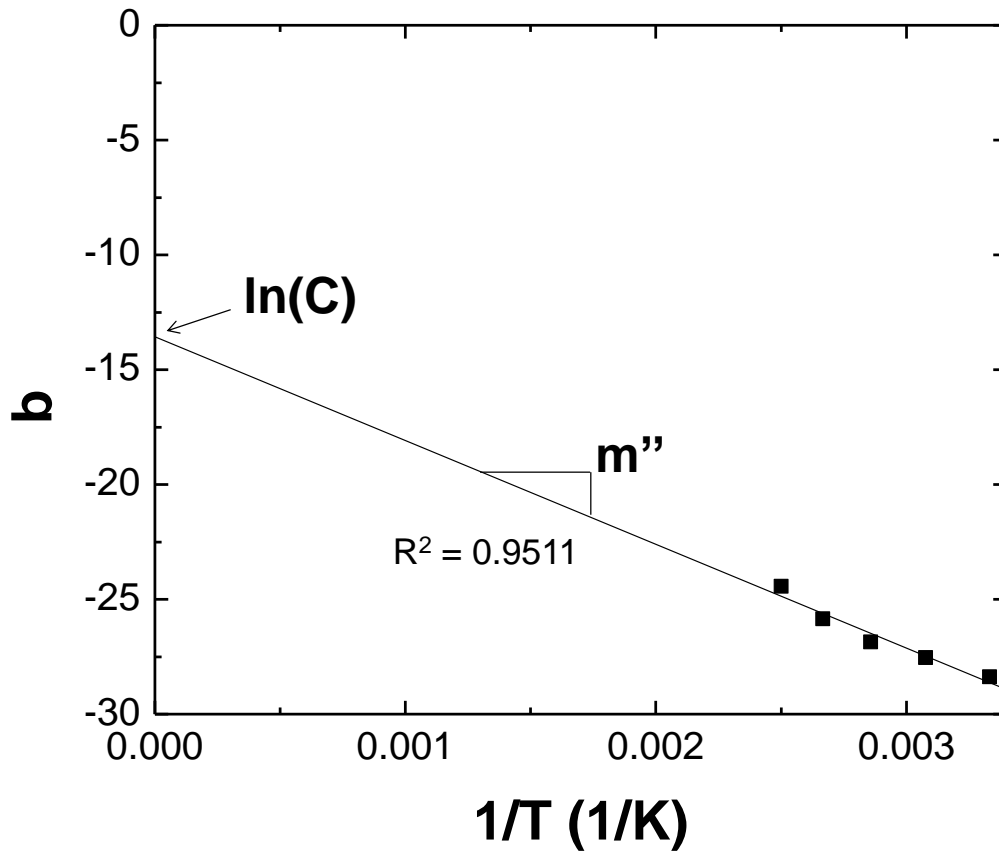
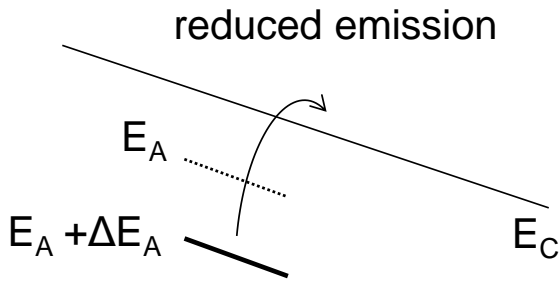


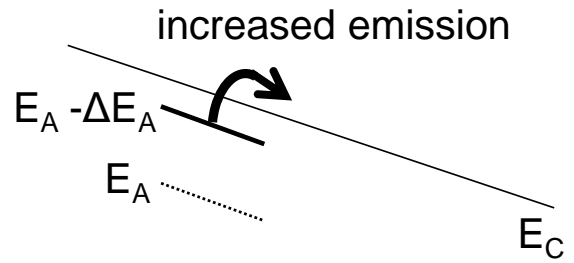
Figure 5-8. The y-intercept of the PF plot versus $1/T$. The slope of this plot (m'') is used to calculate the trap energy level.

Compression



increased compensation
(r decreases)

Tension



reduced compensation
(r increases)

Figure 5-9. Schematic of change in E_A with compressive and tensile stress. Compressive stress increases E_A , decreasing r , increasing compensation, and reducing PF emission. The opposite is true for tensile stress.

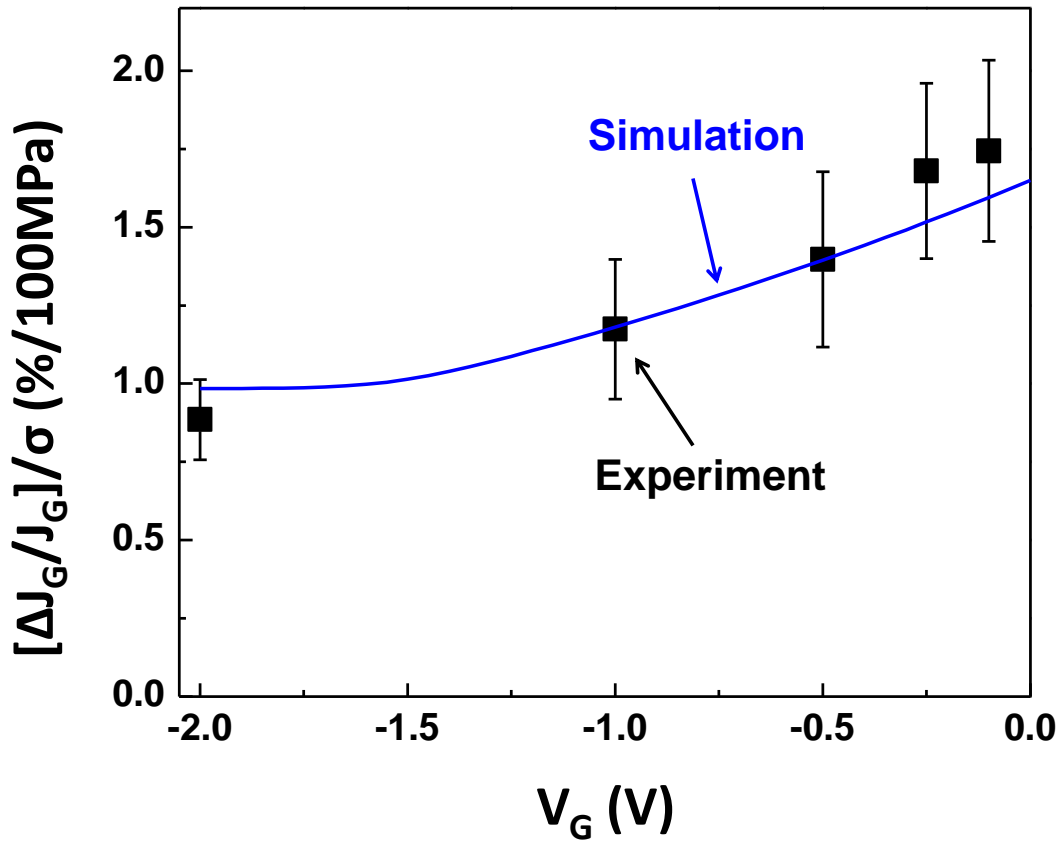


Figure 5-10. Simulated stress sensitivity of J_G per 100 MPa of stress, including E_A and r changing with stress, as a function of reverse gate bias.

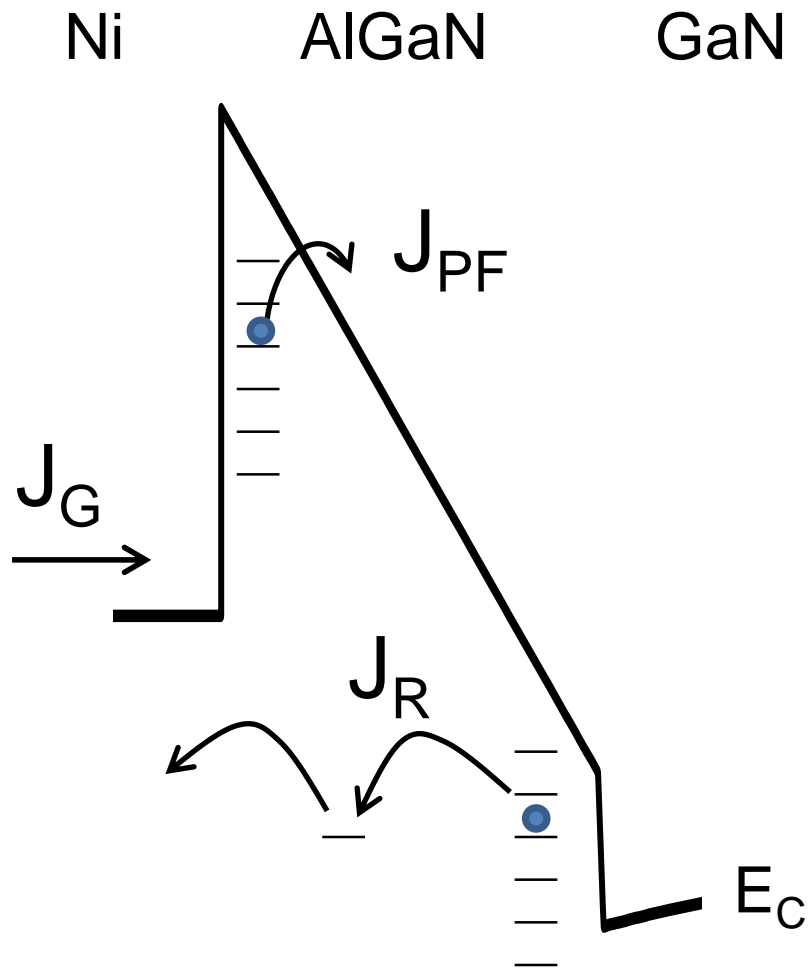


Figure 5-11. Schematic of J_G , J_{PF} , and J_R assuming J_R is a bulk-assisted mechanism driven by the PF emission current for $V_G = -2$ V and other parameters from Table 4-1.

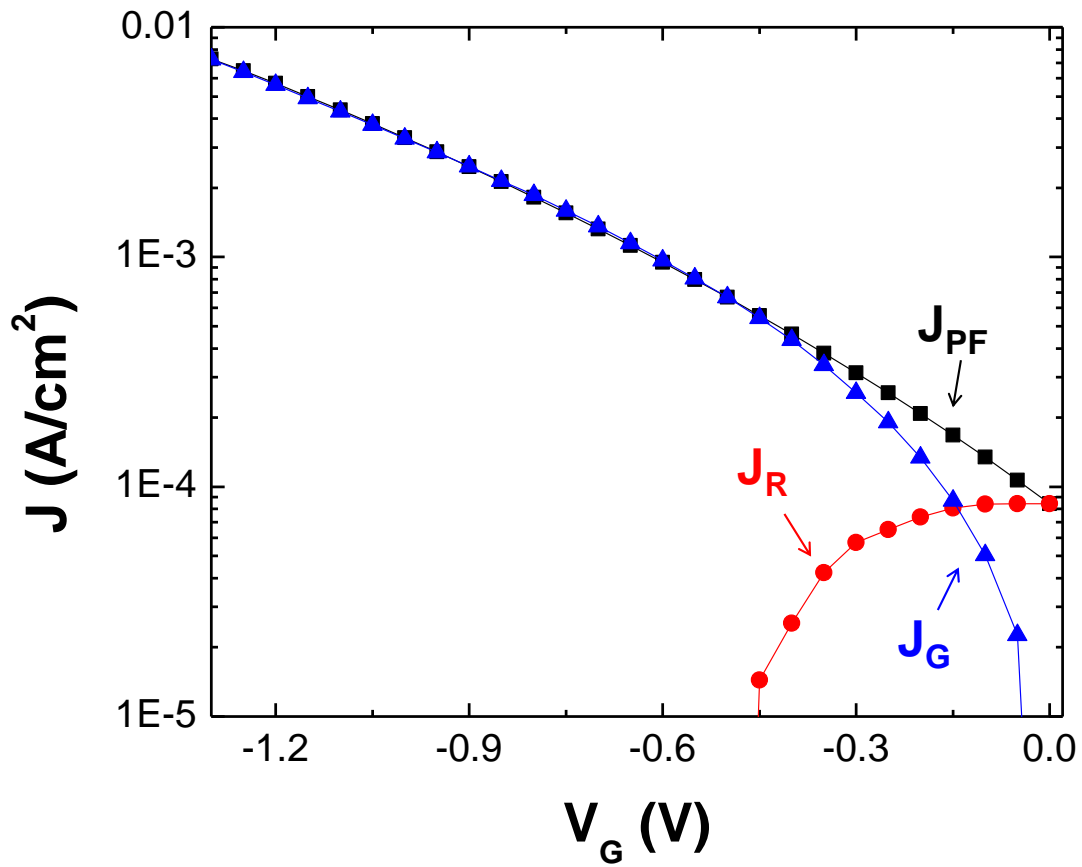


Figure 5-12. Measured J_G , ideal J_{PF} obtained by linear extrapolation of the linear PF fit, and J_R calculated by the difference between J_{PF} and J_G .

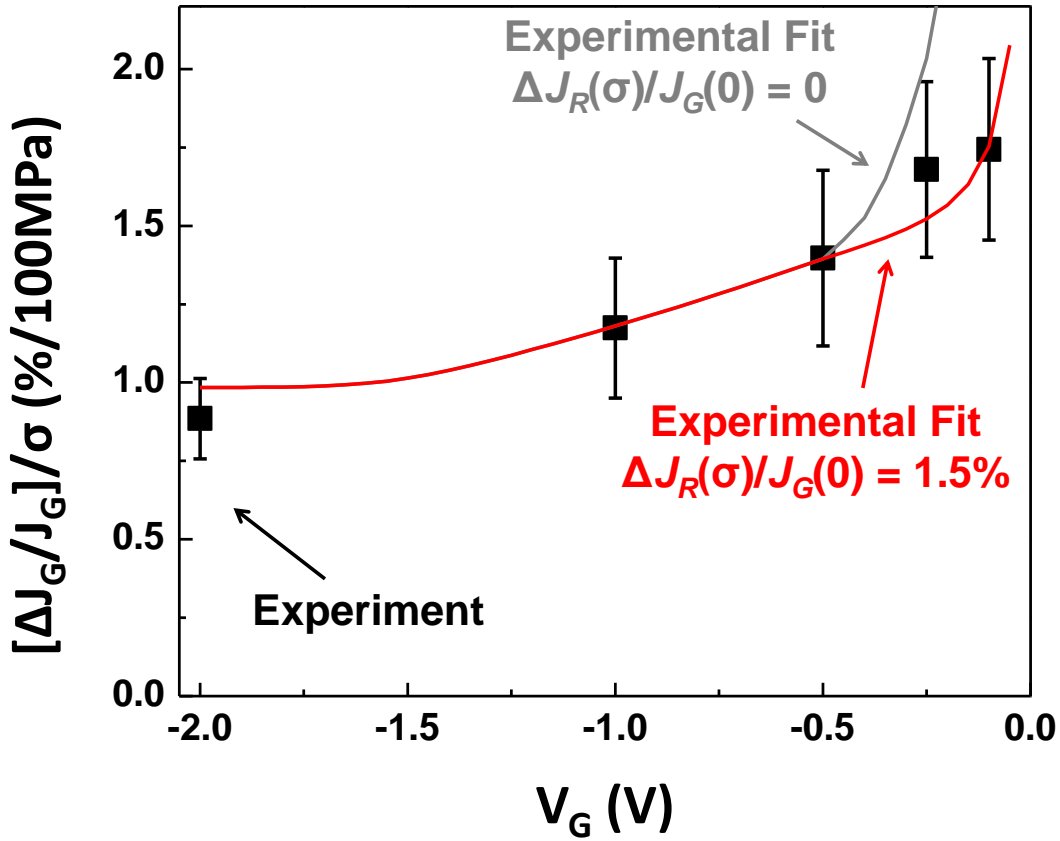


Figure 5-13. Simulated stress sensitivity of J_G at 100 MPa of stress, including J_R , as a function of reverse gate bias. J_R not changing with stress overestimates the stress sensitivity. However, $\Delta J_R(\sigma)/J_G(0) = 1.5\%$ closely matches experiment.

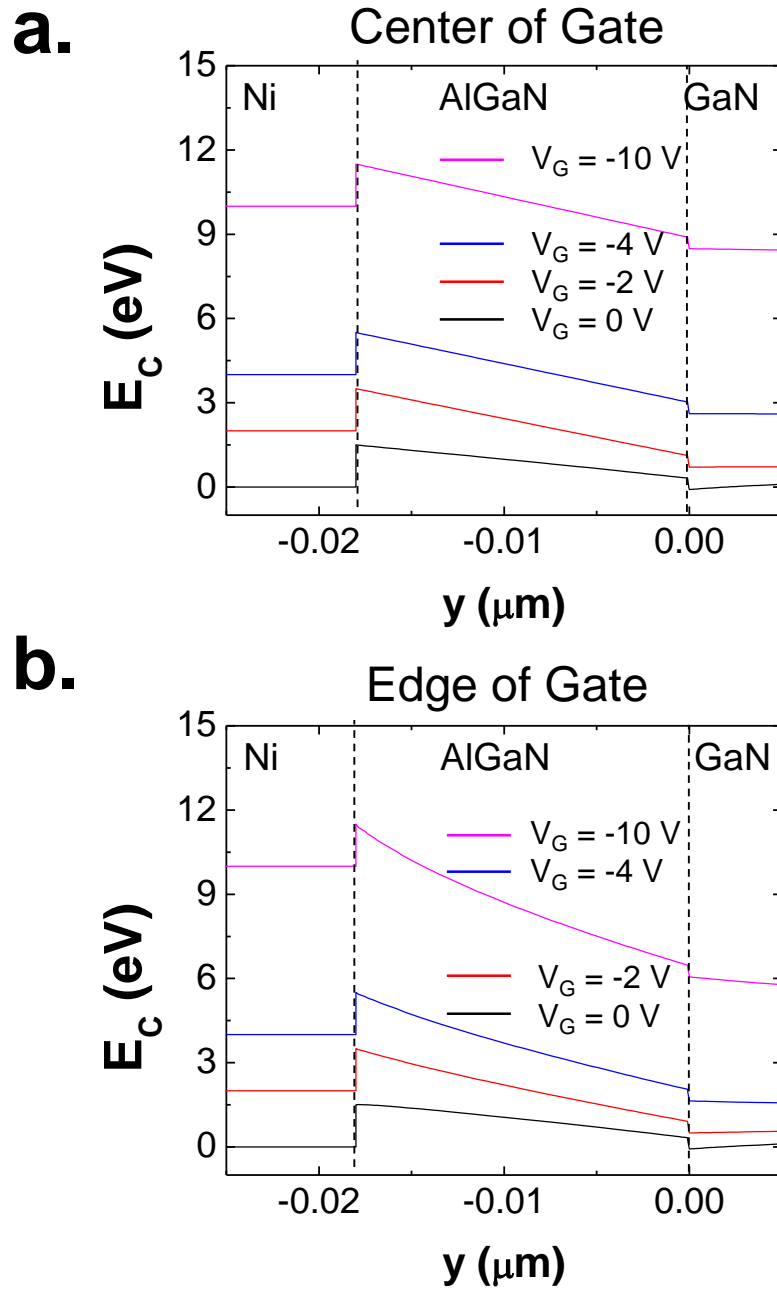


Figure 5-14. Energy band diagrams showing the reduction in the AlGaN barrier thickness at the gate edges for V_G well below V_T .

CHAPTER 6 CONCLUSION

Overall Summary

A systematic study of the effect of mechanical stress on AlGaIn/GaN HEMTs was presented in this dissertation. Stress is inherent to AlGaIn/GaN HEMTs, and can be beneficial or detrimental to performance and reliability. The lattice mismatch stress between AlGaIn and GaN benefits the device by creating the 2DEG inducing polarization, while stress generated via the inverse piezoelectric effect can induce degradation. To characterize the impact of stress on the performance and reliability of AlGaIn/GaN HEMTs, a novel technique was developed to apply external stress to small ($\sim 1 \text{ cm}^2$) wafer samples while simultaneously taking electrical measurements. A four-point wafer bending setup applied stress to the small sample, which was attached to a high carbon stainless steel strip with epoxy. To simultaneously conduct electrical measurements while varying the amount of mechanical stress, wires were attached to the bond pads with room temperature curing conductive epoxy.

An enormous variation in AlGaIn/GaN HEMT gauge factor measurements (4 to -40,000) have been reported in literature (E. Y. Chang, 2009; Eickhoff et al., 2001; Gaska et al., 1998; Kang et al., 2005, 2004; Yilmazoglu et al., 2006; Zimmermann et al., 2006) and is likely a result of charge trapping effects. After eliminating the charge trapping effects, the measured gauge factor of the AlGaIn/GaN HEMT was -2.8 ± 0.4 . This gauge factor indicates a small stress dependence on the device resistivity. This is explained by small changes in the 2DEG sheet carrier density and channel mobility. The experimental results were compared with a simulated gauge factor (-7.9 ± 5.2) to determine the best fitting set of elastic and piezoelectric coefficients of GaN and AlN.

In order to determine the dominant gate leakage mechanism, a thorough investigation of the relationship between E_{AlGaN} and V_G was presented. In a simple model of an ideal 1D device, E_{AlGaN} has a linear relationship to V_G above V_T , and saturates below V_T . Experimentally determined parameters were used in the 1D calculation to model the actual device. Adjusting σ_{int} and n_s based on experimental measurements provided an accurate V_G versus E_{AlGaN} relationship above threshold. Also, a comprehensive 2D simulation was performed to provide insight on E_{AlGaN} for large reverse biases much below V_T . The 2D results proved the 1D model accurate for $V_G > V_T$. However, below threshold, although E_{AlGaN} saturates in the middle of the gate, at the gate edges, E_{AlGaN} continues to increase.

PF conduction was proven to be the dominant gate leakage transport mechanism above threshold. Bias and stress dependence of J_G was measured simultaneously. A decreasing stress dependence of J_G with increasing reverse gate bias was observed. Tensile (compressive) stress increases (decreases) J_G for all applied gate biases ($V_G = -0.1$ to -4 V). Compressive stress increases E_A , and tensile stress decreases E_A . Since stress shifts the trap energy level, the compensation parameter r is also affected by stress. A reverse tunneling current was included in the model to balance the forward PF current at equilibrium. However, the reverse tunneling current only is important at extremely small gate biases. At very large increasing reverse biases, E_{AlGaN} at the gate edges continues to increase, which decreases the tunneling barrier making FN tunneling more probable. When degradation occurs, the contribution to J_G is dominated by FN tunneling at the edges of the gate.

Future Work

Mechanical stress has been shown to affect AlGaIn/GaN HEMT channel resistance and gate current. The demand for improved performance and reliability of AlGaIn/GaN HEMT devices requires further analysis into the role of mechanical stress in degradation.

A more comprehensive understanding of the reverse tunneling current will help to understand how stress affects the gate leakage current at very low reverse biases. More measurements of $\Delta J_G(\sigma)/J_G(0)$ data points need to be obtained at low bias ($-0.1 \text{ V} < V_G < 0 \text{ V}$) to see if reverse tunneling current is present, and if it has a stress dependence.

Also, degradation experiments combining the effects of temperature, electrical stress, light, and mechanical stress will provide further insight into the role of mechanical stress on device degradation. Since limitations on samples prevent a thorough statistical degradation investigation, experiments need to be designed to isolate the effect of stress on degradation. Gate current should be monitored to evaluate degradation as the device is incrementally stressed using temperature and electrical stress just prior to breakdown. Then, mechanical tensile stress can be applied to attempt to induce degradation. Then, a more direct relationship between stress and device failure can be obtained.

Also, trap characterization under mechanical stress to directly measure the change in trap energy with stress will be extremely beneficial. Using optical trap characterization methods will be best since there is no body contact in the AlGaIn/GaN HEMT devices making other characterization methods invalid. A more direct

measurement of the effect of stress on AlGaIn/GaN HEMT traps can help to engineer more reliable, better performing devices.

LIST OF REFERENCES

- [1] T. Mimura, S. Hiyamizu, T. Fujii, and K. Nanbu, "A New Field-Effect Transistor with Selectively Doped GaAs/n-AlxGa1-xAs Heterojunctions," *Japanese Journal of Applied Physics*, vol. 19, no. 5. p. L225-L227, May-1980.
- [2] T. Mimura, "The Early History of the High Electron Mobility Transistor (HEMT)," *IEEE Transactions on Microwave Theory and Techniques*, vol. 50, no. 3, pp. 780-782, Mar. 2002.
- [3] M. Asif Khan, A. Bhattarai, J. N. Kuznia, and D. T. Olson, "High Electron Mobility Transistor Based on a GaN-AlxGa1-xN Heterojunction," *Applied Physics Letters*, vol. 63, no. 9, p. 1214, 1993.
- [4] R. J. Trew, "High-Frequency Solid-State Electronic Devices," *IEEE Transactions on Electron Devices*, vol. 52, no. 5, pp. 638-649, May. 2005.
- [5] P. Rajagopal, T. Gehrke, and J. Roberts, "Large-Area, Device Quality GaN on Si Using a Novel Transition Layer Scheme," *Mater. Res. Soc. Symp. Proc.*, vol. 1, no. 1, pp. 6-11, 2003.
- [6] Cree inc., *CGH31240F 240 W, 2700-3100 MHz, 50-ohm Input/Output Matched, GaN HEMT for S-Band Radar Systems*. 2011.
- [7] Cree inc, *CMPA2735075F 75 W, 2.7 - 3.5 GHz, GaN MMIC, Power Amplifier*. 2011.
- [8] Y. Hao, S. Member, L. Yang, X. Ma, J. Ma, and A. A. Gan, "High-Performance Microwave Gate-Recessed," *Power*, vol. 32, no. 5, pp. 626-628, 2011.
- [9] O. Ambacher, J. Smart, J. R. Shealy, N. G. Weimann, K. Chu, M. Murphy, W. J. Schaff, L. F. Eastman, R. Dimitrov, L. Wittmer, M. Stutzmann, W. Rieger, and J. Hilsenbeck, "Two-Dimensional Electron Gases Induced by Spontaneous and Piezoelectric Polarization Charges in N-and Ga-face AlGaIn/GaN Heterostructures," *Journal of Applied Physics*, vol. 85, no. 6, p. 3222, 1999.
- [10] D. Gregusova, J. Bernat, M. Drzik, M. Marso, J. Novak, F. Uherek, and P. Kordos, "Influence of Passivation Induced Stress on the Performance of AlGaIn/GaN HEMTs," *Physica Status Solidi (C)*, vol. 2, no. 7, pp. 2619-2622, May. 2005.
- [11] J. Joh and J. A. del Alamo, "Critical Voltage for Electrical Degradation of GaN High-Electron Mobility Transistors," *IEEE Electron Device Letters*, vol. 29, no. 4, pp. 287-289, Apr. 2008.
- [12] S. Beeby, *MEMS Mechanical Sensors*. 2004.
- [13] J. Bardeen and W. Shockley, "Deformation Potentials and Mobilities in Non-Polar Crystals," *Physical Review*, vol. 80, no. 1, pp. 72-80, Oct. 1950.

- [14] C. S. Smith, "Piezoresistance Effect in Germanium and Silicon," *Physical Review*, vol. 94, no. 1, p. 42, 1954.
- [15] Y. Sun, S. Thompson, and T. Nishida, *Strain Effect in Semiconductors Theory and Device Applications*. 2010.
- [16] A. People, J. C. Bean, D. V. Lang, A. M. Sergent, H. L. Stormer, K. W. Wecht, R. T. Lynch, and K. Baldwin, "Modulation Doping in Ge_xSi_{1-x}/Si Strained Layer Heterostructure," *Applied Physics Letters*, vol. 45, no. 11, pp. 1231-1233, May. 1984.
- [17] H. M. Manasevit, "Electron Mobility Enhancement in Epitaxial Multilayer Si-Si_{1-x}Ge_x Alloy Films on (100) Si," *Applied Physics Letters*, vol. 41, no. 5, p. 464, 1982.
- [18] M. L. Lee and E. a Fitzgerald, "Hole Mobility Enhancements in Nanometer-Scale Strained-Silicon Heterostructures Grown on Ge-Rich Relaxed Si_{1-x}Ge_x," *Journal of Applied Physics*, vol. 94, no. 4, p. 2590, 2003.
- [19] K. Rim, S. Koester, M. Hargrove, J. Chu, P. M. Mooney, J. Ott, T. Kanarsky, P. Ronsheim, M. Jeong, A. Grill, and H.-S. P. Wong, "Strained Si NMOSFETs for High Performance CMOS Technology," *2001 Symposium on VLSI Technology. Digest of Technical Papers (IEEE Cat. No.01 CH37184)*, pp. 59-60, 2001.
- [20] S. Thompson, N. Anand, M. Armstrong, C. Auth, B. Arcot, M. Alavi, P. Bai, J. Bielefeld, R. Bigwood, J. Brandenburg, and others, "A 90 nm Logic Technology Featuring 50 nm Strained Silicon Channel Transistors, 7 Layers of Cu Interconnects, low k ILD, and 1 um² SRAM Cell," in *Electron Devices Meeting, 2002. IEDM'02. Digest. International*, 2002, pp. 61-64.
- [21] S. E. Thompson, M. Armstrong, C. Auth, M. Alavi, M. Buehler, R. Chau, S. Cea, T. Ghani, G. Glass, T. Hoffman, C.-H. Jan, C. Kenyon, J. Klaus, K. Kuhn, Z. Ma, B. McIntyre, K. Mistry, a Murthy, B. Obradovic, R. Nagisetty, P. Nguyen, S. Sivakumar, R. Shaheed, L. Shifren, B. Tufts, S. Tyagi, M. Bohr, and Y. El-Mansy, "A 90-nm Logic Technology Featuring Strained-Silicon," *IEEE Transactions on Electron Devices*, vol. 51, no. 11, pp. 1790-1797, Nov. 2004.
- [22] S. E. Thompson, M. Armstrong, C. Auth, S. Cea, R. Chau, G. Glass, T. Hoffman, J. Klaus, Z. Ma, B. McIntyre, a Murthy, B. Obradovic, L. Shifren, S. Sivakumar, S. Tyagi, T. Ghani, K. Mistry, M. Bohr, and Y. El-Mansy, "A Logic Nanotechnology Featuring Strained-Silicon," *IEEE Electron Device Letters*, vol. 25, no. 4, pp. 191-193, Apr. 2004.
- [23] H. Yang, R. Malik, S. Narasimha, Y. Li, R. Divakaruni, P. Agnello, S. Allen, A. Antreasyan, J. Arnold, K. Bandy, and others, "Dual stress liner for high performance sub-45nm gate length SOI CMOS manufacturing," in *Electron Devices Meeting, 2004. IEDM Technical Digest. IEEE International*, 2004, pp. 1075-1077.

- [24] a Sozza, a Curutchet, C. Dua, N. Malbert, N. Labat, and a Touboul, "AlGaIn/GaN HEMT Reliability Assessment by means of Low Frequency Noise Measurements," *Microelectronics and Reliability*, vol. 46, no. 9-11, pp. 1725-1730, Sep. 2006.
- [25] N. Sghaier, M. Trabelsi, N. Yacoubi, J. Bluet, A. Souifi, G. Guillot, C. Gaquiere, and J. Dejaeger, "Traps Centers and Deep Defects Contribution in Current Instabilities for AlGaIn/GaN HEMT's on Silicon and Sapphire Substrates," *Microelectronics Journal*, vol. 37, no. 4, pp. 363-370, Apr. 2006.
- [26] H. Rao and G. Bosman, "Device Reliability Study of High Gate Electric Field Effects in AlGaIn/GaN High Electron Mobility Transistors Using Low Frequency Noise Spectroscopy," *Journal of Applied Physics*, vol. 108, no. 5, p. 053707, 2010.
- [27] W. Kruppa, S. Binari, and K. Doverspike, "Low-frequency Dispersion Characteristics of GaN HFETs," *Electronics Letters*, vol. 31, no. 22, pp. 1951-1952, 1995.
- [28] M. a Khan, M. S. Shur, and Q. C. Chen, "Current/Voltage Characteristic Collapse in AlGaIn/GaN Heterostructure Insulated Gate Field Effect Transistors at High Drain Bias," *Electronics Letters*, vol. 30, no. 25, p. 2175, 1994.
- [29] J. Joh and J. D. Alamo, "A Simple Current Collapse Measurement Technique for GaN High-Electron Mobility Transistors," *Electron Device Letters, IEEE*, vol. 29, no. 7, pp. 665-667, 2008.
- [30] S. C. Binari, W. Kruppa, D. H. B., G. Kelnder, A. E. Wickenden, and J. A. Freitas, "Fabrication and Characterization of GaN FETs," *Solid-State Electronics*, vol. 41, no. 10, pp. 1549-1554, Apr. 1997.
- [31] S. Trassaert, B. Boudart, and C. Gaquiere, "Trap Effects Studies in GaN MESFETs by Pulsed Measurements," *Electronics*, vol. 35, no. 16, pp. 1386-1388, 1999.
- [32] S. C. Binari, K. Ikossi, J. a Roussos, W. Kruppa, H. B. Dietrich, D. D. Koleske, A. E. Wickenden, and R. L. Henry, "Trapping Effects and Microwave Power Performance in AlGaIn/GaN HEMTs," *IEEE Transactions on Electron Devices*, vol. 48, no. 3, pp. 465-471, Mar. 2001.
- [33] G. Meneghesso, A. Chini, E. Zanoni, M. Manfredi, M. Pavesi, B. Boudart, and C. Gaquiere, "Diagnosis of Trapping Phenomena in GaN MESFETs," *International Electron Devices Meeting 2000. Technical Digest. IEDM (Cat. No.00CH37138)*, pp. 389-392.
- [34] H. Kim, J. Lee, D. Liu, and W. Lu, "Gate Current Leakage and Breakdown Mechanism in Unpassivated AlGaIn/GaN High Electron Mobility Transistors by Post-Gate Annealing," *Applied Physics Letters*, vol. 86, no. 14, p. 143505, 2005.

- [35] J. Joh and J. a del Alamo, "Mechanisms for Electrical Degradation of GaN High-Electron Mobility Transistors," *2006 International Electron Devices Meeting*, pp. 1-4, Dec. 2006.
- [36] S. Y. Son, Y. S. Choi, P. Kumar, H. W. Park, T. Nishida, R. K. Singh, and S. E. Thompson, "Strain Induced Changes in Gate Leakage Current and Dielectric Constant of Nitrided Hf-Silicate Metal Oxide Semiconductor Capacitors," *Applied Physics Letters*, vol. 93, no. 15, p. 153505, 2008.
- [37] S. Dey, M. Agostinelli, C. Prasad, X. Wang, and L. Shifren, "Effects of Hot Carrier Stress on Reliability of Strained-Si MOSFETs," in *Reliability Physics Symposium Proceedings, 2006. 44th Annual., IEEE International*, 2006, pp. 461–464.
- [38] S. Adachi, *Handbook on Physical Properties of Semiconductors*, vol. 1. 2004.
- [39] M. Levinstein, S. Rumyantsev, and M. Shur, *Handbook Series on Semiconductor Parameters*. 1999.
- [40] A. F. M. Anwar, S. Member, S. Wu, and R. T. Webster, "Temperature Dependent Transport Properties in GaN , Al_xGa_{1-x}N , and In_x Ga_{1-x}N Semiconductors," *Transport*, vol. 48, no. 3, pp. 567-572, 2001.
- [41] R. Quay, "A Temperature Dependent Model for the Saturation Velocity in Semiconductor Materials," *Materials Science in Semiconductor Processing*, vol. 3, no. 1-2, pp. 149-155, Mar. 2000.
- [42] J. P. Ibbetson, P. T. Fini, K. D. Ness, S. P. DenBaars, J. S. Speck, and U. K. Mishra, "Polarization Effects, Surface States, and the Source of Electrons in AlGa_N/Ga_N Heterostructure Field Effect Transistors," *Applied Physics Letters*, vol. 77, no. 2, p. 250, 2000.
- [43] J. W. Johnson, J. Gao, K. Lucht, J. Williamson, C. Strautin, J. Riddle, R. Therrien, P. Rajagopal, J. C. Roberts, A. Vescan, J. D. Brown, A. Hanson, S. Singhal, R. Borges, E. L. Piner, and K. J. Linthicum, "Material, Process, and Device Development of GaN-based HFETs on Silicon Substrates," in *Proc. Electrochem. Soc.*, 2004, vol. 3, no. 111, p. 405.
- [44] S. Timoshenko, *Strength of Materials*. .
- [45] K. Wu, "Strain Effects on the Valence Band of Silicon: Piezoresistance in P-type Silicon and Mobility Enhancement in Strained Silicon PMOSFET," University of Florida, 2005.
- [46] "GaN Essentials - Substrates for GaN RF Devices," 2008. [Online]. Available: www.nitronex.com.

- [47] R. Gaska, J. W. Yang, a D. Bykhovski, M. S. Shur, V. V. Kaminski, and S. M. Soloviov, "The Influence of the Deformation on the Two-Dimensional Electron Gas Density in GaN–AlGa_N Heterostructures," *Applied Physics Letters*, vol. 72, no. 1, p. 64, 1998.
- [48] M. Eickhoff, O. Ambacher, G. Krötz, and M. Stutzmann, "Piezoresistivity of Al_xGa_{1-x}N Layers and Al_xGa_{1-x}N/GaN Heterostructures," *Journal of Applied Physics*, vol. 90, no. 7, p. 3383, 2001.
- [49] E. Y. Chang, "Changes of Electrical Characteristics for AlGa_N/Ga_N HEMTs Under Uniaxial Tensile Strain," *IEEE Electron Device Letters*, vol. 30, no. 3, pp. 213-215, Mar. 2009.
- [50] T. Zimmermann, M. Neuburger, P. Benkart, F. J. Hernandez-Guillen, C. Pietzka, M. Kunze, I. Daumiller, A. Dadgar, A. Krost, and E. Kohn, "Piezoelectric Ga_N Sensor Structures," *IEEE Electron Device Letters*, vol. 27, no. 5, pp. 309-312, May. 2006.
- [51] O. Yilmazoglu, K. Mutamba, and D. Pavlidis, "Strain Sensitivity of AlGa_N / Ga_N HEMT Structures for Sensing," *Engineer*, no. 7, pp. 1037-1041, 2006.
- [52] B. S. Kang, S. Kim, J. Kim, R. Mehandru, F. Ren, K. Baik, S. J. Pearton, B. P. Gila, C. R. Abernathy, C.-C. Pan, G.-T. Chen, J.-I. Chyi, V. Chandrasekaran, M. Sheplak, T. Nishida, and S. N. G. Chu, "AlGa_N/Ga_N High Electron Mobility Transistor Structures for Pressure and pH Sensing," *Physica Status Solidi (C)*, vol. 2, no. 7, pp. 2684-2687, May. 2005.
- [53] B. S. Kang, S. Kim, F. Ren, J. W. Johnson, R. J. Therrien, P. Rajagopal, J. C. Roberts, E. L. Piner, K. J. Linthicum, S. N. G. Chu, K. Baik, B. P. Gila, C. R. Abernathy, and S. J. Pearton, "Pressure-Induced Changes in the Conductivity of AlGa_N/Ga_N high-Electron Mobility-Transistor Membranes," *Applied Physics Letters*, vol. 85, no. 14, p. 2962, 2004.
- [54] R. Vetury, N. Q. Zhang, S. Keller, and U. K. Mishra, "The Impact of Surface States on the DC and RF Characteristics of AlGa_N / Ga_N HFETs," *Measurement*, vol. 48, no. 3, pp. 560-566, 2001.
- [55] S. C. Binari, K. Ikossi, J. a Roussos, W. Kruppa, H. B. Dietrich, D. D. Koleske, A. E. Wickenden, and R. L. Henry, "Trapping Effects and Microwave Power Performance in AlGa_N/Ga_N HEMTs," *IEEE Transactions on Electron Devices*, vol. 48, no. 3, pp. 465-471, Mar. 2001.
- [56] M. Gassoumi, J. Bluet, F. Chekir, I. Dermoul, H. Maaref, G. Guillot, A. Minko, V. Hoel, and C. Gaquiere, "Investigation of Traps in AlGa_N/Ga_N HEMTs by Current Transient Spectroscopy," *Materials Science and Engineering: C*, vol. 26, no. 2-3, pp. 383-386, Mar. 2006.

- [57] A. D. Koehler, A. Gupta, M. Chu, S. Parthasarathy, K. J. Linthicum, J. W. Johnson, T. Nishida, and S. E. Thompson, "Extraction of AlGa_N/Ga_N HEMT Gauge Factor in the Presence of Traps," *IEEE Electron Device Letters*, vol. 31, no. 7, pp. 665-667, 2010.
- [58] S. Bradley, A. Young, L. Brillson, M. Murphy, and W. Schaff, "Role of barrier and buffer layer defect states in AlGa_N/Ga_N HEMT structures," *Journal of Electronic Materials*, vol. 30, no. 3, pp. 123–128, 2001.
- [59] H. Kim, A. Vertiatchikh, R. Thompson, V. Tilak, T. Prunty, J. Shealy, and L. Eastman, "Hot Electron Induced Degradation of Undoped AlGa_N/Ga_N HFETs," *Microelectronics Reliability*, vol. 43, no. 6, pp. 823-827, Jun. 2003.
- [60] M. Chu, T. Nishida, X. Lv, N. Mohta, and S. E. Thompson, "Comparison Between High-Field Piezoresistance Coefficients of Si Metal-Oxide-Semiconductor Field-Effect Transistors and Bulk Si Under Uniaxial and Biaxial Stress," *Journal of Applied Physics*, vol. 103, no. 11, p. 113704, 2008.
- [61] O. Ambacher, "Two-Dimensional Electron Gases Induced by Spontaneous and Piezoelectric Polarization Charges in N- and Ga-face AlGa_N/Ga_N Heterostructures," *Journal of Applied Physics*, vol. 83, no. 6, p. 3656, 1999.
- [62] A. Zoroddu, F. Bernardini, P. Ruggerone, and V. Fiorentini, "First-Principles Prediction of Structure, Energetics, Formation Enthalpy, Elastic Constants, Polarization, and Piezoelectric Constants of AlN, GaN, and InN: Comparison of Local and Gradient-Corrected Density-Functional Theory," *Physical Review B*, vol. 64, no. 4, pp. 1-6, Jul. 2001.
- [63] I. L. Guy, S. Muensit, E. M. Goldys, and D. Interna-, "Extensional Piezoelectric Coefficients of Gallium Nitride and Aluminum Nitride," *Applied Physics Letters*, vol. 75, no. 26, pp. 4133-4135, 1999.
- [64] K. Shimada, T. Sota, and K. Suzuki, "First-Principles Study on Electronic and Elastic Properties," *Journal of Applied Physics*, vol. 84, no. 9, 1998.
- [65] D. Vanderbilt, "Spontaneous Polarization and Piezoelectric Constants of III-V Nitrides," *Physical Review B*, vol. 56, no. 16, pp. 24-27, 1997.
- [66] A. Wright, "Elastic Properties of Zinc-Blende and Wurtzite AlN, GaN, and InN," *Journal of applied physics*, vol. 82, no. September, p. 2833, 1997.
- [67] A. Polian, M. Grimsditch, and I. Grzegory, "Elastic Constants of Gallium Nitride," vol. 79, no. March, pp. 3343-3344, 1996.
- [68] K. Kim, W. Lambrecht, and B. Segall, "Elastic constants and related properties of tetrahedrally bonded BN, AlN, GaN, and InN.," *Physical review. B, Condensed matter*, vol. 53, no. 24, pp. 16310-16326, Jun. 1996.

- [69] K. Kim, W. R. L. Lambrecht, and B. Segall, "Electron Structure of GaN with Strain and Phonon Distortions," *Physical review. B, Condensed matter*, vol. 50, Feb. 1994.
- [70] E. Ruiz, S. Alvarez, and P. Alemany, "Electronic Structure and Properties of AlN.," *Physical review. B, Condensed matter*, vol. 49, no. 11, pp. 7115-7123, Mar. 1994.
- [71] T. Yang and S. Nakajima, "Electronic structures of Wurtzite GaN, InN and their alloy $\text{Ga}_{1-x}\text{In}_x\text{N}$ calculated by the tight-binding method," *Japanese journal of applied physics*, 1995.
- [72] M. Chu, A. D. Koehler, A. Gupta, T. Nishida, and S. E. Thompson, "Simulation of AlGaIn/GaN High-Electron-Mobility Transistor Gauge Factor Based on Two-Dimensional Electron Gas Density and Electron Mobility," *Journal of Applied Physics*, vol. 108, no. 10, p. 104502, 2010.
- [73] M. Yamaguchi, T. Yagi, T. Sota, T. Deguchi, K. Shimada, and S. Nakamura, "Brillouin scattering study of bulk GaN," *Journal of Applied Physics*, vol. 85, no. 12, p. 8502, 1999.
- [74] C. Deger, E. Born, H. Angerer, O. Ambacher, M. Stutzmann, J. Hornsteiner, E. Riha, and G. Fischerauer, "Sound Velocity of $\text{Al}_x\text{Ga}_{1-x}\text{N}$ Thin Films Obtained by Surface Acoustic-Wave Measurements," *Applied Physics Letters*, vol. 72, no. 19, p. 2400, 1998.
- [75] A. D. Bykhovski, V. V. Kaminski, M. S. Shur, Q. C. Chen, and M. A. Khan, "Piezoresistive Effect in Wurtzite n-type GaN," *Applied Physics Letters*, vol. 68, no. 6, p. 818, 1996.
- [76] K. Tsubouchi, "Zero Temperature Coefficient SAW Delay Line on AlN Epitaxial Films," *1983 Ultrasonics Symposium*, vol. 32, no. 5, p. 634, 1983.
- [77] S. Mizuno, Y. Ohno, S. Kishimoto, K. Maezawa, and T. Mizutani, "Large Gate Leakage Current in AlGaIn/GaN High Electron Mobility Transistors," *Japanese Journal of Applied Physics*, vol. 41, no. Part 1, No. 8, pp. 5125-5126, Aug. 2002.
- [78] S. Huang, B. Shen, F.-J. Xu, F. Lin, Z.-L. Miao, J. Song, L. Lu, L.-B. Cen, L.-W. Sang, Z.-X. Qin, Z.-J. Yang, and G.-Y. Zhang, "Study of the Leakage Current Mechanism in Schottky Contacts to Al_{0.25}Ga_{0.75}N/GaN Heterostructures with AlN Interlayers," *Semiconductor Science and Technology*, vol. 24, no. 5, p. 055005, May. 2009.
- [79] S. Karmalkar, D. M. Sathaiya, and M. S. Shur, "Mechanism of the Reverse Gate Leakage in AlGaIn/GaN High Electron Mobility Transistors," *Applied Physics Letters*, vol. 82, no. 22, p. 3976, 2003.

- [80] E. J. Miller, E. T. Yu, P. Waltereit, and J. S. Speck, "Analysis of Reverse-Bias Leakage Current Mechanisms in GaN Grown by Molecular-Beam Epitaxy," *Applied Physics Letters*, vol. 84, no. 4, p. 535, 2004.
- [81] L. Fang, W. Tao, S. Bo, H. Sen, and M. Nan, "The Leakage Current Mechanisms in the Schottky Diode with a Thin Al Layer Insertion Between Al_{0.245}Ga_{0.755}N/GaN Heterostructure and Ni/Au Schottky Contact," *Chinese Physics B*, vol. 1614, 2009.
- [82] D. M. Sathaiya and S. Karmalkar, "Edge Effects on Gate Tunneling Current in HEMTs," *IEEE Transactions on Electron Devices*, vol. 54, no. 10, pp. 2614-2622, Oct. 2007.
- [83] S. Arulkumaran, T. Egawa, H. Ishikawa, and T. Jimbo, "Temperature Dependence of Gate-Leakage Current in AlGa_N/Ga_N High-Electron-Mobility Transistors," *Applied Physics Letters*, vol. 82, no. 18, p. 3110, 2003.
- [84] J. C. Carrano, T. Li, P. A. Grudowski, C. J. Eiting, R. D. Dupuis, and J. C. Campbell, "Current Transport Mechanisms in GaN-Based Metal-Semiconductor-Metal Photodetectors," *Applied Physics Letters*, vol. 72, no. 5, pp. 542-544, 1998.
- [85] D. Mahaveer Sathaiya and S. Karmalkar, "Thermionic Trap-Assisted Tunneling Model and its Application to Leakage Current in Nitrided Oxides and AlGa_N/Ga_N High Electron Mobility Transistors," *Journal of Applied Physics*, vol. 99, no. 9, p. 093701, 2006.
- [86] D. M. Sathaiya and S. Karmalkar, "A Closed-Form Model for Thermionic Trap-Assisted Tunneling," *IEEE Transactions on Electron Devices*, vol. 55, no. 2, pp. 557-564, Feb. 2008.
- [87] S. Sudharsanan and S. Karmalkar, "Modeling of the Reverse Gate Leakage in AlGa_N/Ga_N High Electron Mobility Transistors," *Journal of Applied Physics*, vol. 107, no. 6, p. 064501, 2010.
- [88] T. Hashizume, J. Kotani, and H. Hasegawa, "Leakage Mechanism in GaN and AlGa_N Schottky Interfaces," *Applied Physics Letters*, vol. 84, no. 24, p. 4884, 2004.
- [89] W. Chikhaoui, J. M. Bluet, P. Girard, G. Bremond, C. Bru-Chevallier, C. Dua, and R. Aubry, "Deep Levels Investigation of AlGa_N/Ga_N Heterostructure Transistors," *Physica B: Condensed Matter*, vol. 404, no. 23-24, pp. 4877-4879, Dec. 2009.
- [90] K. H. Lee, S. J. Chang, P. C. Chang, Y. C. Wang, and C. H. Kuo, "High Quality GaN-Based Schottky Barrier Diodes," *Applied Physics Letters*, vol. 93, no. 13, p. 132110, 2008.
- [91] O. Mitrofanov, "Poole-Frenkel Electron Emission from the Traps in AlGa_N/Ga_N Transistors," *Journal of Applied Physics*, vol. 95, no. 11, p. 6414, 2004.

- [92] J. Spradlin, S. Doğan, J. Xie, R. Molnar, a a Baski, and H. Morkoç, "Investigation of Forward and Reverse Current Conduction in GaN films by Conductive Atomic Force Microscopy," *Applied Physics Letters*, vol. 84, no. 21, p. 4150, 2004.
- [93] H. Zhang, E. J. Miller, and E. T. Yu, "Analysis of Leakage Current Mechanisms in Schottky Contacts to GaN and Al_{0.25}Ga_{0.75}N/GaN Grown by Molecular-Beam Epitaxy," *Journal of Applied Physics*, vol. 99, no. 2, p. 023703, 2006.
- [94] D. Yan, H. Lu, D. Cao, D. Chen, R. Zhang, and Y. Zheng, "On the Reverse Gate Leakage Current of AlGaIn/GaN High Electron Mobility Transistors," *Applied Physics Letters*, vol. 97, no. 15, p. 153503, 2010.
- [95] E. J. Miller, X. Z. Dang, E. T. Yu, and I. Introduction, "Gate leakage current mechanisms in AlGaIn/GaN heterostructure field-effect transistors," *Journal of Applied Physics*, vol. 88, no. 10, 2000.
- [96] D. Yan, H. Lu, D. Cao, D. Chen, R. Zhang, and Y. Zheng, "On the reverse gate leakage current of AlGaIn/GaN high electron mobility transistors," *Applied Physics Letters*, vol. 97, no. 15, p. 153503, 2010.
- [97] J. W. Chung, J. C. Roberts, E. L. Piner, and T. Palacios, "Effect of gate leakage in the subthreshold characteristics of AlGaIn/GaN HEMTs," *Electron Device Letters, IEEE*, vol. 29, no. 11, pp. 1196–1198, 2008.
- [98] J. Chung, X. Zhao, and T. Palacios, "Estimation of Trap Density in AlGaIn/GaN HEMTs from Subthreshold Slope Study," *Device Research Conference*, no. 617, pp. 5-6, 2007.
- [99] L. Kolaklieva and R. Kakanakov, "Ohmic Contacts for High Power and High Temperature Microelectronics," *Micro Electronic and Mechanical Systems*, no. December, 2009.
- [100] A. Chini, V. Di Lecce, M. Esposito, G. Meneghesso, and E. Zanoni, "RF degradation of GaN HEMTs and its correlation with DC stress and I-DLTS measurements," in *Microwave Integrated Circuits Conference, 2009. EuMIC 2009. European*, 2009, no. September, pp. 132–135.
- [101] J. Joh, L. Xia, and J. a del Alamo, "Gate Current Degradation Mechanisms of GaN High Electron Mobility Transistors," *2007 IEEE International Electron Devices Meeting*, pp. 385-388, 2007.
- [102] M. Chu, "Characterization and Modeling of Strain in Si FET and GaN HEMT Devices (Unpublished)," University of Florida, 2011.
- [103] J. Yeagan and H. Taylor, "The Poole Frenkel Effect with Compensation Present," *Journal of Applied Physics*, vol. 39, no. 12, pp. 5600–5604, 1968.

- [104] W. R. Harrell and C. Gopalakrishnan, "Implications of Advanced Modeling on the Observation of Poole–Frenkel Effect Saturation," *Thin Solid Films*, vol. 405, pp. 205-217, 2002.
- [105] W. R. Harrell and J. Frey, "Observation of Poole- Frenkel Effect Saturation in SiO₂ and Other Insulating Films," *Thin Solid Films*, vol. 352, pp. 195-204, 1999.
- [106] Y. S. Choi, H. Park, T. Nishida, and S. E. Thompson, "Reliability of HfSiON Gate Dielectric Silicon MOS Devices Under [110] Mechanical Stress: Time Dependent Dielectric Breakdown," *Journal of Applied Physics*, vol. 105, no. 4, p. 044503, 2009.
- [107] Y. S. Choi, T. Nishida, and S. E. Thompson, "Impact of Mechanical Stress on Direct and Trap-Assisted Gate Leakage Currents in P-Type Silicon Metal-Oxide-Semiconductor Capacitors," *Applied Physics Letters*, vol. 92, no. 17, p. 173507, 2008.
- [108] M. E. Levinshtein, S. L. Rumyantsev, and M. Shur, *Properties of Advanced Semiconductor Materials : GaN, AlN, InN, BN, SiC, SiGe*. Wiley, 2001, pp. 1-30.

BIOGRAPHICAL SKETCH

Andrew (Andy) Daniel Koehler was born in 1982 in Gainesville, Florida. He received his B. S. and M. S. degrees in electrical and computer engineering from the University of Florida in 2004 and 2007 respectively. He has been pursuing his Ph.D. degree in electrical and computer engineering under Dr. Scott E. Thompson and co-supervised by Dr. Toshikazu Nishida since 2005 focusing on the impact of strain on novel device materials and structures.

During his graduate studies, he also completed three internships with Intel Corporation. In 2006 he interned in Rio Rancho, New Mexico with Fab 11 Sort, optimizing testing of NOR flash devices for functional defects. In the summers of 2007 and 2008 he interned in Hillsboro, Oregon with Components Research exploring methods of fabricating semiconducting nanowire FETs and investigating the stress dependence of III-V devices. He received his Ph.D. from the University of Florida in the fall of 2011.